Universita degli Studi di Ferrara

DOTTORATO DI RICERCA IN
FISICA

CICLO XXX

COORDINATORE Prof. Guidi Vincenzo

NEW SCHEMES AND EXPERIMENTS FOR HIGH EFFICIENCY BEAM STEERING THROUGH COHERENT EFFECTS IN BENT CRYSTALS

Settore Scientifico Disciplinare FIS/01

Dottorando
Dott. Sytov Alexei

Tutore
Prof. Guidi Vincenzo

Tutore esterno
Prof. Tikhomirov Victor

Anni 2014-2017

CONTENTS

INTRODUCTION

The basic principle of coherent effects of charged particle interaction with a crystal is an ordered atomic structure of the crystal substance, so-called crystal lattice. In particular, if a charge particle hits a bent crystal at a very small angle w.r.t. a crystal axis or plane, its penetration depth will considerably increase. This is the basic idea of the channeling effect. Channeling is the effect of the penetration of charged particles through a single crystal parallel to its crystalline axes or planes, moving in the averaged field of the latter.

Stark was the first [1], who pointed out the possibility of the existence of this effect in 1912. However, the first experimental confirmation of this effect was obtained only in 1960 in the works of Davis et al. [2] who showed that, in contrast to the case of amorphous solids, the distribution of the number of ions over penetration depth in crystalline substances has a long tail at great depths. To test these experiments, Robinson and Oen [3] in 1963 performed numerical simulation of the penetration of ions into the crystal. They showed that a small fraction of the ions incident on the crystal at a small angle to the atomic plane or chain are localized inside the channel. Thus, theoretically, the channeling phenomenon was first confirmed by simulations. Two years later, Lindhard [4] developed a theory of channeling, in which he defined the critical angle of capture under the channeling conditions.

The field of channeling was considerably extended in 1976, after Tsyganov suggested using channeling in *bent* crystals to deflect charged particle beams [5]. This idea opened up huge opportunities for the use of crystals, in particular at accelerators, where a bent crystal in many cases can replace bulky and expensive electric deflectors and deflecting magnets. In addition, another important effect of particle deflection, so-called volume reflection, was suggested in [6, 7], being reflection of charged particles from curved crystalline planes.

Curved crystals possess wide opportunities for accelerator physics. Very strong electric field, applied with accuracy to Angstrom, allow to deflect particles with high efficiency. The main advantage of bent crystals is their compact dimensions, low cost and easy installation and operation. Bent crystals allow one to control beams of different energies (from several MeV up to tens of TeV) of different types of charged particles (protons, muons, electrons, positrons, etc.).

Since then, experiments on deflection of beams with curved crystals have been carried out in many of the world's largest scientific centers: CERN (Geneva, Switzerland), Fermi National Accelerator Laboratory (Fermilab) (Batavia, USA), Brookhaven National Laboratory (Brookhaven, USA), IHEP

(Protvino, Russia), PNPI (Gatchina, Russia), JINR (Dubna, Russia), INFN (Italy), the Institute of Nuclear Physics (Mainzer Mikrotron MAMI, Germany) and others [8–32, 34–37] and [A6, A7]. Moreover, bent crystals were applied for beam collimation [38–49] and extraction [38, 41, 42, 50] from an accelerator (IHEP, U-70 synchrotron; Fermilab, Tevatron; CERN, SPS and LHC). Apart from these bent crystals represent a very promising instrument for generation of X-ray and γ radiation, as shown by a number of experiments [32, 34–37, 51–56].

The work presented in this thesis is dedicated to the study of coherent effects of beam steering by a bent crystal at ultrarelativistic energies.

The first chapter is devoted to the overview of the coherent effects, connected with planar and axial channeling. In particular the motion in the average interplanar and interaxial potential is considered along with effects of multiple and single scattering on nuclei and electrons. In addition the effects of dechanneling, volume capture and volume reflection are discussed. Moreover some advanced effects, such as multiple volume reflection in one bent crystal are described.

In the second chapter the model of particle dynamics in a bent crystal accompanied by processes of multiple and single Coulomb scattering as well as nuclear scattering and the model implementation into the CRYSTAL simulation code are introduced. Additionally the High Performance Computing (HPC) features are described, namely Message Passing Interface (MPI) parallelization, as well as the routine for variation of initial parameters for the solution optimization problem.

The third chapter is dedicated to the application of the methods of beam steering by means of bent crystals to the future accelerator projects on the example of the Future Circular Collider. In this chapter the multiple volume reflection in one bent crystal and a crystal sequence are considered. Moreover the technique of channeling efficiency increase by means of the narrow plane cut as well as channeling angular acceptance increase by means of the channeling in skew planes are studied. The theoretical model to optimize the mentioned effects is introduced. Finally, a way to apply these effects for beam steering at the Future Circular Collider is proposed.

The forth chapter represents the results of the experiment at Mainz Mikrotron MAMI, dedicated to sub-GeV electron steering in ultra-thin silicon and germanium bent crystals. In particular, the measuring of dechanneling length and channeling efficiency as well as volume reflection angle in dependence on the crystal bending radius is described. The results for different values bending radius were obtained by the same crystal, bent by means of innovative pieso-electric driven holder. The fitting model to extract channeling efficiency and dechanneling length is introduced and applied to both experimental and simulation results. The influence of over-barrier particles to the dechanneling length is also studied.

The fifth chapter is devoted to the process of channeling and over-barrier (quasichanneling) oscillations and, in particular, to the way of their direct experimental observation, predicted in this work. For their observation it is suggested to use the trajectories correlations, being transformed into series of peaks in the deflection angle distribution. The mechanism of such transformation as well as the observation conditions are introduced. This description is supported by both analytical quantatitive model and Monte Carlo simulations. The representation of these correlations in ionization loss process is also described. Finally the first experimental observation of the quasichanneling oscillations in the deflection angle distribution is presented.

LIST OF PUBLICATIONS

The work presented in this thesis is based on the following articles:

A1 A. I. Sytov, Vestnik. Belarusian. Univ. Series **1** N2 (2014), 48–52, (in Russian), *Application of bent crystal for proton beam extraction from a storage ring*

A2 V. V. Tikhomirov, A. I. Sytov, Nucl. Instr. and Meth. in Phys. Res. B **309**, 109–114 (2013), *Multiple volume reflection in one crystal as an origin of significant scattering intensity and radiation power increase*

A3 A. I. Sytov, V. V. Tikhomirov, Nucl. Instr. and Meth. in Phys. Res. B **355**, 383–386 (2015), *CRYSTAL simulation code and modeling of coherent effects in a bent crystal at the LHC*

A4 A. I. Sytov *et al*, Eur. Phys. J. C. **76**, 77 (2016), *Planar channeling and quasichanneling oscillations in a bent crystal*

A5 A. I. Sytov, V. V. Tikhomirov, and A. S. Lobko, Phys. Rev. Acc. and Beams **20**, 071001 (2017), *Crystal collimator systems for high energy frontier*

A6 T. N. Wistisen *et al*, Phys. Rev. Lett. **119**, 024801 (2017), *Observation of Quasichanneling Oscillations*

A7 A. I. Sytov *et al*, Eur. Phys. J. C. **77**, 901 (2017), *Steering of Sub-GeV electrons by ultrashort Si and Ge bent crystals*

Articles and proceeding not included in this thesis, published before and during the PhD:

N1 V. V. Tikhomirov, A. I. Sytov, Proc. of the 23th Intern. Conf. "Russian Particle Accelerator Conference" RuPAC 2012. September 24-28, 2012, Peterhof, St. Petersburg, Russia. 79–81 (2012), *New ideas for crystal collimation*

N2 V. V. Tikhomirov, A. I. Sytov, A. Golovanov. Proc. of the 4th Congress of Belarusian Physicists. April 24-26, 2013, Minsk, Belarus, 15–16 (2013), *New possibilities of beam controlling of charged particles with bent crystals*

N3 V. V. Tikhomirov, A. I. Sytov. Problems of Atomic Science and Technology **57** N1, 88-92 (2012), *The miscut angle influence on the future LHC crystal based collimation system*

N4 E. Bagli *et al*, Phys. Rev. Lett. **115**, 015503 (2015), *Orientational coherent effects of high-energy particles in a LiNbO3 crystal*

N5 L. Bandiera *et al*, Eur. Phys. J. C. **76**, 80 (2016), *Relaxation of axially confined 400 GeV/c protons to planar channeling in a bent crystal*

N6 E. Bagli et al, Eur. Phys. J. C. **77**, 71 (2017), *Experimental evidence of independence of nuclear de-channeling length on the particle charge sign*

N7 V. G. Baryshevsky et al, Nucl. Instr. and Meth. in Phys. Res. B **402**, 35–39 (2017), *On the influence of crystal structure on the electromagnetic shower development in the lead tungstate crystals*

N8 U. Wienands et al, Nucl. Instr. and Meth. in Phys. Res. B **402**, 11–15 (2017), *Channeling and radiation experiments at SLAC*

N9 L. Bandiera et al, Nucl. Instr. and Meth. in Phys. Res. B **402**, 296–299 (2017), *Splitting of a high-energy positively-charged particle beam with a bent crystal*

CHAPTER 1
COHERENT EFFECTS OF CHARGED PARTICLES INTERACTION WITH A CRYSTAL

1.1 Introduction to the channeling effect

Channeling [4, 57–65] is the effect of the penetration of charged particles through a monocrystal parallel to its atomic axes or planes (Fig. 1.1). The principle idea of the effect the following. If charged particles move along crystal axes or planes, they experience interaction with atomic planes or strings as a hole, representing in fact coherent interaction with a crystal lattice, while the incorrelated events of Coulomb scattering are suppressed. In other words, charged particles flow in the field of atomic planes or axes with considerably lower "resistance" than in amorphous media.

Fig. 1.1 qualitatively illustrates also the condition of the channeling effect. It is possible only if the incident angle of the charged particle is lower than its limiting value, so called critical channeling angle or Lindhard angle [4]. In addition, one can notice the oscillatory character of motion of the channeling particles, being consequently reflected by crystal planes or axes. This pecularity leads to a wide number of coherent effects of deflections and reflections. One can influence on this motion by changing the crystal orientation and, therefore, by choosing different atomic planes or strings to exploit the coherent effects. Moreover, since the atomic fields in the crystal lattice may exceed hundreds of GeV/cm, being unachievable by existing technologies by using electric or magnetic deflectors, coherent effects in crystals provide unique possibilities for beam steering. Moreover, charged particles deflection in a such strong electric field is accompanied by X-ray and γ radiation [59, 63, 66–69], providing another promising application of bent crystals.

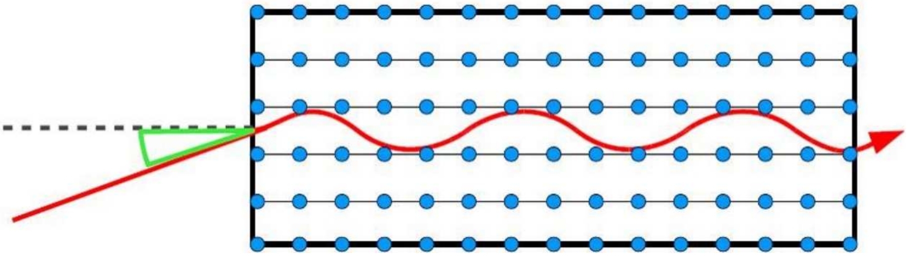

Figure 1.1: Illustration of channeling effect.

1.1.1 An averaged atomic potential

The first theoretical model of the channeling effect was proposed by Jens Lindhard [4]. His main idea was to apply the approximation of the averaged atomic potential. In other words, if a charged particle enters the crystal at rather low angle w.r.t. a crystal plane or axis, one can replace the sum atomic potentials by an averaged atomic potential, representing the coherent interaction with atomic axis or plane as a hole. Later the theory of channeling was summarized in a lot of reviews and monographs [57–65].

The potential of an atomic plane can be calculated by using the potential of a single atom $V_(x, y, z)$ in the following way (in the case of monoatomic crystal):

$$V_{pl}(x) = N d_{pl} \int_{-\infty}^{\infty} \int_{-\infty}^{\infty} V(x, y, z) dydz, \tag{1.1}$$

where the integration is carried out on the longitudinal coordinate z and the transverse coordinate y, while x is another transverse coordinate, orthogonal to the plane, d_{pl} is the average interplanar distance, N is the atomic concentration. The interplanar potential can be calculated as a sum (1.1) for different planes. Since in a crystal lattice possesses periodic structure, the interplanar potential can be written in the following way[1]:

$$U_{pl}(x) = \sum_{i=-\infty}^{\infty} \sum_{j=1}^{N_{pl}} V_{pl}(x + i d_{pl\ j}), \tag{1.2}$$

where the first sum bears on the plane number, while the second one on the number of different interplanar distances $d_{pl\ j}$, the total number of which is N_{pl}, $d_{pl} = \sum_{j=1}^{N_{pl}} d_{pl\ j}/N_{pl}$ (for equidistant planes $N_{pl} = 1$, $d_{pl} = d_{pl\ 1}$). Usually, the infinite sum can be cut off to the sum of several nearby atomic planes. If one would like to calculate the potential at the crystal boundary, he must replace in 1.2 one infinity sign by 0.

The potential of an atomic string can be calculated by using the potential of a single atom $V(x, y, z)$ in the following way:

$$V_{ax}(x, y) = \frac{1}{d_{at}} \int_{-\infty}^{\infty} V(x, y, z) dz, \tag{1.3}$$

where the integration is carried out on the longitudinal coordinate z, d_{at} is the averaged interatomic distance in a string.

---

[1] Sometimes the interplanar potential will be marked as $U(x)$, where only the planar case is considered.

The interaxial potential can be found as a sum of the atomic strings (usually several nearby atomic strings are already enough for high accuracy):

$$U_{ax}(x,y) = \sum_{i=-\infty}^{\infty} \sum_{j=-\infty}^{\infty} V_{ax}(x - x_{ax\ i}, y - y_{ax\ i}), \tag{1.4}$$

$x_{ax\ i}$ and $y_{ax\ i}$ are coordinates of atomic strings.

In a real crystal one must take into account also thermal vibrations of atoms. The distribution of thermal oscillations in 3 dimensions represents gaussian distribution:

$$w(x,y,z) = \frac{1}{(2\pi u_1^2)^{3/2}} \exp\left(-\frac{x^2+y^2+z^2}{2u_1^2}\right), \tag{1.5}$$

where u_1 is the amplitude of thermal vibrations, being equal for silicon to 0.075 Å.

The potential of a crystal plane or axis, can be averaged by thermal vibrations by using 1D and 2D distribution respectively:

$$w_{pl}(x) = \frac{1}{\sqrt{2\pi u_1^2}} \exp\left(-\frac{x^2}{2u_1^2}\right), \tag{1.6}$$

$$w_{ax}(x) = \frac{1}{2\pi u_1^2} \exp\left(-\frac{x^2+y^2}{2u_1^2}\right), \tag{1.7}$$

which can be found as:

$$V_{pl0}(x) = \int_{-\infty}^{\infty} V_{pl}(x-\chi) w_{pl}(\chi) d\chi, \tag{1.8}$$

$$V_{ax0}(x,y) = \int_{-\infty}^{\infty}\int_{-\infty}^{\infty} V_{ax}(x-\chi, y-\upsilon) w_{pl}(\chi,\upsilon) d\chi d\upsilon, \tag{1.9}$$

and can be used instead of $V_{pl}(x)$ and $V_{ax}(x,y)$ in (1.2,1.4).

The simplest approximation of the interplanar potential is the harmonic approximation:

$$U_{pl}(x) = \frac{4U_0 x^2}{d_{pl}^2}, \tag{1.10}$$

where U_0 is the potential depth. Though such approximation is very rude, it allows to find analytically the solution of the equation of motion (see below).

The atomic potential may be usually described as a Coulomb potential, screened by the cloud of electrons. It can be written in the Tomas-Fermi model [70] in the following way:

$$V(r) = \frac{Zze^2}{r} \Phi_{sc}\left(\frac{r}{a_{TF}}\right), \tag{1.11}$$

where Φ_{sc} is the screening function, $r = \sqrt{x^2 + y^2 + z^2}$, Z the atomic number, ze the charge of a particle, passing through the crystal, $a_{TF} = (9\pi^2/128Z)^{1/3}a_0$ the Tomas-Fermi screening radius, a_0 the Bohr radius. There are different approximations of atomic potential, depending on the screening function. The first one the Lindhard potential [4], with the screening function $\Phi_{sc}\left(\frac{r}{a_{TF}}\right) = 1 - \left(1 + \frac{3a_{TF}^2}{r^2}\right)^{-1/2}$. The planar potential can be written in the following way:

$$V_{pl}^{L}(x) = 2\pi N d_{pl} Z z e^2 (\sqrt{x^2 + 3a_{TF}^2} - x). \tag{1.12}$$

Another approximation is the Molière potential [71–73] with the screening function $\Phi_{sc}\left(\frac{r}{a_{TF}}\right) = \sum_{i=1}^{3} \alpha_i \exp\left(-\frac{r\beta_i}{a_{TF}}\right)$, where $\alpha = (0.1, 0.55, 0.35)$ and $\beta = (6.0, 1.2, 0.3)$ and the planar potential, having the following form:

$$V_{pl}^{Mol}(x) = 2\pi N d_{pl} Z z e^2 a_{TF} \sum_{i=1}^{3} \frac{\alpha_i}{\beta_i} \exp\left(-\frac{r\beta_i}{a_{TF}}\right). \tag{1.13}$$

The Molière approximation of the planar potential, averaged by thermal vibrations, can be written analytically in the following way:

$$\begin{aligned} &V_{pl0}^{Mol}(x) = 2\pi N d_{pl} Z z e^2 a_{TF} \textstyle\sum_{i=1}^{3} \frac{\alpha_i}{2\beta_i} \exp\left(\frac{\beta_i^2 u_1^2}{2a_{TF}^2}\right) \times \\ &\left[\exp\left(-\frac{x\beta_i}{a_{TF}}\right) \operatorname{erfc}\left(\frac{1}{\sqrt{2}}\left(\frac{u_1\beta_i}{a_{TF}} - \frac{x}{u_1}\right)\right) + \exp\left(\frac{x\beta_i}{a_{TF}}\right) \operatorname{erfc}\left(\frac{1}{\sqrt{2}}\left(\frac{u_1\beta_i}{a_{TF}} + \frac{x}{u_1}\right)\right)\right]. \end{aligned} \tag{1.14}$$

More realistic approximation as well as more simple to operate analytically is the Doyle-Terner approximation [74]:

$$V^{DT}(r) = \frac{2}{\sqrt{\pi}} Z z e^2 a_0 \sum_i \frac{a_i}{B_i^{3/2}} \exp\left(-\frac{r^2}{B_i}\right), \tag{1.15}$$

where $B_i = b_i/4\pi^2$, a_i and b_i are the coefficients, that can be measured experimentally by X-ray diffraction. The direct connection with the experimental data is the main advantage of such approximation. There are a series of works [75–80], providing similar results for the coefficients.

The Doyle-Terner potential (1.15) can be averaged by thermal vibrations (1.5):

$$V_0^{DT}(r) = \frac{2}{\sqrt{\pi}} Z z e^2 a_0 \sum_i \frac{a_i}{(B_i + 2u_1^2)^{3/2}} \exp\left(-\frac{r^2}{B_i + 2u_1^2}\right). \tag{1.16}$$

The corresponding planar and axial Doyle-Terner potential can be written respectively:

$$V_{pl0}^{DT}(x) = 2\sqrt{\pi} N d_{pl} Z z e^2 a_0 \sum_i \frac{a_i}{\sqrt{B_i + 2u_1^2}} \exp\left(-\frac{x^2}{B_i + 2u_1^2}\right); \tag{1.17}$$

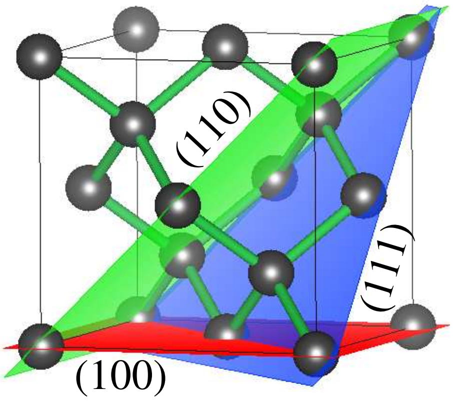

Figure 1.2: Diamond-like lattice.

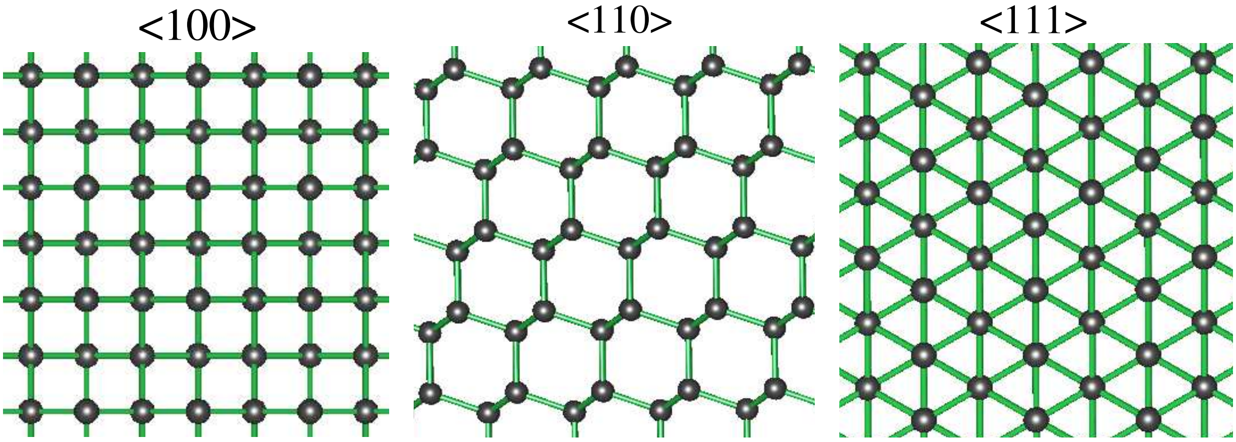

Figure 1.3: Crystal orientation along <100>, <110> and <111> axes of diamond-like lattice.

$$V_{ax0}^{DT}(x,y) = \frac{2}{d_{at}} Zze^2 a_0 \sum_i \frac{a_i}{B_i + 2u_1^2} \exp\left(-\frac{x^2+y^2}{B_i+2u_1^2}\right). \tag{1.18}$$

The materials of diamond-like lattice, namely C, Si, Ge, are widely used in channeling experiments. The structure of the diamond lattice consists of two face-centered cubic lattices shift along the bulk diagonal w.r.t. each other by one quarter of their length [81–83]. This lattice is presented in Fig. 1.2. Several planes and axes are widely used, namely <100>, <110>, <111> and (100), (110) and (111). The planes (100), (110) and (111) are marked in Fig. 1.2, while the direction along the axes <100>, <110>, <111> is shown in Fig. 1.3. The interplanar distances for the crystal planes as well as the interatomic distances for the crystal axes (both formulae and values for Si and Ge) are presented in Table 1.1.

The comparison of different planar potentials is shown in Fig. 1.4 for (100), (110) and (111) silicon planes at room temperature. Hereinafter the coefficients of the Doyle-Terner potential from [78] were used. One can notice, that in contrast to (100) and (110), planes the (111) planes are not equidistant. One

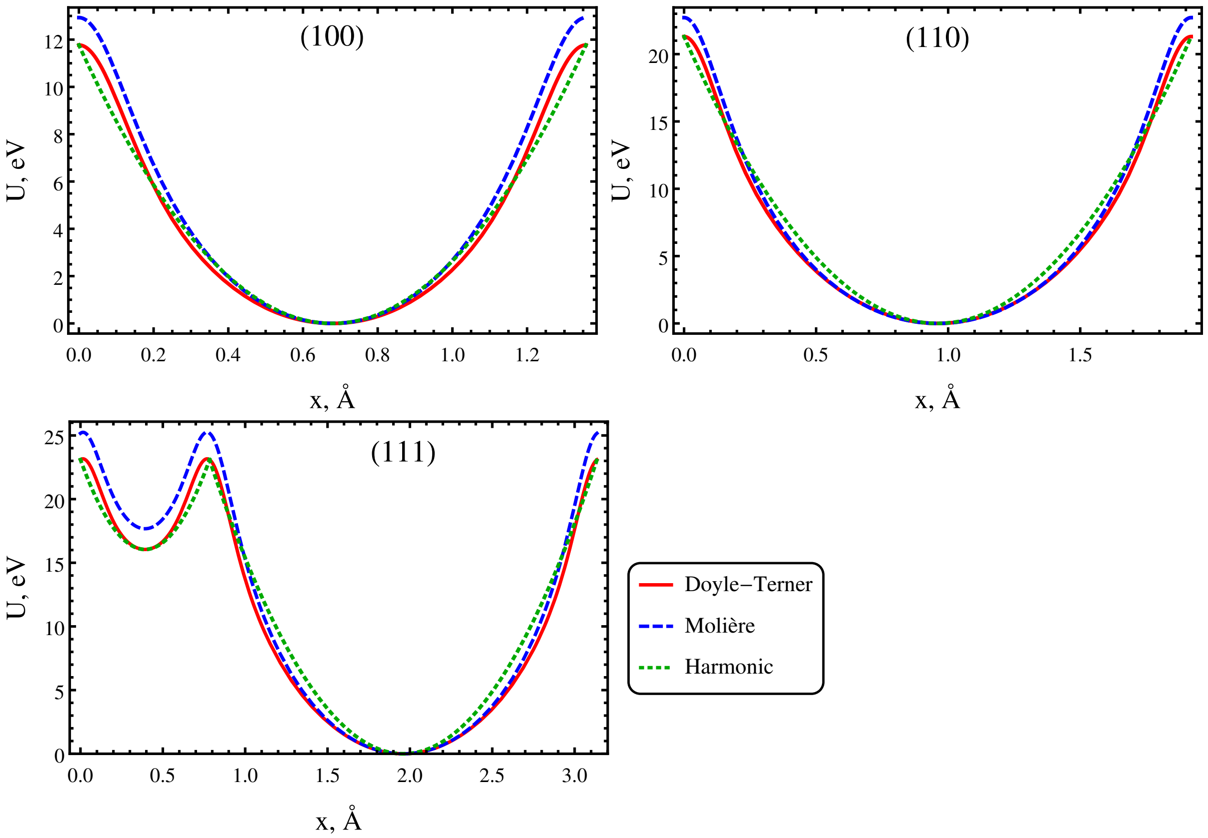

Figure 1.4: Interplanar Doyle-Terner, Molière and harmonic potential for positively charged particles for (100), (110) and (111) silicon planes.

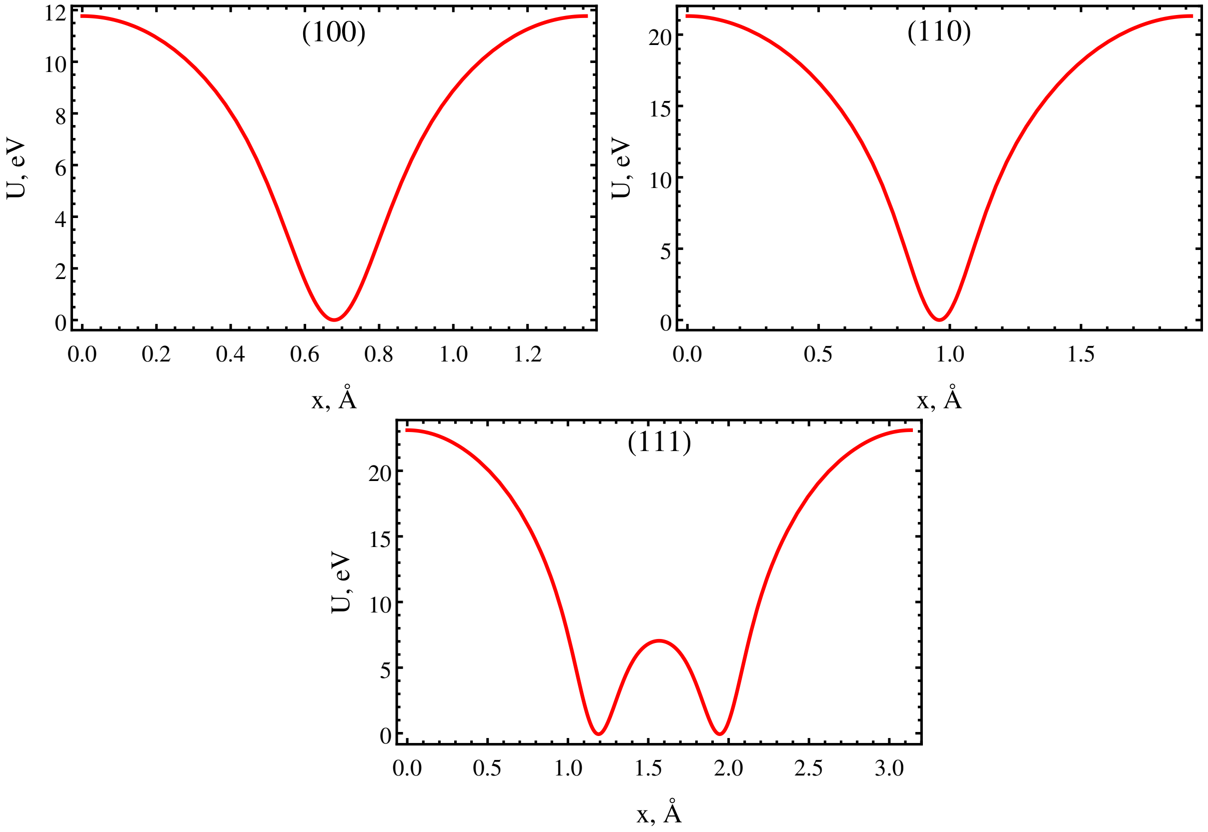

Figure 1.5: Interplanar Doyle-Terner potential for negatively charged particles for (100), (110) and (111) silicon planes

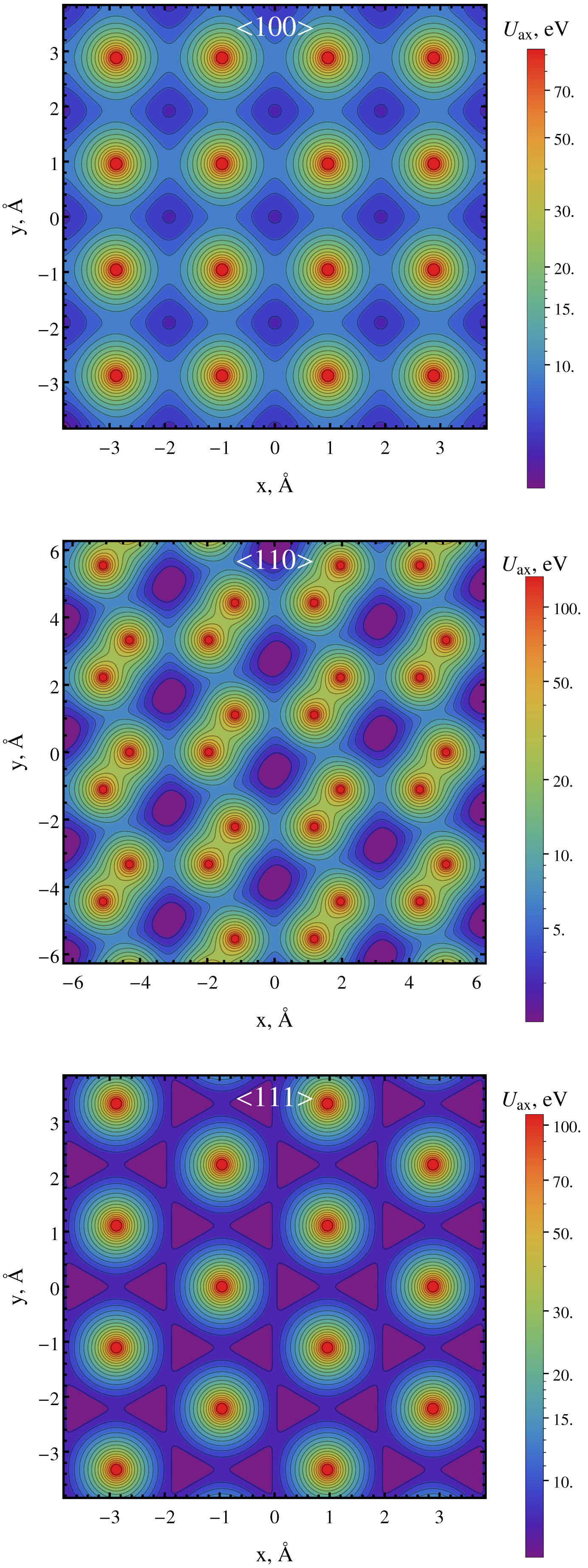

Figure 1.6: Interaxial Doyle-Terner potential for positively charged particles for <100>, <110> and <111> silicon axes.

Table 1.1: Lattice parameters of diamond-like crystals.

Material	Lattice const, Å	i	$d_{pl\ i}$, Å (100)	(110)	(111)	$d_{at\ i}$, Å <100>	<110>	<111>
	a	1	$a/4$	$a/2\sqrt{2}$	$a\sqrt{3}/4$	a	$a/\sqrt{2}$	$3a\sqrt{3}/4$
		2			$a/4\sqrt{3}$			$a\sqrt{3}/4$
Si	5.43	1	1.36	1.92	0.78	5.43	3.84	2.35
		2			2.35			7.05
Ge	5.66	1	1.42	2.00	0.82	5.66	4.00	2.45
		2			2.45			7.35

can also notice a smoothed maximum, caused by thermal vibrations. This kind of potentials is valid for positive particles, while for the negative ones it is turned over, as shown in Fig. 1.5.

The interaxial Doyle-Terner potentials for <100>, <110>, <111> (for positive particles) are shown in Fig. 1.6. One can observe in this figure the structure of atomic strings.

1.1.2 Planar channeling

As it was mentioned above, if a particle hits a bent crystal at a sufficiently small angle w.r.t. its atomic axis or planes, it will be captured in the regime of channeling motion. From the point of view of the potential (Figs. 1.4-1.6) it means underbarrier motion, where the underbarrier part of the potential represents a *channel*.

The channeling motion can be treated by two different approaches, namely by classical and quantum mechanics. The choice depends on both the particle type and its energy and generally depends on the number of quantum levels inside the channel. The number of the levels N_{qm} for planar channeling can be estimated by the following formula [63]:

$$N_{qm} \sim \frac{d_{pl}}{\lambdabar_c}\sqrt{\frac{EU_0}{m^2}}, \tag{1.19}$$

where E is the particle energy, m its mass, $\lambdabar_c$ the reduced Compton length. If the condition $N_{qm} \gg 1$ is valid, a classical approach is applicable. For light particles, namely for electrons and positrons, one can sicurely apply the classical equations starting from the energies of ~100 MeV, being ultrarelativistic. On the other hand for protons and heavy ions one can apply the classical approach even at the energies of several of MeV, meaning non-relativistic particles. Since the results of this work concern only ultrarelativistic energies, starting from $\sim$GeV for electrons and from $\sim 10^2$ GeV for protons, one can assume, that the classical approach is always valid in all the cases, considered below. The quantum approach is described in more details for instance in the following works [57, 59, 61, 63, 64]. Also the radiation, produced by a charged particle, moving in a crystal, is well described in [59, 63, 64, 66–69].

In order to formulate the equations of motion, one must write down the full energy of a particle for the case of atomic planes:

$$E = \sqrt{p_x^2c^2 + p_y^2c^2 + p_z^2c^2 + m^2c^4} + U_{pl}(x) = const, \tag{1.20}$$

where p_x, p_y and p_z are the components of the particle momentum, c speed of light. The y-component, being parallel to the plane, can be included into the longitudinal z-component. Since the condition $p_x \ll p_z$ is always valid for channeling particles (compare the maximal value of potential, being tens of eV and the particle energy) one can extract the transverse component from the square root as:

$$E = p_x^2c^2/E_z + E_z + U_{pl}(x) = const, \tag{1.21}$$

where $E_z = \sqrt{p_z^2c^2 + m^2c^4}$ is the longitudinal energy, while

$$\epsilon = p_x^2c^2/E_z + U_{pl}(x) \tag{1.22}$$

is so-called transverse energy. By assuming $p \approx p_z$ and $E \approx E_z$ as well as by using $p_x = p_z\theta_x$, where θ is the angle of a particle w.r.t. the crystal plane, and $E = pc^2/v$, one can also rewrite (1.22) in the following way:

$$\epsilon = \frac{pv}{2}\theta^2 + U_{pl}(x) = const. \tag{1.23}$$

Let us assume that it is conserved, as already marked in (1.23). Before resolving the particle trajectory one can find the condition of capture of a particle under the channeling conditions, namely $\epsilon \leq U_0$. This can be transformed into the condition of the incident angle:

$$\theta < \theta_L = \sqrt{\frac{2U_0}{pv}}, \tag{1.24}$$

where θ_L is so-called critical channeling angle or *Lindhard* angle.

The trajectory can be calculated from (1.23) by using $\theta_x = \frac{dx}{dz}$:

$$z(x) = \int_{x_0}^{x} \frac{\sqrt{pv}d\chi}{\sqrt{2(\epsilon - U_{pl}(\chi))}}, \tag{1.25}$$

where x_0 is the initial transverse coordinate, while the initial longitudinal coordinate is assumed to be equal to 0. Since no assumptions have been done about under-barrier motion yet, Eq. (1.25) is valid also for the over-barrier motion.

The equation of motion can be written if one finds a derivative on z of the Eq. (1.23):

$$\frac{d^2x}{dz^2} + \frac{U'_{pl}(x)}{pv} = 0. \tag{1.26}$$

Here $U'_{pl}(x)$ represents the interplanar electric field, shown for both silicon and germanium for both (110) and (111) planes in Fig. 1.7. One can notice that in general the electric field for germanium is considerably higher than for silicon. Higher electric field is promising for both particle deflection, since higher deflection angles become possible, and radiation emission intensity. As it will be shown below, the process of deflection is more efficient for higher Z-materials at higher energies of hundreds GeV, while at lower energies scattering influence worsen the efficiency.

For the harmonic approximation of the potential (1.10) one can find an analytical solution of this equation:

$$x = \frac{d_{pl}}{2}\sqrt{\frac{\epsilon}{U_0}}\sin(2\pi\frac{z}{\lambda} + \varphi_0); \tag{1.27}$$

$$\theta = \sqrt{\frac{2\epsilon}{U_0}}\cos(2\pi\frac{z}{\lambda} + \varphi_0), \tag{1.28}$$

where φ_0 is the initial phase, that can be found from initial conditions,

$$\lambda = \pi d_{pl}\sqrt{\frac{pv}{2U_0}} \tag{1.29}$$

is the channeling oscillation length, being usually a good estimate for the real case. In other words, a particle under the planar channeling conditions performs oscillations called *planar channeling oscillations*. Such oscillations are also possible for over-barrier motion at still rather small angles w.r.t. to the crystal planes. These oscillations are called *planar quasichanneling oscillations* as well as such mode of over-barrier motion is called the *quasichanneling* mode.

1.1.3 Axial channeling

When a crystal is aligned along crystal axes, charged particles will move in their potential (see Fig. 1.6). However, the behavior of charged particles of different sign is different. Unlike the planar case (see Figs. 1.4-1.5) in the axial one the potential well depth is different.

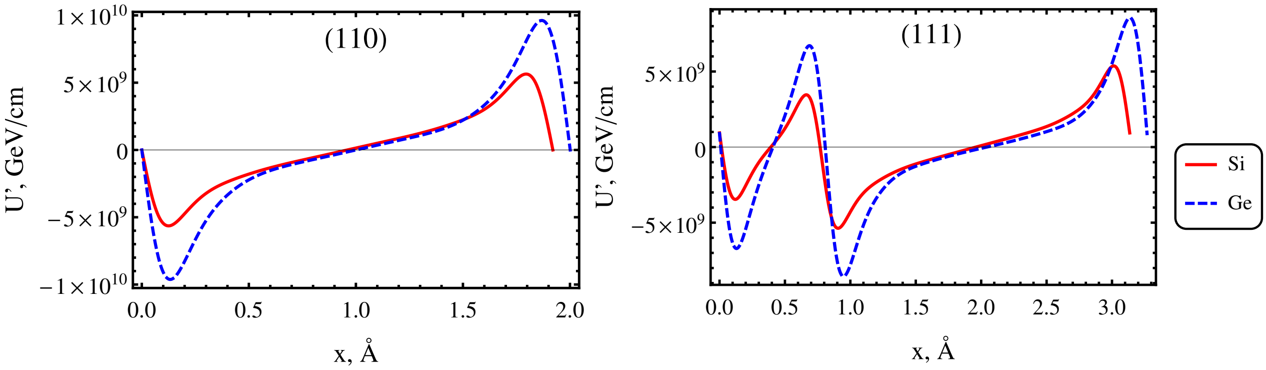

Figure 1.7: Interplanar electric field for both silicon (red, solid) and germanium (blue, dashed) crystals for both (110) (left) and (111) (right) planes in Doyle-Terner approximation.

In the case of positively charged particles it is very low, namely few eV in spite of the potential maximum, being $\sim 10^2$ eV. Since the probability of capture under the channeling conditions is very low, such regime is called hyperchanneling [84]. The remaining part of particles will move freely in transverse direction, sometimes experiencing scattering by atomic strings.

Negatively charged particles can be captured under the axial channeling conditions by profound potential wells (being potential maximum for positively charged particles).

Apart the transverse energy, transverse motion in interaxial potential is characterized by angular momentum L. The angle θ of particle incidence w.r.t. a crystal axis can be factorized [85] by radial $\theta_r = dr/dz$ and azimutal $\theta_\varphi = rd\varphi/dz$ components: $\theta^2 = \theta_r^2 + \theta_\varphi^2$, where $r^2 = x^2 + y^2$ is the radial coordinate. The conserved angular momentum has the form $L = p\theta_\varphi r = pr^2 d\varphi/dz$. Consequently, the transverse energy (1.23) can be written as:

$$\epsilon = \frac{pv}{2}\theta^2 + U_{ax}(r) = \frac{pv}{2}\left(\frac{dr}{dz}\right)^2 + \frac{L^2}{2m\gamma r^2} + U_{ax}(r) = const, \qquad (1.30)$$

where the following relativistic expression was used $p = \gamma m v$, γ is the Lorentz factor. One can notice that here an assumption of radial symmetry of the potential $U_{ax}(r)$, which is nearly correct not far form the center of the axis. In analogy to the planar case (see (1.25)) the particle trajectory can be extracted in the following way:

$$z(r) = \int_{r_0}^{r} \frac{\sqrt{pv}\,d\rho}{\sqrt{2(\epsilon - U_{pl}(\rho)) - \frac{L^2}{2m\gamma\rho^2}}}. \qquad (1.31)$$

Taking into account $d\varphi = dzL/pr^2$, one also find the trajectory in the transverse plane:

$$\varphi(r) = \int_{r_0}^{r} \frac{L/\sqrt{m\gamma}\rho^2 d\rho}{\sqrt{2(\epsilon - U_{pl}(\rho)) - \frac{L^2}{2m\gamma\rho^2}}}. \tag{1.32}$$

However, in real situation one must take into account that the symmetry of interaxial field is not radial. Therefore, one can switch to the Cartesian coordinate system, in which $\theta^2 = \theta_x^2 + \theta_y^2$, $\theta_x = dx/dz$, $\theta_y = dy/dz$ and the equation (1.30) can be rewritten as:

$$\epsilon = \frac{pv}{2}\theta^2 + U_{ax}(x,y) = \frac{pv}{2}(\theta_x^2 + \theta_y^2) + U_{ax}(x,y) = const. \tag{1.33}$$

Differentiation by z will give the system of equations, analogical to (1.26):

$$\begin{cases} \dfrac{d^2x}{dz^2} + \dfrac{U'_{ax\ x}}{pv} = 0; \\ \dfrac{d^2y}{dz^2} + \dfrac{U'_{ax\ y}}{pv} = 0. \end{cases} \tag{1.34}$$

The Lindhard angle for axial channeling can be found analogically to the planar case as

$$\theta_{Lax} = \sqrt{\frac{2U_{0ax}}{pv}}, \tag{1.35}$$

where U_{0ax} is the potential well depth of the axial channel. Since the maximal value of the axial potential is higher than that of the planar one with a factor of ~ 5, the axial Lindhard angle for negatively charged particles is 2–3 times higher than the planar one. In other words, atomic strings possess stronger electric field than that of planes, which potentially provides stronger deflection as well as radiation effects. For positively charged particles the Lindhard angle is several times smaller. Nevertheless the strength of electric field is the same on module, therefore the possibilities for deflection and radiation are valid also for positively charged particles.

1.1.4 Multiple and single scattering

Incoherent scattering on nuclei and electrons can break the trasverse energy conservation law (1.23, 1.30, 1.33) and change the particle trajectory.

There are several kinds of incoherent scattering in a crystal media:

1) Coulomb scattering;

2) nuclear elastic (no loss of a particle; no energy loss);

3) nuclear quasielastic (no loss of a particle; energy loss; disintegration of the nucleus, on which scattering occurs);

4) nuclear inelastic (particle loss; disintegration of the nucleus, on which scattering occurs).

The first type of scattering is Coulomb scattering. A particle can be scattered by a screened atomic potential as a whole or by a single electron, causing atom ionization.

Coulomb scattering on atom can be treated by a well fitted cross section of screened atom [71,86,87], based on Yukawa potential:

$$\frac{d\sigma_C}{d\Omega} = 4\frac{z^2Z^2e^4}{p^2v^2}\frac{1}{(\vartheta^2+\vartheta_1^2)^2}, \tag{1.36}$$

where $\vartheta_1 = \hbar\sqrt{1.13+3.76(zZe^2/\hbar v)}/(pa_{TF})$ is the so-called characteristic scattering angle [71,86], $d\Omega$ is the element of a solid angle.

By using this cross section and taking into account $d\Omega = \vartheta d\vartheta d\varphi$ one can find the r.m.s. angle of multiple scattering in a material of thickness Δz. However, one must take into account that in a crystal the scattering cross section is divided onto coherent and incoherent part [66,88]:

$$\frac{d\sigma_C}{d\Omega} = \frac{d\sigma_C}{d\Omega}_{inc} + \frac{d\sigma_C}{d\Omega}_{coh}, \tag{1.37}$$

where the incoherent part can be expressed from (1.36) by using the Debye-Waller factor $\exp(-p^2\vartheta^2u_1^2)$:

$$\frac{d\sigma_C}{d\Omega}_{inc} = \frac{d\sigma_C}{d\Omega}\left(1-\exp(-p^2\vartheta^2u_1^2)\right). \tag{1.38}$$

Therefore the r.m.s. multiple scattering angle can be written as:

$$<\vartheta_{Cms}^2> = <n_N> \Delta z \int_0^{\vartheta_2}\int_0^{2\pi}\frac{d\sigma_C}{d\Omega}\left(1-\exp(-p^2\vartheta^2u_1^2)\right)d\varphi\vartheta d\vartheta, \tag{1.39}$$

where $<n_N>$ is the average nuclear density along the trajectory element Δz. The direct calculations lead to the following equation:

$$<\vartheta_{Cms}^2> = 4\pi <n_N> \Delta z\left(\frac{zZe^2}{pv}\right)^2\left[\ln\left(1+\left(\frac{\vartheta_2}{\vartheta_1}\right)^2\right)+\left(1+p^2\vartheta_1^2u_1^2\right)\times\right.$$
$$\left.\exp\left(p^2\vartheta_1^2u_1^2\right)\left(E_1\left(p^2\left(\vartheta_1^2+\vartheta_2^2\right)u_1^2\right)-E_1\left(p^2\vartheta_1^2u_1^2\right)\right)+\frac{1-\exp\left(-p^2\vartheta_2^2u_1^2\right)}{1+\left(\frac{\vartheta_2}{\vartheta_1}\right)^2}\right], \tag{1.40}$$

where $E_1(x) = \int_x^\infty \exp(-t)dt/t$ is the exponential integral. The angle ϑ_2 is the angle, limiting multiple scattering. Indeed, according to Molière [71,86], the scattering distribution possesses a nearly gaussian form only in the center (in zero approximation), having long non-gaussian tales. Therefore the single scattering events on atom must be treated separately [62, 69, 88–92] according to (1.36, 1.38).

Any type of single scattering events is defined by scattering length L_{sc}, that is the length, used in the exponential cumulative distribution function for the probability of scattering:

$$F_{sc}(s) = \exp\left(-s/L_{sc}\right), \tag{1.41}$$

where s markes the passed distance. Any scattering length can be calculated by using the cross section of such event σ_{sc} and the nuclear density, averaged along the trajectory:

$$L_{sc} = 1/ < n_N > \sigma_{sc}. \tag{1.42}$$

The cross section of single Coulomb scattering on an atom can be calculated by integration (1.36):

$$\sigma_{Css} = 2\pi \int_{\vartheta_2}^{\vartheta_{max}} \frac{d\sigma_C}{d\Omega} \vartheta d\vartheta = 4\pi \left(\frac{zZe^2}{pv}\right)^2 \left(\frac{1}{\vartheta_1^2 + \vartheta_2^2} - \frac{1}{\vartheta_1^2 + \vartheta_{max}^2}\right), \tag{1.43}$$

where $\vartheta_{max} = \hbar/pR_N$ is the maximal scattering angle, determined by the nucleus radius R_N, providing the length of the next Coulomb single scattering as:

$$L_{Css} = 1/ \left(4\pi < n_N > \left(\frac{zZe^2}{pv}\right)^2 \left(\frac{1}{\vartheta_1^2 + \vartheta_2^2} - \frac{1}{\vartheta_1^2 + \vartheta_{max}^2}\right)\right). \tag{1.44}$$

Another type of single scattering event is scattering on electrons. Its cross section is represented by a “usual” Rutherford cross section [93]:

$$\frac{d\sigma_{Ce}}{d\Omega} = 4\frac{z^2e^4}{p^2v^2}\frac{1}{\vartheta^4}. \tag{1.45}$$

However, the main parameter, defining scattering on electrons is the kinetic energy, transfered to electron $T_e = p^2\vartheta^2/2m_e$, where m_e is the electron mass. Therefore, in order to find the electron cross section, one must use the formula, similar to (1.43) and substitute under the integral ϑ by T:

$$\sigma_{ess} = \int_{T_{min}}^{T_{max}} \frac{d\sigma_{Ce}}{dT} dT = 4\pi \left(\frac{ze^2}{v}\right)^2 \left(\frac{1}{2mT_{min}} - \frac{1}{2mT_{max}}\right), \tag{1.46}$$

where $T_{max} = 2m_e(\gamma\beta)^2/(1 + 2m_e\gamma/m + (m_e/m)^2)$ is the maximal energy that can be lost for ionization [94], while T_{min} is the ionization potential that can be

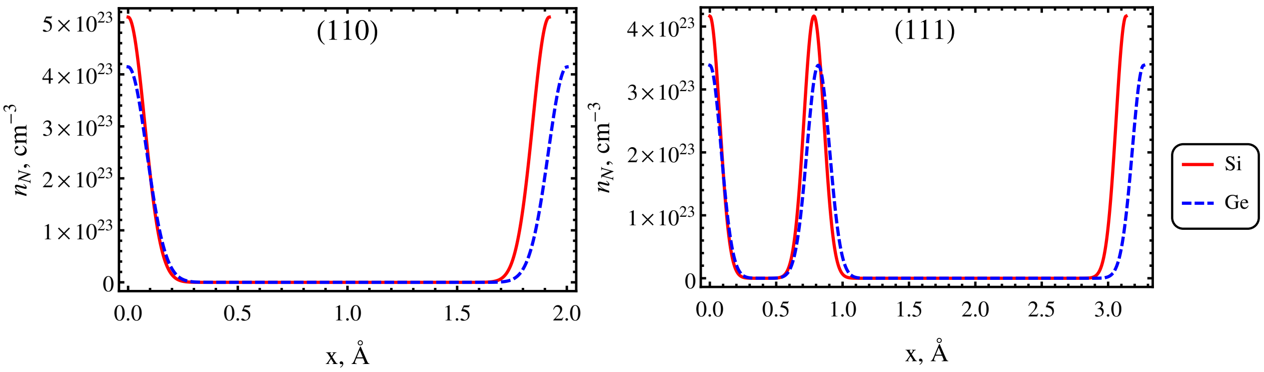

Figure 1.8: Interplanar nuclear density for both silicon (red, solid) and germanium (blue, dashed) crystals for both (110) (left) and (111) (right) planes.

found as the Fermi energy at the point of scattering, $\beta = v/c$. Consequently, the length of the next single Coulomb scattering on electron can be calculated similarly to (1.44):

$$L_{Ce} = 1/\left(4\pi < n_e > \left(\frac{ze^2}{v}\right)^2 \left(\frac{1}{2mT_{min}} - \frac{1}{2mT_{max}}\right)\right), \tag{1.47}$$

where $< n_e >$ is the averaged electronic density along the trajectory.

Nuclear scattering is important only for channeling hadrons (protons, ions). The length of nuclear scattering events L_{el}, L_{diff}, L_{inel} (elastic, diffractive and inelastic respectively) almost do not depend on the energy and can be usually found in the literature [94] for any type of material. One must only recalculate this length, taking into account the atomic density along the trajectory:

$$L_{sc} < n_N > /N. \tag{1.48}$$

Since all types of scattering depend on the nuclear and electron density distributions, it is important to calculate them for the channels, considered above (see Figs. 1.6,1.7). The nuclear density is proportional to the distribution of thermal oscillations (1.6–1.7):

$$n_{Npl}(x) = Nd_{pl}w_{pl}(x) = \frac{Nd_{pl}}{\sqrt{2\pi u_1^2}} \exp\left(-\frac{x^2}{2u_1^2}\right); \tag{1.49}$$

$$n_{Nax}(x,y) = w_{ax}(x,y)/d_{at} = \frac{1}{2\pi d_{at} u_1^2} \exp\left(-\frac{x^2+y^2}{2u_1^2}\right). \tag{1.50}$$

The corresponding distribution for both (110) and (111) planes for both Si and Ge crystals is shown in Fig. 1.8.

The electron density distribution n_e can be found by using the Poisson equation $\Delta U = 4\pi e^2(n_e + Zn_N)$. One can find both interplanar n_{epl} and interaxial n_{eax} electric density as

$$n_{epl}(x) = \frac{U''_{pl}(x)}{4\pi e^2} - Zn_{Npl}(x); \tag{1.51}$$

$$n_{eax}(x,y) = \frac{\Delta U_{ax}(x,y)}{4\pi e^2} - Zn_{Nax}(x,y). \tag{1.52}$$

The corresponding distribution for both (110) and (111) planes for both Si and Ge crystals is shown in Fig. 1.9. One can notice that the electron density for germanium is more than twice higher, resulting in higher probability of single scattering on electrons the for Si.

1.1.5 Dechanneling

Particle scattering considered above may cause change of transverse energy (1.23,1.33), which can be expressed in the following way:

$$\Delta\epsilon = \epsilon + \Delta\epsilon - \epsilon = \frac{pv}{2}(\theta + \vartheta)^2 - \frac{pv}{2}\theta^2 = pv\theta\vartheta + \frac{pv}{2}\vartheta^2. \tag{1.53}$$

Moreover the energy change can be strong enough that a channeling particle can become the overbarrier one. This process is called *dechanneling* [4,57–65,95–98].

Since scattering is possible on either nuclei or electrons, two types of dechanneling can be marked out, namely nuclear and electronic dechanneling. Scattering on nuclei is considerably stronger than that on electrons. Therefore it should be the main reason of particle escape the channeling conditions.

However, there is a strong difference between channeling of positively and negatively charged particles. For negative particles the atoms are placed in the

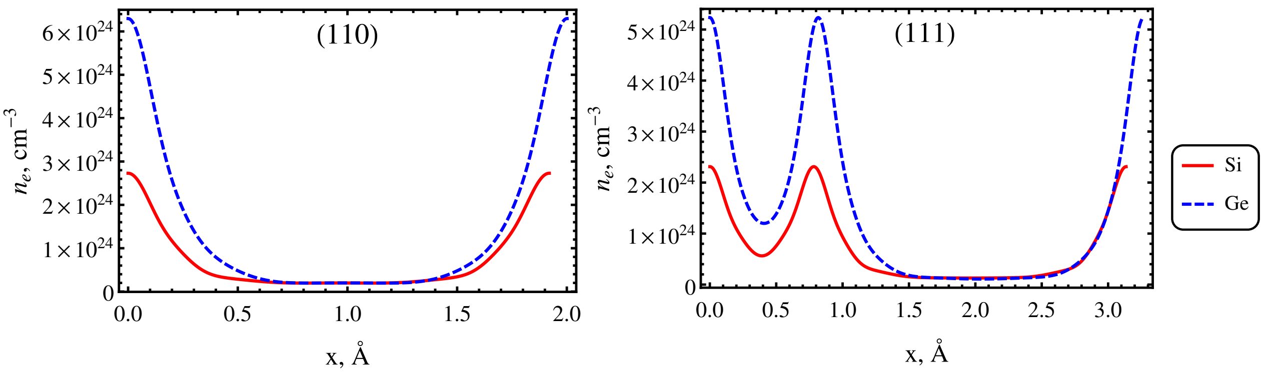

Figure 1.9: Interplanar electron density for both silicon (red, solid) and germanium (blue, dashed) crystals for both (110) (left) and (111) (right) planes.

center of the channel, while for the positive ones they are at the channel boundary (see Figs. 1.3-1.6). This means strong influence of nuclear dechanneling for the negative particles and relatively weak for the positive ones. Moreover, by this reason there is no sense to differ electronic and nuclear dechanneling for negatively charged particles, because of higher contribution of nuclear dechanneling w.r.t. the electronic one. In opposite, for positive perticles the nuclear scattering is suppressed outside a thin zone, being near the atomic plane, defined by the Tomas-Fermi screening radius [61, 62] $\sim \pm a_{TF} = x_{cr}$. In the remaining part of the channel electronic dechanneling makes the principle contribution.

The process of transverse energy increase can be described in terms of the diffusion theory [62, 95–97]. The simplest case, namely electronic dechanneling of positively charged particles under planar channeling conditions is well treated by the diffusion equation:

$$\frac{\partial F}{\partial z} = \frac{1}{2}\frac{\partial}{\partial \epsilon}\left(D_e(\epsilon)\frac{\partial F}{\partial \epsilon}\right), \tag{1.54}$$

where F is the distribution function, D_e the diffusion coefficient. The transverse energy is assumed to be less than the critical trasverse energy value $\epsilon < E_{cr}$ where the nuclear dechanneling is suppressed, namely the level of the energy at x_{cr}: $E_{cr} = U_{pl}(x_{cr})$. Assuming [62, 96, 97] $D_e = D_{e0}\epsilon$ one obtains the solution in the following form:

$$F(z,\epsilon) = \sum_{k=1}^{\infty} C_k J_0\left(j_{0,k}\sqrt{\frac{\epsilon}{E_{cr}}}\right)\exp\left(-\frac{j_{0,k}D_{e0}z}{4E_{cr}}\right), \tag{1.55}$$

where $j_{0,k}$ is the k-th zero of the Bessel function J_0, C_k follows from the particle initial distribution on the transverse energy $F_0(\epsilon)$:

$$C_k = \frac{1}{J_1^2(j_{0,k})E_{cr}}\int_0^{E_{cr}} F_0(\epsilon)J_0\left(j_{0,k}\sqrt{\frac{\epsilon}{E_{cr}}}\right)d\epsilon. \tag{1.56}$$

The dechanneling length can be determined by the exponent function in (1.55). Since $j_{0,1}$ is several times lower than $j_{0,2}$ etc. the items with $k > 1$ are suppressed. Therefore one can define the dechanneling length from the first item of (1.55) in the following way:

$$L_{edech0} = \frac{4E_{cr}}{j_{0,1}^2 D_{e0}} = \frac{256}{9\pi^2}\frac{pv}{\ln(2\gamma m_e c^2/I) - 1}\frac{a_{TF}d_{pl}}{zZe^2}, \tag{1.57}$$

where I is the ionization potential. Moreover, this defines the exponential low of channeling fraction η_{ch} (the number of particles being under channeling

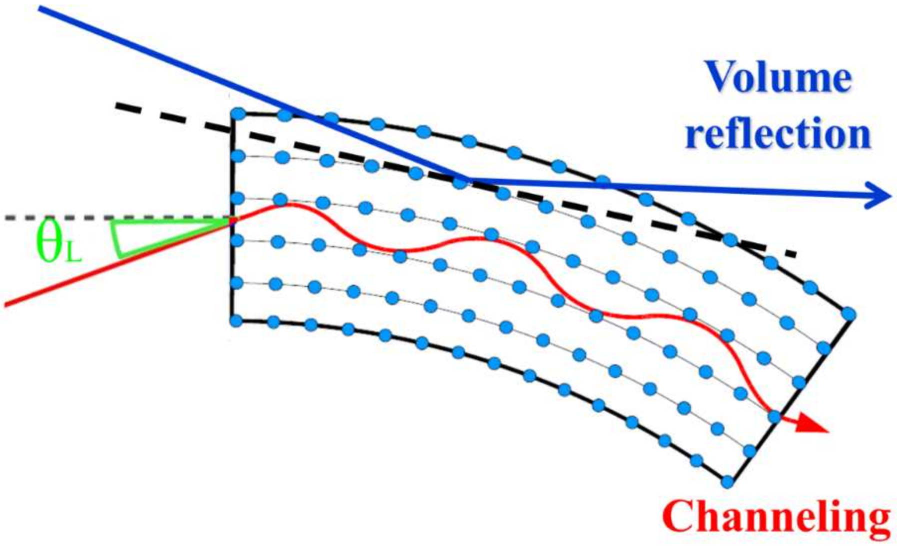

Figure 1.10: Channeling and volume reflection in a bent crystal.

conditions at the longitudinal coordinate z w.r.t. the number of all the particles, passing the crystal at the same coordinate) decrease:

$$\eta_{ch} = \eta_{ch0} \exp\left(-z/L_{edech0}\right), \tag{1.58}$$

where η_{ch0} is the initial channeling efficiency value. One can do also a conclusion that the electronic dechanneling length in a straight crystal increases almost proportionally to the energy value. The exponential dependence (1.58) is also valid in some cases for the nuclear dechanneling length L_{ndech0}, which will be discussed later.

Note that the planar oscillation length (1.29) is proportional to the square root from the energy. Such dependence can be explained by the fact that the scattering angle (see above) is inversely proportional to the energy while the critical channeling angle (1.24) to the square root from the energy.

Therefore, one can conclude that the channeling conditions become more pronounced at higher energies, while incoherent scattering becomes more suppressed.

1.2 Coherent effects in a bent crystal

1.2.1 Channeling

The main idea of beam steering in a bent crystal [5] is to deflect a particle beam following bent crystal planes or axes as schematically shown in Fig. 1.10. The simplest example of coherent effect for beam steering in a bent crystal is the channeling effect.

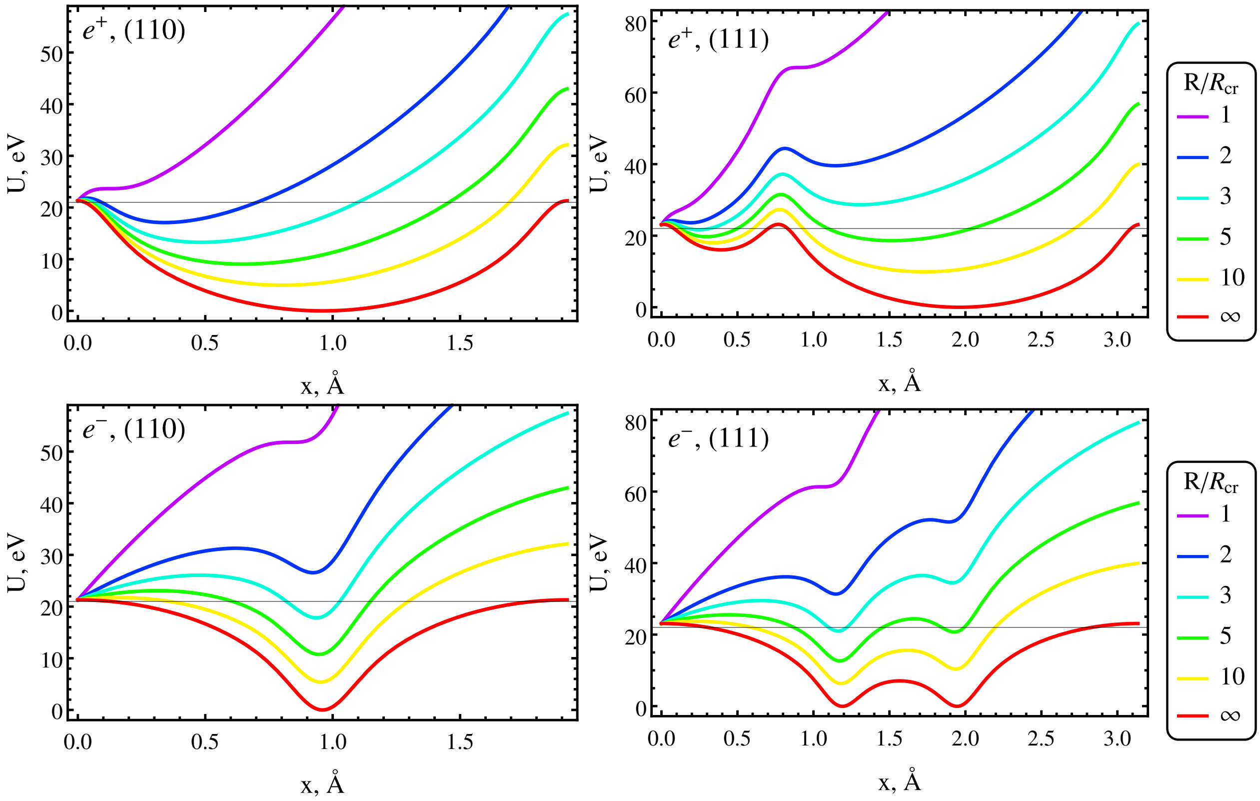

Figure 1.11: Interplanar potential in a bent silicon crystal of different bending radius for both (110) (left) and (111) (right) planes for both positively (top) and negatively charged particles (bottom).

The main difference of the potential well is the centrifugal term pv/R, where R is the crystal bending radius. This results in the effective interplanar potential, that can be written as[2]:

$$U_{eff\ pl}(x) = U_{pl}(x) + pvx/R \tag{1.59}$$

for the planar case and

$$U_{eff\ ax}(x, y) = U_{ax}(x, y) + pvx/R \tag{1.60}$$

for the axial one, assuming horizontal bending. An example of Doyle-Terner interplanar potential in a bent crystal is in Fig. 1.11 for both positively and negatively charged particles. One can notice, that the channeling effect is still possible, though the potential well depth becomes lower with decrease of bending radius. The transverse electric field is shifted in a vertical direction on the value pv/R.

$$U'_{eff\ x} = U'_x + pv/R, \tag{1.61}$$

---

[2] Sometimes this potential will be marked as $U_{eff}(x)$, where only the planar case is considered.

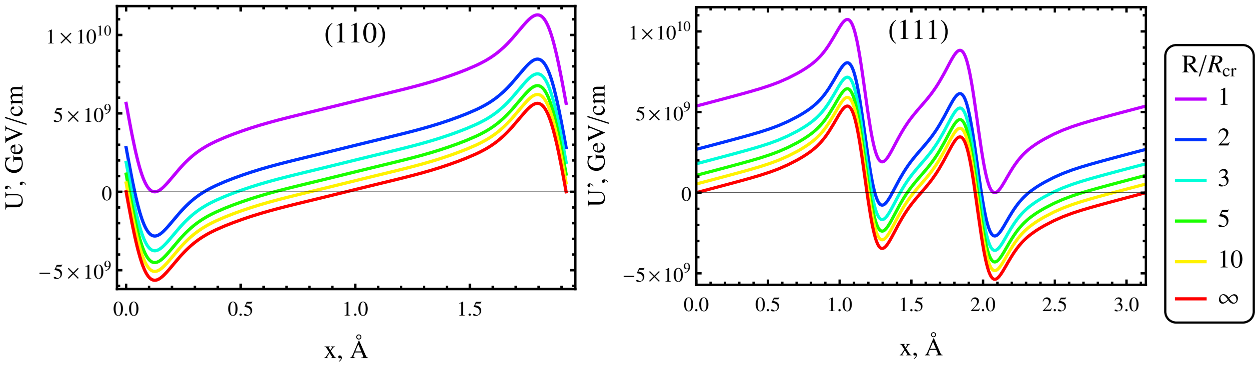

Figure 1.12: Interplanar electric field in a bent silicon crystal of different bending radius for both (110) (left) and (111) (right) planes.

being valid for both planar and axial cases. The example of electric field for the planar case is shown in Fig. 1.12. The planar channeling effect is still possible, when the electric field can change the sign, representing the extrema condition. This is possible, when the maximal electric field E_0 is higher than $1/R$, giving the critical radius value:

$$R_{cr} = \frac{pv}{E_0}. \tag{1.62}$$

One can notice that the critical radius is proportional to the energy. Consequently one may suppose that if one fixes the potential well shape, when increasing the energy, one must reduce the bending angle, being:

$$\theta_b = \frac{l_{cr}}{R}, \tag{1.63}$$

where l_{cr} is the crystal length. However, as has been discussed above, the dechanneling length is nearly proportional to the particle energy (1.57), which is valid also for a bent crystal of fixed potential well shape. In particular, it can be estimated in the harmonic approximation (1.10) in the following way [62,65]:

$$L_{edech} = L_{edech0}(1 - \frac{R_{cr}}{R})^2. \tag{1.64}$$

In other words, one can increase the crystal length, proportionally to pv, achieving the same channeling efficiency for the same bending angle.

Unfortunately, there are other limits, restricting the crystal length growth. Apart the logarithmic term in the denominator of Eq. (1.57), it is the inelastic loss rate (essential for channeling hadrons), with a weak dependence on the energy.

The Lindhard angle (1.24) is also changed, since the potential well depth decreases w.r.t. that of the straight crystal. One can generalize the Lindhard angle also for a bent crystal by using the right value U_0 of the potential well depth.

In order to rewrite the equations of motion, one must replace the potential in the transverse energy expressions (1.23,1.33) by the effective one (1.59-1.60):

$$\epsilon = \frac{pv}{2}\theta^2 + U_{pl}(x) + \frac{pvx}{R} = const, \tag{1.65}$$

$$\epsilon = \frac{pv}{2}\theta^2 + U_{pl,ax}(x,y) + \frac{pvx}{R} = const. \tag{1.66}$$

for the planar and the axial cases respectively, giving the equations of motion:

$$\frac{d^2x}{dz^2} + \frac{U'_{pl\ x}}{pv} + \frac{1}{R} = 0, \tag{1.67}$$

$$\begin{cases} \dfrac{d^2x}{dz^2} + \dfrac{U'_{ax\ x}}{pv} + \dfrac{1}{R} = 0; \\ \dfrac{d^2y}{dz^2} + \dfrac{U'_{ax\ y}}{pv} = 0. \end{cases} \tag{1.68}$$

Therefore, the conditions of the channeling effect in a bent crystal are the incident angle to be less than the Lindhard angle as well as the bending radius to be more than the critical one. Obviously the channeling efficiency in a bent crystal depends not only on the crystal length and particle energy but also on the rate R/R_{cr}, which will be discussed later.

1.2.2 Volume reflection

Another effect becomes possible in a bent crystal, being not possible in a straight one. When an overbarrier particle flies towards a bent crystal plane, it may be reflected in opposite direction, as schematically shown in Fig. 1.10. This effect is called the volume reflection effect [6, 7].

Volume reflection can be simply illustrated on the potential well diagram Fig. 1.13. This effect may occur, if a particle moves towards a potential barrier on which it will be reflected. The volume reflection effect is possible at negative angles of crystal alignment θ_{cr}, i.e. positive incident angles θ_{x0} (see Fig. 1.10), otherwise it will initially move away from the reflection point and a reflection will not occur. However it must not exceed on module the crystal bending angle, or the particle will not achieve the reflection point. This condition of volume reflection can be written in the following way:

$$0 < \theta_{x0} < \theta_b. \tag{1.69}$$

The angle of volume reflection is not constant and depends on bending radius as well as on the transverse energy value. Indeed, the trajectory of a particle

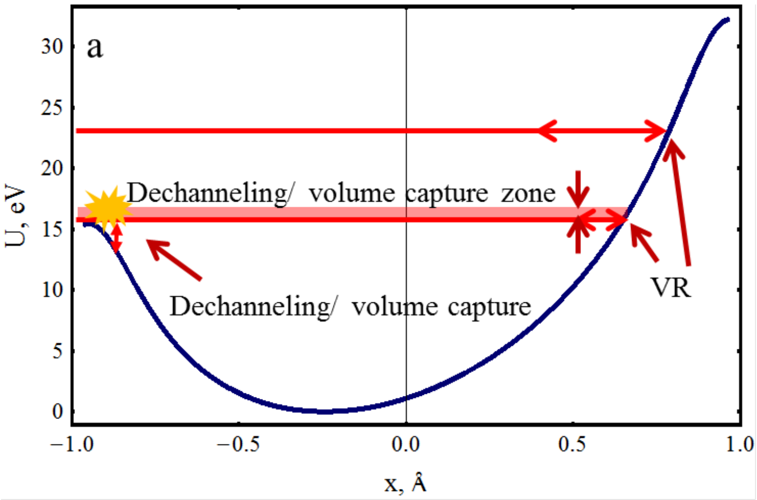

Figure 1.13: The interplanar potential well for the bent Si (110) crystal of 4 mm length and 50 μrad bending angle for 7 TeV protons.

can be calculated by using the trasverse energy expression (1.65) analogically to (1.25):

$$z(x) = \int_{x_0}^{x} \frac{\sqrt{pv}d\chi}{\sqrt{2(\epsilon - U_{pl}(\chi) - pv\chi/R)}}. \tag{1.70}$$

The coordinate z is the coordinate in a co-rotating reference system, directed along a bent crystal plane. By division this coordinate by the bending radius (compare Eq. (1.63)) one can transform it to the angle of deflection by bent crystal planes. However, it is necessary to take into account that this is not channeling but over-barrier motion. Therefore one must subtract from (1.70) the coordinate, obtained by (1.70) but with “switched off” interplanar potential:

$$z_0(x) = \int_{x_0}^{x} \frac{\sqrt{pv}d\chi}{\sqrt{2(\epsilon - U_{pl}(x_{ref}(\epsilon)) - pv\chi/R)}}, \tag{1.71}$$

where x_{ref} is the coordinate of the reflection point. Taking into account also both parts of a trajectory to and from the reflection point, one obtains the angle of volume reflection [6, 7, 99, 100]:

$$\alpha = 2\frac{z(x_{ref}) - z_0(x_{ref})}{R} = \\ \int_{x_0}^{x_{ref}} \left(\frac{\sqrt{2pv}}{\sqrt{\epsilon - U_{pl}(\chi) - \frac{pv\chi}{R}}} - \frac{\sqrt{2pv}}{\sqrt{\epsilon - U_{pl}(x_{ref}(\epsilon)) - \frac{pv\chi}{R}}} \right) d\chi, \tag{1.72}$$

which confirms the dependence of the volume reflection effect on the bending radius as well as on the energy and the potential well shape. Qualitatively the trends of this dependence can be explained in terms of the potential well (Fig. 1.13). The time of a particle approach to the reflection point depends on its distance from the point of potential maximum. In classical mechanics [85] it is proved that this time increases if the reflection point approaches to the point of maximum, tending to infinity.

Therefore, in order to increase the volume reflection angle, one must make the bending radius as high as possible. Though α will never go to infinity but tend to a constant level, it may exceed the critical channeling angle up to 50%. More detailed investigation of the volume reflection process, both theoretical and experimental is described below.

1.2.3 Dechanneling, volume capture and rechanneling

Since incoherent scattering can change the transverse energy of a charged particle, the latter can either enter or escape the channeling mode. The process of a particle escape the channeling conditions, so-called dechanneling, has been considered above. The dependence of the channeling fraction of the penetration depth can be approximated (not always [98]) by the exponential low:

$$\eta_{ch} = \eta_{ch\ n} \exp\left(-z/L_{ndech0}\right) + \eta_{ch\ e} \exp\left(-z/L_{edech0}\right), \tag{1.73}$$

where $\eta_{ch\ n}$ and $\eta_{ch\ e}$ are the fractions of channeling particles inside and outside the zone of nuclear scattering influence (x_{cr}). Since in the case of negative particles all of them cross the atomic plane during their motion, only the first item of (1.73) can be considered.

The process of volume capture [101–104] is an inverse process w.r.t. dechanneling. In other words, an initially overbarrier particle, flying towards the volume reflection point, can be scattered, when passing the atomic plane, and captured under the channeling conditions as shown in Fig. 1.13. Though in theory nothing prevents the same process in a straight crystal, only in a bent one a trasverse energy value can approach the value of potential barrier due to centrifugal term (see (1.59)). The conditions of volume capture generally concide with the conditions of volume reflection.

Therefore, due to the process of volume capture the channeling effect becomes possible not only for the angles of crystal alignment, lower than the Lindhard angle but also beyond this range. The condition is the same as for volume reflection (1.69). However, evidently the channeling efficiency of volume captured particles will be considerably less than that of initially channeling particles.

There is a value of crystal alignment, being optimal for volume capture manifestation, namely $\theta_{cr} = -\theta_b$ or

$$\theta_{x0} = \theta_b, \tag{1.74}$$

when a particle reaches the volume reflection point nearly at the end of the crystal. In such a way a particle remains under the channeling conditions by the end of the crystal. In fact the transverse energy value remains still close to that of volume reflected particle, so one has mixing of both volume capture and volume reflection.

It is important that even dechanneled particle can be recaptured again under the channeling conditions also due to incoherent scattering. This process, so-called rechanneling can be followed again by dechanneling and so on. One must underline here that the influence of the processes of dechanneling and rechanneling on the channeling efficiency are considerably higher for negatively charged particles than for the positive ones [29]. This is explained by the position of the crystal planes, being at the channel boundary for positive particles and in the channel center for the negative ones.

All these processes are considered in more details both experimentally and by simulations in the following chapters.

1.2.4 Coherent effects in the field of atomic strings in a bent crystal

Axial channeling, considered above for straight crystal remains valid also for the bent one. However, for positively charged particles the potential well depth is low, while for negative particles it is high but incoherent scattering on atomic strings, being in the channel center, contribute a lot. Therefore most of particle become overbarrier. By this reason the main contribution is made by coherent action of several atomic strings and their interference, represented by skew crystal planes, shown in Fig. 1.2.4 on example of the <111> axis (compare also Fig. 1.6). One can notice a lot crystal planes, intersected by the same axis. The electric field strength of various planes is different, because of different 2-dimensional atomic concentration inside a plane. The strongest planes are (110), one of which is vertical in Fig. 1.2.4.

If a particle angle is low enough w.r.t. some skew crystal planes, this particle can be reflected by means of volume reflection or even be captured under the channeling conditions by these skew planes. In other words, all the effects, considered above for vertical bent crystal planes, are also valid for the skew ones. The only difference is that the centrifugal component is not directed normally w.r.t. the plane. Therefore, there is a components of centrifugal force, directed normally and along the skew crystal plane. If one chooses the direction of x and y coordinate as normal and tangential, the equations of motion (1.67)

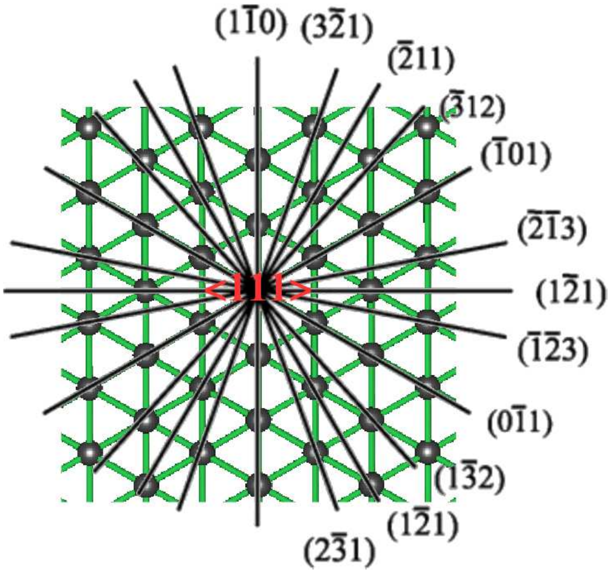

Figure 1.14: Skew crystal planes, intersecting by the ¡111¿ axis.

will be rewritten as:

$$\begin{cases} \dfrac{d^2x}{dz^2} + \dfrac{U'_{pl\ x}}{pv} + \dfrac{1}{R}\cos\alpha_{pl} = 0; \\ \dfrac{d^2y}{dz^2} + \dfrac{1}{R}\sin\alpha_{pl} = 0, \end{cases} \tag{1.75}$$

where α_{pl} is the angle of inclination a skew crystal plane (for the vertical one $\alpha_{pl} = \pi/2$). In other words, one can introduce an effective bending radia of a skew plane $R_x = R/\cos\alpha_{pl}$ and $R_y = R/\sin\alpha_{pl}$, application of which in (1.75) leads to the same description of channeling, dechanneling, volume reflection, volume capture, etc. as previously.

In a real situation some particles are captured under the channeling conditions at the orientation, being optimal for axial channeling. The overbarrier particle can experience consequent scattering on several atomic strings, also causing beam deflection in the direction of crystal bending. This effect is called stochastic deflection [105, 106]. It was observed experimentally for particles of both signs [19–22]. However, at some penetration depth particles start to "relax" to the channeling mode in skew planes [4] by means of volume capture.

However, by adjusting the crystal orientation one can stimulate the process of channeling or volume reflection in skew a bent crystal plane, providing some benefits w.r.t. the vertical ones. In particular, if one aligns a crystal for volume reflection from one skew crystal plane, a reflected particle will be in optimal conditions to be reflected by the next one, etc. This process is illustrated in Fig. 1.2.4. What is more important, volume reflections in vertical direction will compensate each other, amplifying each other in the horizontal one. This effect is called multiple volume reflection in one bent crystal (MVROC) [24, 107]. It

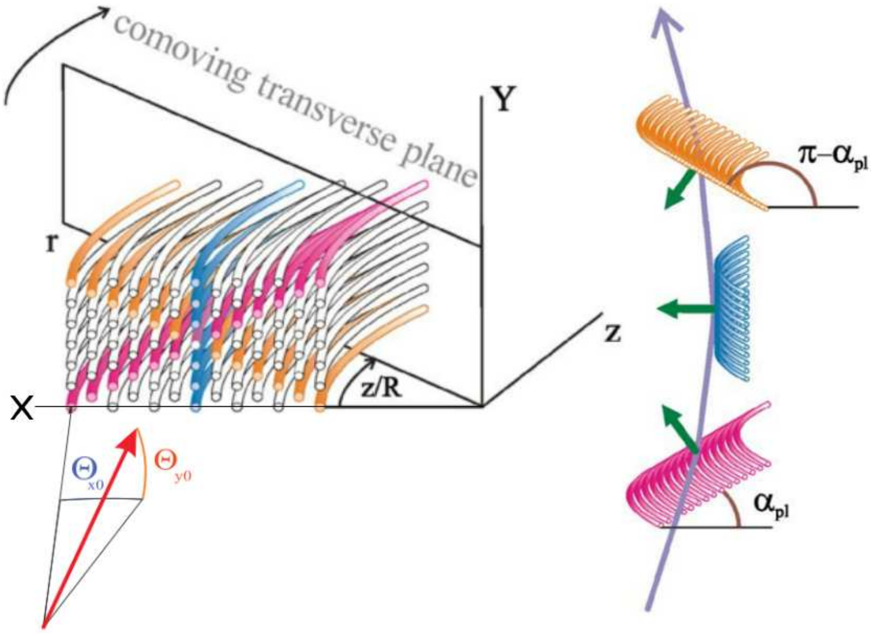

Figure 1.15: Multiple volume reflection in one bent crystal.

was observed experimentally for particles of both signs [23–26,53,54]. Moreover, as it was shown experimentally [51,53,54], MVROC is a very promising source of radiation.

For clear manifestation of MVROC one must align a bent crystal to avoid capture under the channeling conditions. On the other hand one can align skew crystal planes along the beam direction. Consequently, in the case of non-capture in the channeling mode a particle may continue its motion by consequent volume reflections by means of MVROC [A2, A5], which considerably increases the deflection angle of a non-channeling particle.

Therefore, by changing the crystal alignment one can either apply pure axial effects or amplify the planar coherent effects, considered above. Both MVROC and channeling in skew planes will be considered in details below.

1.3 Summary

There are various coherent effects in a bent crystal, applicable for beam steering in modern accelerators. In the planar case it is planar channeling, volume reflection, while the axial one is represented by axial channeling, stochastic reflection, multiple volume reflection in one bent crystal as well as channeling in skew crystal planes. One can calculate a charged particle trajectory by means of solution of equations of motion, containing the transverse electric field, produced by crystal planes or atomic strings, and a centrifugal term due to crystal bending.

Incoherent scattering is responsible for particle escape or capture under the conditions of the coherent effect. For the case of channeling these effects are called dechanneling and rechanneling/volume capture respectively. If a particle escapes the conditions of one coherent effect, it may be deflected by another one, for instance volume reflection after dechanneling.

Incoherent scattering is divided onto Coulomb and nuclear. The first one can be also divided on multiple and single scattering on screened nuclear potential and single electrons. All the processes are defined by the cross sections and can be treated randomly during the trajectory calculations. The realization of this model is the topic of the next chapter.

CHAPTER 2
CRYSTAL SIMULATION CODE

2.1 General description and the algorithm

The CRYSTAL simulation code [A1, A3] is designed to simulate various coherent effects of the interaction of charged particles (protons, electrons, muons and their antiparticles) with straight or curved single crystals taking into account different types of scattering. The developed program has already made it possible to successfully simulate [A3, A6, A7] various experiments to observe and apply coherent effects in crystals on modern accelerators.

The program contains one-dimensional and two-dimensional models that allow one modeling the *classical* trajectories of relativistic and ultrarelativistic charged particles in the field of atomic planes or strings, respectively. The specified ranges of particle energies in CRYSTAL for agreement with an experiment: from 100 MeV and higher. At lower energies, quantum effects can contribute significantly. There is no upper energy limit. The restriction on the angles of incidence of particles w.r.t. the crystalline axes or planes is no more than 4-5 degrees (on modulo). Otherwise, the longitudinal step becomes substantially smaller than the interatomic distance, and the one-dimensional and two-dimensional models become inapplicable.

For the calculation of trajectories and modeling of scattering, the following functions are used: interplanar potential, interplanar electrostatic field, nuclear and electron densities, minimum ionization energy of an atom. All these functions are stored as interpolation coefficients in the input file, which allows one-dimensional and two-dimensional models to be specified for any monocrystal of any orientation without modifying the source code of the program. The interplanar potential and its derivative functions were preliminarily calculated by using the Doyle-Turner potential [78]. The ionization losses are calculated by the model described in Section 1.4.2 in [62]. This calculation is performed taking into account the average density along the entire trajectory after its calculation.

The algorithm for simulation of motion of particles in a crystal is shown in Fig. 2.1. For a one-dimensional model, the trajectory of a charged particle is calculated by numerically solving the equations of motion by the fourth-order

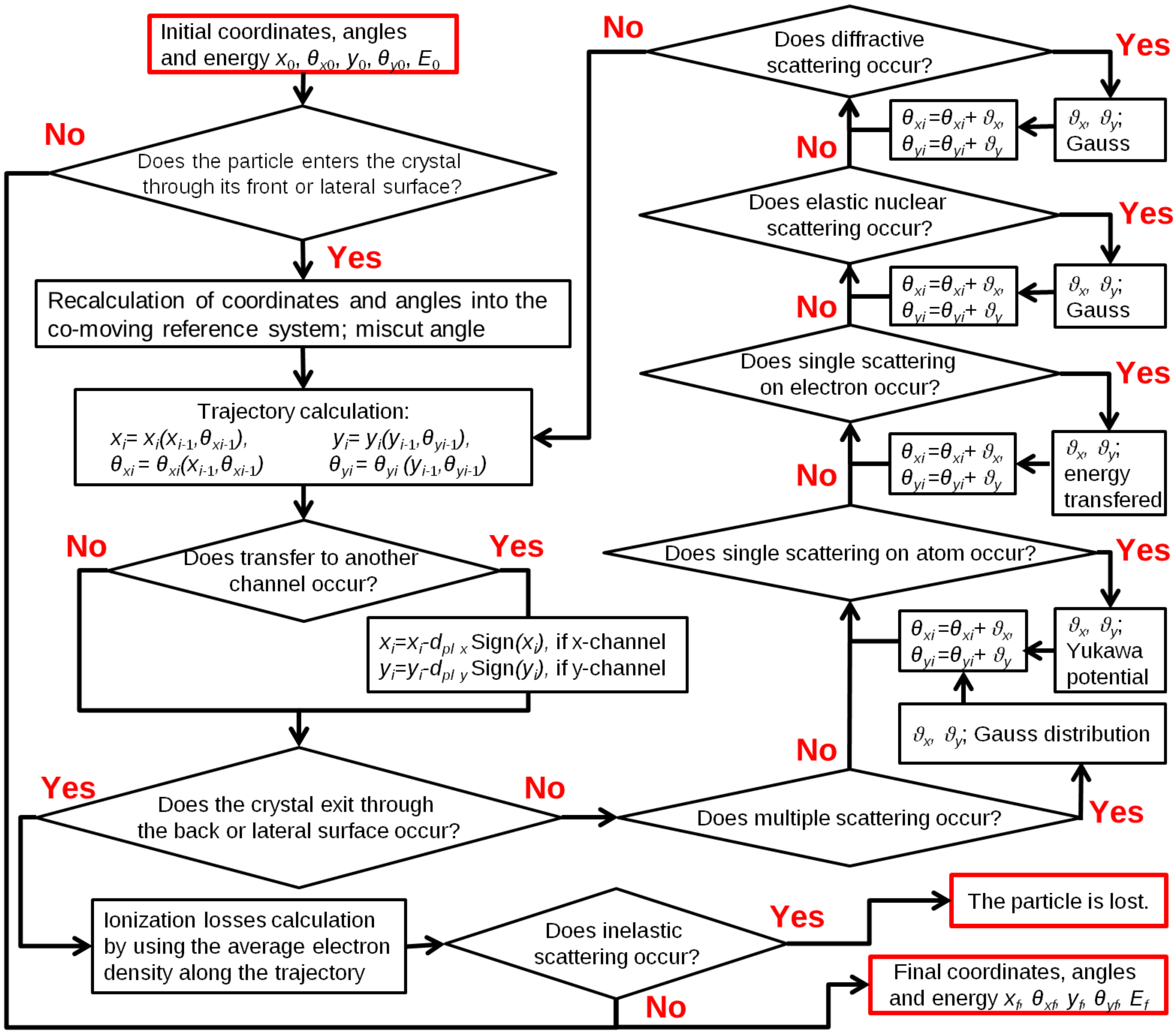

Figure 2.1: The CRYSTAL algorithm.

Runge-Kutta method [108, 109], (1.67) for 1D-model and (1.68) for 2D-model:

$$\begin{cases} \dfrac{d^2x}{dz^2} + \dfrac{U'_{ax\ x}}{pv} + \dfrac{1}{R_x} = 0; \\ \dfrac{d^2y}{dz^2} + \dfrac{U'_{ax\ y}}{pv} + \dfrac{1}{R_y} = 0, \end{cases} \tag{2.1}$$

where R_x and R_y are the bending radius of a crystal in x- and in y-direction, as defined in (1.75).

Coulomb scattering is simulated for all particles by the Monte Carlo method, and for nuclear hadrons, in addition to this, nuclear elastic, diffractive and inelastic scattering is simulated by the model [110]. Coulomb scattering is modeled taking into account the suppression of incoherent scattering [66] by the model [88] and involves multiple and single scattering on atoms with allowance for the screened cross section (for this, the functions of nuclear and electron density are used), and also single scattering of electrons (for this, the minimal energy of ionization is used), as described in the previous chapter. The simulated scattering angles, denoted by ϑ_x, ϑ_y in Fig. 2.1, are added to the angles of the particle, obtained by solving the equation of motion.

The geometry of the crystal is also included in the program, namely the horizontal bending of the crystal, the possibility of entry/exit through its lateral surface, the influence of the miscut angle [111] and [N3], as well as a crystalline cut, which significantly increases channeling efficiency [112, 113]. A special procedure allows one to vary one or more parameters by specifying a table of values for them and performing calculation for each set of parameters. Output files include the values of horizontal and vertical coordinates and particle angles at the entrance and exit of the crystal, as well as the efficiency of channeling, the number of inelastic scattering events, etc.

The program also provides MPI parallelization, which allows one to perform calculations on clusters and supercomputers.

2.2 Interpolation of the main functions and trajectory calculation

The main functions, i.e. interplanar potential, interplanar electrostatic field, nuclear and electron densities and minimum ionization energy of an atom, are not very convenient for fast calculations because of the very large required number of mathematical operations at each step. Therefore, all these functions were interpolated by cubic splines for both 1D- and 2D-model. In particular, in 1D model spline interpolation can be expressed in the following way [108, 109]:

$$S(x) = a_i + \Delta x_i(b_i + \Delta x_i(c_i + d_i\Delta x_i)), \tag{2.2}$$

where i is the interpolation node number, $\Delta x_i = x - x_i$, x_i interpolation nodes, a_i, b_i, c_i and d_i the interpolation coefficients.

For the 2 dimensional case it will be written as

$$\begin{aligned} S(x,y) = g_{i+1,j,2}(y)\frac{\Delta x_i^3}{6hx_i} - g_{i,j,2}(y)\frac{\Delta x_{i+1}^3}{6hx_i} + \\ (g_{i+1,j,1}(y) - \frac{g_{i+1,j,2}(y)}{6}hx_i^2)\frac{\Delta x_i}{hx_i} - (g_{i,j,1}(y) - \frac{g_{i,j,2}(y)}{6}hx_i^2)\frac{\Delta x_{i+1}}{hx_i}, \end{aligned} \tag{2.3}$$

where

$$g_{i,j,k}(y) = C_{i,j+1,k}\frac{\Delta y_j^3}{hy_j} - C_{i,j,k}\frac{\Delta y_{j+1}^3}{hy_j} + B_{i,j,k}\frac{\Delta y_j}{hy_j} - A_{i,j,k}\frac{\Delta y_{j+1}}{hy_j}, \tag{2.4}$$

$\Delta x_i = x - x_i$, $\Delta y_i = y - y_i$, x_i and y_i the interpolation nodes, $A_{i,j,k}$, $B_{i,j,k}$, $C_{i,j,k}$ the interpolation coefficients.

All the interpolation coefficients are calculated in advance by using formulae (1.17-1.18,1.49-1.52) from the first chapter. The summation for multiple planes or axes is calculated according to (1.2,1.4). For the case of a particle entrance or exit through a crystal lateral surface an additional set of interpolation coefficients is calculated, corresponding to the main functions near the crystal boundary. In this case the sum for (1.2,1.4) on i starts from 0.

All the main functions are reproduced during the simulation process by spline interpolation (2.2-2.4). The electric field is used for instance for a numerical solution of equations of motion (2.1), being found at each step by the fourth-order Runge-Kutta method.

The choice of the simulation step follows from its evaluation in the transverse direction. It should be no more than d_{pl}/N_{steps}, where N_{steps} is the number of transverse steps necessary for the particle to pass from one edge of the channel to the other in channeling mode with the maximum possible amplitude. Consequently, the value of simulation step in the longitudinal direction is determined by the formula:

$$dz = \pi d_{pl} \sqrt{\frac{2pv}{U_0}} / N_{steps}. \tag{2.5}$$

For simplicity, in the algorithm, dz was not changed when the particle moved under the channeling conditions. Only in the case of a particle escape from the latter, dz was changed, namely decreased in inversely proportion to the angle of the particle w.r.t. the crystal plane. In order to achieve high accuracy, N_{steps} is usually taken to be equal to 500.

2.3 Scattering routine

Coulomb scattering involves multiple scattering, described by a Gaussian distribution, and single scattering characterizing the long non-Gaussian tails of the distribution of scattering angles as was decribed in the previous chapter. To simulate multiple scattering, it is sufficient to calculate its r.m.s. angle $< \vartheta^2_{Cms} >$ (1.44). It is calculated by integrating over the scattering angles $\vartheta \leqslant \vartheta_2$ of Eq. (1.36), taking into account the suppression of scattering.

ϑ_2 splits multiple and single scattering [88]. The choice of this angle is not strictly defined, since at its zero value only single scattering is actually left. However, for small angles such scattering events can be taken into account in multiple scattering, which considerably reduces the number of necessary computations. One can calculate the probability of a single scattering by using the single scattering cross section σ_{Css} (1.43), giving:

$$P_{Css} = \sigma_{Css} n_{Npl/ax} dz = 4\pi n_{Npl/ax} dz \left(\frac{zZe^2}{pv}\right)^2 \left(\frac{1}{\vartheta_1^2 + \vartheta_2^2} - \frac{1}{\vartheta_1^2 + \vartheta_{max}^2}\right), \quad (2.6)$$

where $n_{Npl/ax}$ represents either planar or axial nuclear density depending on the model choosen for simulations (1D or 2D). One can distinguish between single and multiple scattering by taking Pss in the range from 0 to 1. For convenience of modeling, the value 0.1 was used. The angle ϑ_2 is expressed from (2.6). At too low values of the nuclear density, P_{Css} can be less than the set value for any ϑ_2, in which case multiple scattering at the current step is not modeled.

The generation of the multiple scattering angle by means of the Gaussian distribution can be done by Monte Carlo as:

$$\vartheta = \sqrt{- < \vartheta_{Cms}^2 > \ln(1-\xi)}, \quad (2.7)$$

where ξ is a uniform random number, generated in the interval [0,1). In order to generate the x- and the y-components of the multiple scattering angle one has to generate another random number ξ, namely:

$$\begin{cases} \vartheta_x = \vartheta \cos(2\pi\xi); \\ \vartheta_y = \vartheta \sin(2\pi\xi). \end{cases} \quad (2.8)$$

Coulomb single scattering is simulated by means of the distribution (1.36) by using one more random number ξ, with the value of the minimum angle taken to be ϑ_2, and the maximum angle ϑ_{max}, determined by the size of the atomic nucleus. The the x- and the y-components of the single scattering angle can be generated according to (2.8). In addition, single scattering on electrons is simulated. For this, the Fermi energy is estimated in dependence on the particle coordinates in a crystal. The energy is assumed to be the minimum energy transferred to an electron. The simplest and at the same time ruther realistic way to estimate the Fermi energy is to calculate the average logarithm of the interplanar or interaxial potential [70], averaged over the electron density. Then one can generate the transfered energy by using the cross section (1.46) and another specially generated random number ξ, and in a such way calculate the scattering angle. The further procedure is analogous to the procedure for simulating single scattering on an atom.

Nuclear scattering of hadrons is simulated on the basis of the model [110]. Nuclear scattering includes elastic scattering (on the whole nucleus), diffractive (on one nucleon) and inelastic (leading to the absorption of a particle). The r.m.s. scattering angles can be written as:

$$< \vartheta_N^2 >= \frac{1}{Bp^2}, \tag{2.9}$$

where B is a slope determined for each type of scattering. For example, for protons in the case of elastic scattering, it is written as:

$$B = 12.85 A^{2/3} GeV^{-2}, \tag{2.10}$$

where A is the atomic number of a nucleus of crystal substance. The scattering angles are simulated by Gaussian distribution according to equations (2.7-2.8).

A single scattering event can be generated by Monte Carlo simulation of the scattering length of a particle by using another specially generated random number ξ:

$$z_{sc} = -\frac{\ln(1-\xi)}{L_{sc}}, \tag{2.11}$$

where L_{sc} can be equal to the values of L_{Css}, L_{Ce}, L_{el}, L_{diff} or L_{inel}, depending on the type of single scattering considered (single Coulomb on atoms (1.44), on single electrons (1.48), nuclear elastic, diffractive or inelastic (1.44) respectively). In order for the scattering to take place, the z_{sc} should not exceed the modeling step dz. Since it is convenient to simulate the inelastic scattering in the end of the crystal, one must compare z_{sc} with the trajectory length for this case.

2.4 Structure of program files

The program contains the following **program files**:

- **Crystal51_MPI.f** is the control program, which contains MPI procedures, namely parallelizing, parameter variation, saving output files to separate directories and initializing the random number generator and starting the Single procedure.
- **Single.f** is a procedure that organizes input-output, generation of the input particle beam and starts the simulation procedure for the trajectory in the crystal for each particle separately. When running calculations on a multi-core or multiprocessor machine, the total number of particles is evenly distributed among all the processes.
- **crystal_sytov51ph21.f** is a procedure for modeling the trajectory of a charged particle in a crystal, including an initializing procedure that organizes the input parameters of the crystal and particle beam and calculates the quantities needed for the program, and auxiliary procedures and functions such as one- and two-dimensional spline interpolation.

- **rnd.f** is the random number generator RANMAR [30].
- **Makefile** is a file containing the commands for compiling and running the program.

The program includes the following **input files**:

- **crystal-parameters.dat** is a file containing parameters for the geometry of the crystal and the input beam.
- **Impact.dat** is a file containing beam particle distributions along the horizontal and vertical coordinates and angles, as well as the distribution type.
- **si.dat** is file containing the main parameters of the crystal material and the length of the nuclear scattering of particles, by default it is silicon. For convenience, the program allows one to use files with the name of other elements - germanium and tungsten, in which case the files should be named **ge.dat** and **w.dat**.
- **plane-si-110.dat** is a file containing the basic parameters and interpolation coefficients of the basic functions for the (110) plane. For convenience, there is a possibility of using similar names for other planes (111) and (100) (in the title instead of "110", respectively, "111" or "100") and other materials ("ge" and "w" instead of "si", by analogy with si.dat). For the axial case, the file name specifies "axis" instead of "plane". For example, for a silicon crystal, aligned in the direction of the <111> axes, the file will be called: **axis-si-111.dat**. The potentials and derived functions, calculated by different models can be implemented into these files, though the default model is the Doyle-Terner potential [78]. To successfully launch the program, all listed files must be in the same directory. To avoid errors, the full path to the directory and the name of the catalog itself should be written in the standard Latin alphabet.

2.5 Geometry of a crystal and generation of a charged particle beam

The geometry of a crystal and the parameters of the incident beam are completely specified in the input files crystal, namely **crystal-parameters.dat** and **Impact.dat**. All the values for coordinates and lengths are written in cm as well as for angles in radians. The feature of variation of parameters is developed for parameters from the first files. For this the parameter table must be written in separate input files line by line. The structure of the **crystal-parameters.dat** file (the names of parameters are marked by italic bold) and the name of the **files for data variation** (in brackets) is the following:

- Name of the directory in which the output will be stored (**PROGRAM.dat**)
- Number of particles in the input beam for modeling (**NMC.dat**)
- The energy of the particles in GeV (**ENERGY.dat**)
- Program mode (**MODE.dat**):
  - ***MOD*** (symbols 1-3 or 4-6 in the word) is a modified Monte Carlo method, in which particles are assigned a weight equal to 1, which decreases as a function of the inelastic scattering probability in the crystal, which makes it possible to calculate the fraction of inelastically lost particles with greater accuracy. If this mode is not selected, then in the case of inelastic scattering the particle is considered to be lost.
  - ***INP*** (symbols 1-3) is the mode of reading the input beam parameters from files fort.42001, fort.42002, etc. by the number of processes to be launched in the format horizontal coordinate and angle, vertical coordinate and angle (coordinates in cm, angles in radians). Otherwise, the beam is generated by Monte Carlo.
  - ***TR*** (symbols 4-5) is the mode of recording the particle trajectory in the output file Trajectory.dat in the format: longitudinal coordinate, transverse horizontal coordinate, horizontal angle (coordinates in cm, angles in radians). If none of the listed modes is selected, it is enough to write NO.
- Particle names: ***proton***, ***antiproton***, ***electron***, ***positron***, ***muon+***, ***muon-*** (**PARTICLE.dat**)
- Material of the crystal: ***si*** for silicon, ***ge*** for germanium, ***w*** for tungsten. This determines the choice of the file **si.dat** and **plane-...** or **axes-...** (see above) (**MATERIAL.dat**)
- Type of planes or axes; planes are indicated as (number), for example: ***(110)***. Similarly, the axes are specified, but with dashes instead of brackets, ***-111-*** instead of (111). (**PLANE.dat**))
- The width of the crystal (**THICKNESS.dat**)
- The crystal height (**HEIGHT.dat**)
- The length of the crystal (**LENGTH.dat**)
- The angle of bending of the crystal (can be negative if the crystal is bent on the left but not on the right) (**BENDING.dat**)
- The horizontal coordinate of the crystal (if = 0, the beam falls to the center of the crystal) (**COORDX.dat**)

- The vertical coordinate of the crystal (if = 0, the beam falls to the center of the crystal) (**COORDY.dat**)
- The average horizontal angle of beam incidence on the crystal (**BEAMX.dat**)
- The average vertical angle of beam incidence on the crystal (**BEAMY.dat**)
- The horizontal angular orientation of the crystal (**ANGLEX.dat**)
- The vertical angular orientation of the crystal (**NGLEY.dat**)
- The value of the miscut angle (**MISCUT.dat**)
- The angular divergence of the beam by default (**DELTATETA.dat**)
- The crystal mode with the crystalline cut [20-21]; cut when selecting it, otherwise no-cut (**CUT.dat**)
- The first longitudinal coordinate of the cut (**CUTZ1.dat**)
- The second longitudinal coordinate of the cut (**CUTZ2.dat**)

Input files, containing initial parameter tables can be generated automatically by using the entry in the crystal-parameters.dat file instead of the parameter value: ***R <space> min. value of parameter <space> max. value of parameter <space> step***. This function is enabled for all numeric parameters in **crystal-parameters.dat**. If one varies several parameters, the program will perform calculations for each combination of their values. If it is necessary to go through parameter values in groups, then instead of ***R***, one needs to write ***R1*** for each parameter, related to the group. The number of values for each parameter in the group must match. When specifying such values manually in the corresponding files with tables of initial parameters, ***R1*** should be written in the first line.

The structure of the **Impact.dat** file is the following:

- ***center of distribution of horizontal coordinates of the input beam <space> width of distribution (see below) <space> type of distribution***
- ***center of distribution of vertical coordinates of the input beam <space> width of distribution <space> type of distribution***
- ***center of distribution of horizontal angles of the input beam <space> half-width of distribution (see below) <space> type of distribution***
- ***center for distribution of vertical angles of the input beam <space> half-width of distribution <space> type of distribution***

The distribution type is either uniform or Gaussian: in the file, respectively, ***Uniform*** or ***Gauss***. For a Gaussian distribution, the root-mean-square value is introduced instead of the width or half-width. To include the default values, one needs to add the word ***no*** to the beginning of the corresponding line in the Impact.dat file. The default distribution is Gaussian.

2.6 Output Files

The output files are written to the directory whose name is written in the first line of the **crystal-parameters.dat** file. Also the nested directories are created inside a given directory in the case of using the function of variation of the parameter values. The name of the nested directories correspond to the current value of the parameter being variated. The level number of nested directories is equal to the number of variated parameters.

In the created directory, the output coordinates and angles of particles are recorded after passage through the crystal:

- **x.dat** is the horizontal coordinate;
- **tx.dat** is the horizontal angle;
- **y.dat** is the vertical coordinate;
- **ty.dat** is the horizontal angle.

Similar files are created in the **Nincr01** sub-directory for input coordinates and angles at the crystal entrance. The efficiency values are written to the Eff.dat file, namely channeling efficiency; the fraction of inelastic particle losses; the absolute error of this fraction; its relative error. Also, the input files **crystal-parameters.dat** and **Impact.dat** are copied.

2.7 Implementation of MPI Parallelization

Since in the program the trajectory of each particle is simulated independently, the process of parallelization by using the Message Passing Interface (MPI) is rather simple. With the help of a special function, each process receives equal parts of the particles for simulation. To do this, one only needs to know the number of processes involved and the number of the current process that can be received by using the procedures MPI_COMM_SIZE and MPI_COMM_RANK respectively.

The uniqueness of each particle is ensured by the individual initialization for each process of the random number generator, in which the process number is the argument. Since MPI is designed for distributed memory systems, all the input data (interpolation coefficients of the main functions, etc.) are loaded into the RAM separately for each process. In particular the first process reads all the input data and then broadcasts these data to the other processes by using the MPI_BCAST procedure.

The main limitation of linear growth is the amount of computation. However, since it is done only once at the start of the program run, it doesn't contribute considerably, if the amount of calculations is large enough to achieve optimal computing performance. Moreover, since simulations do not practically require interactions between different processes, the productivity indeed increases almost linearly with the increase of their number. Data exchange is performed only at the end of the calculations by using the MPI_Reduce procedure, which calculates the channeling efficiency, the fraction of inelastic losses, and other data that are written to the Eff.dat file. Since it concerns only few numbers, this practically has no effect on performance.

2.8 System requirements, program compilation and launch

The CRYSTAL simulation code is written in Fortran language and does not require any libraries other than MPI. The program is debugged to run under the Linux operating system with the installed compilers gfortran (GNU Fortran) or ifort (Intel Fortran) and mpif77 or mpif90 (either OpenMPI or IntelMPI). Compilation and startup is performed using: ./Makefile. The number of processes to run is specified in the Makefile: mpirun -np number of processes. To achieve the optimal counting speed, it must correspond to the number of logical cores. The amount of required RAM does not exceed 400 MB per process. The program can also be used under the Windows operating system, for example when PGIFortran and OpenMPI are installed.

The program was also debugged and run on CINECA supercomputers (Bologna, Italy), Fermi, Galileo and Marconi. The maximal number of cores, used simutaneously was 2304 on CPUs Intel Xeon E5-2697 v4 (Broadwell) at 2.30 GHz at Marconi-A1. The program, compiled with Intel compiler, was nearly twice faster than with the GNU one on both Marconi and Galileo.

2.9 Summary

The CRYSTAL simulation code is developed, allowing one simulations of various coherent effects of charged particles interaction with straight and curved crystals. The program includes one-dimensional and two-dimensional models, providing the possibility to calculate particle trajectories in the averaged field of atomic planes and strings, respectively. The program uses Doyle-Turner model of atomic potential, though any potential can be implemented without code modifications. In addition incoherent Coulomb scattering is simulated, as well as various types of nuclear scattering - elastic, diffractive and inelastic.

For the optimization problem solution, the program includes a procedure for varying the initial parameters, in which the code is able to perform a complete simulation cycle for each combination of parameters. To increase computing performance, MPI is implemented in the program for high-performance computing on supercomputers and clusters. Parallelization can be done due to the independent calculations of different particle trajectories. As a result each process carries out simulation for its set of particles.

The main advantage of the CRYSTAL program lies in *ab-initio* simulations of previously undefined effects. Therefore the CRYSTAL simulation code allows one to predict new, previously unknown effects.

CHAPTER 3

NEW METHODS OF BEAM DEFLECTION AND OPTIMIZATION

Crystalline collimators can potentially considerably improve the cleaning performance of the presently used collimator systems using amorphous collimators. A crystal-based collimation scheme which relies on the channeling particle deflection in bent crystals has been proposed and extensively studied both theoretically and experimentally. However, since the efficiency of particle capture into the channeling regime does not exceed ninety percent, this collimation scheme partly suffers from the same leakage problems as the schemes using amorphous collimators.

To improve further the cleaning efficiency of the crystal-based collimation system to meet the requirements of the Future Circular Collider, a *double* crystal-based collimation scheme is suggested, to which the second crystal is introduced to enhance the deflection of the particles escaping the capture to the channeling regime in its first crystal. The application of the effect of *multiple volume reflection in one bent crystal* and of the same *in a sequence of crystals* is simulated and compared for different crystal numbers and materials at the energy of 50 TeV. To optimize these effects, the analytical model of single and multiple volume reflection in one and a sequence of bent crystals is suggested. Being invariant w.r.t. the particle energy this model is applicable for any high-energy accelerator.

To enhance also the efficiency of use of the first crystal of the suggested double crystal-based scheme, it is proposed to apply the following: the method of increase of the probability of particle capture into the channeling regime at the first crystal passage by means of fabrication of a *crystal cut* and the method of the amplification of non-channeled particle deflection through the multiple volume reflection in one bent crystal, accompanying the particle *channeling by a skew plane*. Both of these methods are simulated for the 50 TeV FCC energy.

3.1 A possible setup of a crystal-based collimation scheme at the FCC

The collimation system is of key importance for stable operation of modern high energy storage rings and colliders, for instance for the LHC and the future HL-LHC project [114, 115]. Moreover, ”the operation and physics goals of re-

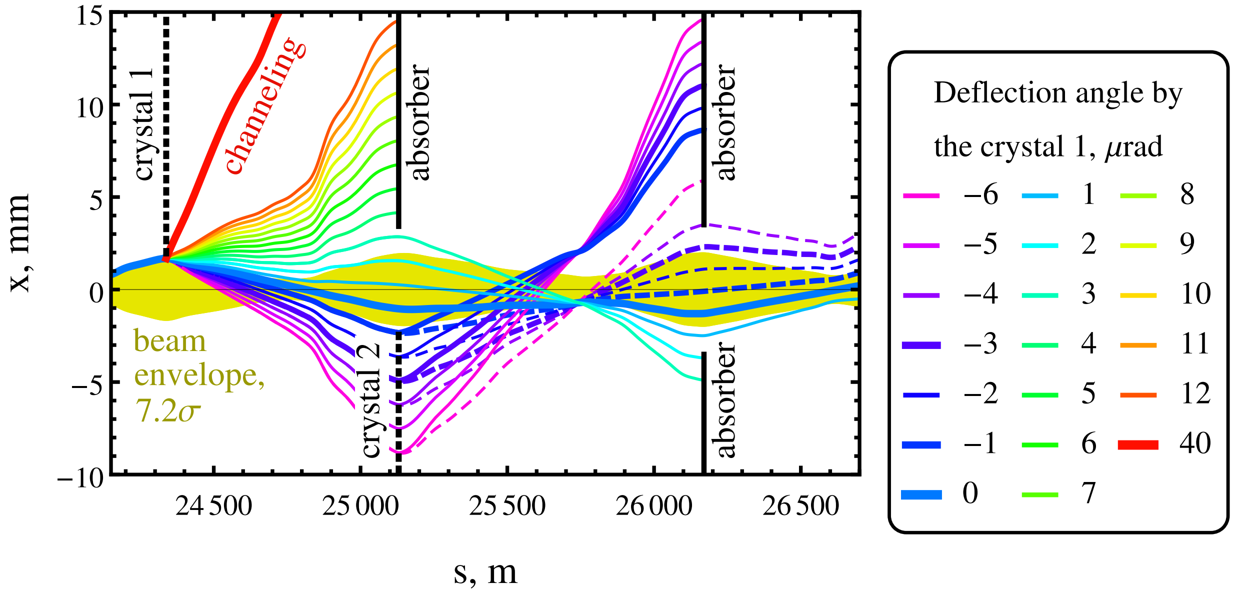

Figure 3.1: Double crystal-based collimation system. Beam trajectories for different deflection angles by the crystal 1 are simulated in the betatron cleaning area of the FCC [119], taking into account only betatron oscillations. The crystal 1, crystal 2 and the absorbers are placed at 7.2 σ, 9 σ and 12.6 σ respectively. The particles, passed through the crystal 2, are assumed to be deflected by -5 μrad for solid lines and 0 μrad for the dashed ones. Bold curves illustrate the trajectories of non-deflected particle, of channeled particles and particles deflected by 1 and 3 μrad, being the typical angles of particle deflection by volume reflection (VR) and multiple volume reflection in one bent crystal (MVROC) respectively.

cent superconducting, high-energy hadron colliders, such as the Tevatron, the Relativistic Heavy-Ion Collider (RHIC), and the Large Hadron Collider (LHC), could not be fulfilled without adequate beam collimation" [116]. The small-angle scattering in collimators is used to induce a steady betatron amplitude growth resulting in particle collisions with the target collimators (absorbers) before they reach the apertures of superconducting magnets. Thick amorphous collimators are used at the LHC, RHIC and SPS at present. The efficiency of any collimation scheme is limited by the leakage to sensitive equipment. Since the uncorrelated Coulomb scattering in the amorphous collimators is characterized by the small average scattering angles, the leakage of the collimation schemes with amorphous collimators is determined by both the multiple particle passages through the latter and the small impact parameters of particle collisions with the target collimators (absorbers).

Crystal collimators can be used to decrease the leakage of the present collimation systems [116, 117]. The point is that a bent crystal can deflect channeling particles by the angles large enough to hit target collimators immediately and with a large impact parameter. Such a collimator scheme, using planar channeling in bent crystals, proposed in [118], has been widely explored in experiments [38–49].

However, this collimation approach also suffers from the leakage. The latter is mainly induced by more than ten percent of the particles inevitably escaping the capture to the channeling regime at their first passage through the crystal collimator. As with the amorphous collimators, many of these particles reach target collimators by means of volume reflection or Coulomb scattering only after a number of passages through the crystal collimator having small impact parameters. That is why further possibilities to improve the efficiency of the crystal assisted collimation system still remains.

Therefore, a new *double* crystal-based collimation system is suggested, as shown in Fig. 3.1. This layout represents the FCC betatron cleaning insertion with beta-functions and absorber transverse positions (12.6 σ) taken from [119]. In the trajectories simulated only betatron oscillations were taken into account, while the synchrotron ones were neglected because of too low values of the dispersion functions.

The bent crystal 1 is placed at 7.2 σ, i.e. at the transverse position of primary collimators [119], deflecting most of particles into the absorber in the channeling mode. The second crystal, placed at $\sim$ 9 σ, plays role of the secondary collimator intercepting particles, volume reflected in the crystal 1, and deflecting them into the absorber.

The collimation system proposed [A5] demonstrates the following advantages.

1) The impact parameters of particles at the absorbers are large enough to prevent the leakage at the absorber boundary.

2) Close to 100 % of halo particles will be intercepted by only one passage through the betatron cleaning insertion.

Different coherent effects, being promising for this application in both bent crystals, are proposed. In particular, for the second crystal we suggest the several-fold increase of the typical angle of scattering and volume reflection in the crystal collimator by the effect of multiple volume reflection in one bent crystal (MVROC) [24, 107]. A good alternative to MVROC can be volume reflection in a sequence of crystals [120]. The main advantage of both effects is large angular acceptance to deflect coherently almost all the particles passing through the crystal and large enough deflection angle θ_{Xdef} to deflect the particles into the absorber by few or even only one crystal passage.

To amplify the deflection angle even more, it is proposed to use the advantages of both of these effects by using of MVROC in a sequence of crystals. Moreover MVROC in crystals of different materials is studied: silicon,

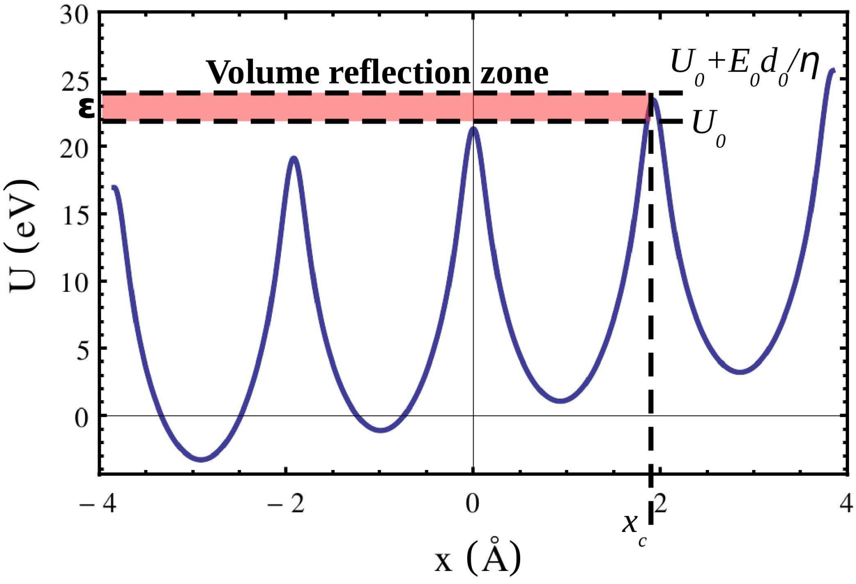

Figure 3.2: Interplanar potential in (110) Si crystal.

germanium and tungsten. The parameters of the crystal as well as its alignment for each effect are optimized both theoretically and by means of Monte Carlo simulations on example of 50 TeV protons of Future Circular Collider (FCC) [121–124]. These effects are compared by the peak deflection angle.

The second approach is the application of planar channeling in skew crystal planes [A2, A5] instead of the vertical ones. Its main advantage is deflection of non-channeled particles by means of MVROC instead of volume reflection considerably amplifying the deflection angle. The angular acceptance and, consequently, the channeling efficiency also increases. In addition, it is suggested to considerably increase the channeling efficiency by application of the crystal cut [112, 113].

Combination of these two approaches can lead to the further collimation optimization. Each of suggested coherent effects has a potential to considerably increase the efficiency of the crystal-based collimation system.

3.2 Volume reflection in a sequence of bent crystals

Volume reflection at optimal conditions provides a deflection angle α of approximately $\alpha \approx 1.5\theta_L$ [99]. More exact calculations of the ratio of the volume reflection angle to the Lindhard angle (for straight crystal) can be provided by formula from [99, 100] and rewritten, taking into account the critical radius R_{cr}:

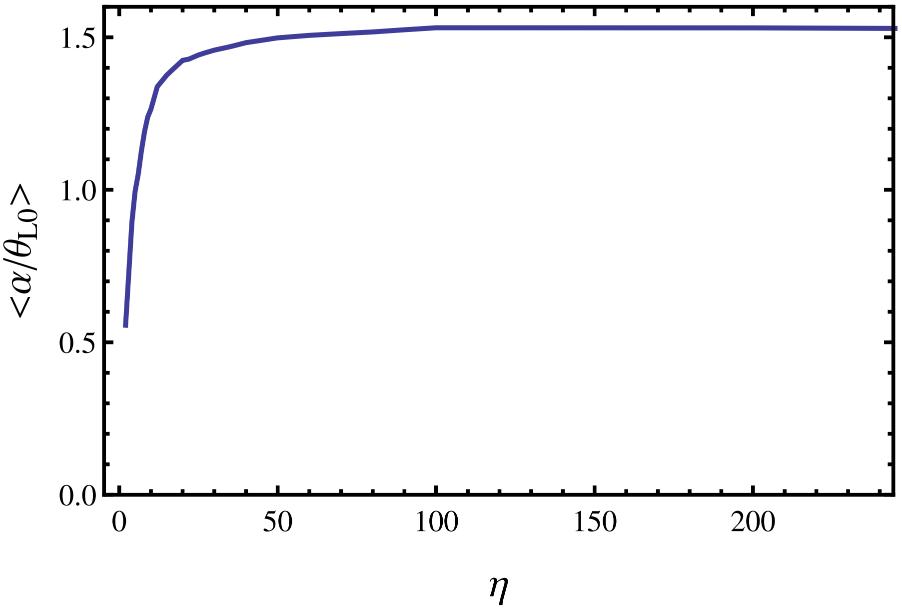

Figure 3.3: The dependence of the ratio of volume reflection angle to the Lindhard angle on the ratio of the bending radius to its critical value.

$$\frac{\alpha}{\theta_L} = \frac{E_0}{\eta\sqrt{U_0}} \int\limits_{x_0}^{x_c(\epsilon)} \left[\frac{1}{\sqrt{\epsilon - U(x) - \frac{E_0}{\eta}x}} - \frac{1}{\sqrt{\epsilon - U(x_{ref}(\epsilon)) - \frac{E_0}{\eta}x}} \right] dx. \qquad (3.1)$$

Here η is the ratio of the bending radius R to its critical value R_{cr}, $U(x)$ hereinafter will be the interplanar potential function of a straight crystal instead of $U_{pl}(x)$ (since the axial potential will not be used for theoretical calculations anymore and there is no need to differ it from the interplanar one), $\frac{E_0}{\eta}x$ represents centrifugal fraction of interplanar potential, ϵ is the transverse energy, x_0 is the initial coordinate of particle motion and x_{ref} is the volume reflection point (see Fig. 3.2). The dependence on transverse energy can be reduced by its averaging on over-barrier values, the distribution of which can be approximately considered as uniform [99, 100]:

$$< \frac{\alpha}{\theta_L} >= \frac{\eta}{E_0 d_0} \int\limits_{U_0}^{U_0+\frac{E_0}{\eta}d_0} \frac{\alpha}{\theta_L} d\epsilon, \qquad (3.2)$$

where d_0 is the interplanar distance. It should be noted that multiple scattering have not been considered yet, because the goal is to estimate optimal parameters for Monte Carlo simulations.

Thus, the obtained formulae (3.1-3.2) [A5, A7] depend only on interplanar potential and bending radius. They are very useful, because they do not depend

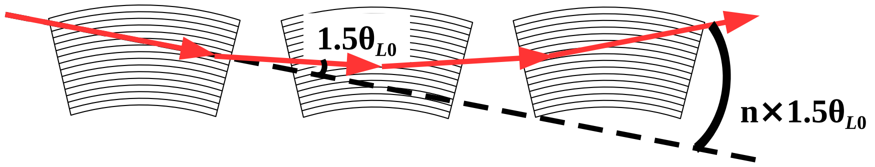

Figure 3.4: Volume reflection in a sequence of bent crystals.

on particle energy and therefore, can be verified with experiments already done as well as can be applied at higher energy.

A plot representing the dependence by Eqs. (3.1-3.2) for (110) planes is shown in Fig. 3.3. Indeed, the maximal deflection angle of $1.53\theta_L$ is reached at the bending radius

$$R \approx 100 R_{cr}. \tag{3.3}$$

However, in reality $R = l_{cr}/\varphi$ is limited by the bending angle φ, to be at least several times higher than θ_L, and by the crystal length l_{cr}, always limited by experimental reasons. These constraints are especially important when considering volume reflections in a sequence of bent crystals (see Fig. 3.4).

All of the crystals in a sequence as well as their orientation are considered to be the same. Therefore, the sum of deflection angles at each crystal from Eq. (3.2) should be less than the bending angle. Moreover, to avoid the capture into the channeling mode, the angle of alignment of any crystal in a sequence should be at least on $1.5\theta_L$ less than the current beam direction. This can be transformed into the condition:

$$n < \frac{\alpha}{\theta_L} > (\eta) = \varphi - 3\theta_L, \tag{3.4}$$

where n is a number of bent crystals in a sequence, volume reflection angle is fixed w.r.t. the interplanar potential. We fix also the total length of the sequence L_{seq}, because, for instance, the crystal-based collimation is optimized taking into account constraints on inelastic nuclear scattering rate that depends on the total length of the crystal crossed by the beam [94]. Therefore the bending angle can be calculated by the equation:

$$\varphi = L_{seq}/n\eta R_{cr}, \tag{3.5}$$

transforming the condition (3.4) into:

$$n < \frac{\alpha}{\theta_L} > (\eta) = L_{seq}/n\eta R_{cr} - 3\theta_L, \tag{3.6}$$

and expressing η, one can find an optimal bending radius as a function of n. Unfortunately, Eq. (3.6) is not linear, but can be simply solved numerically.

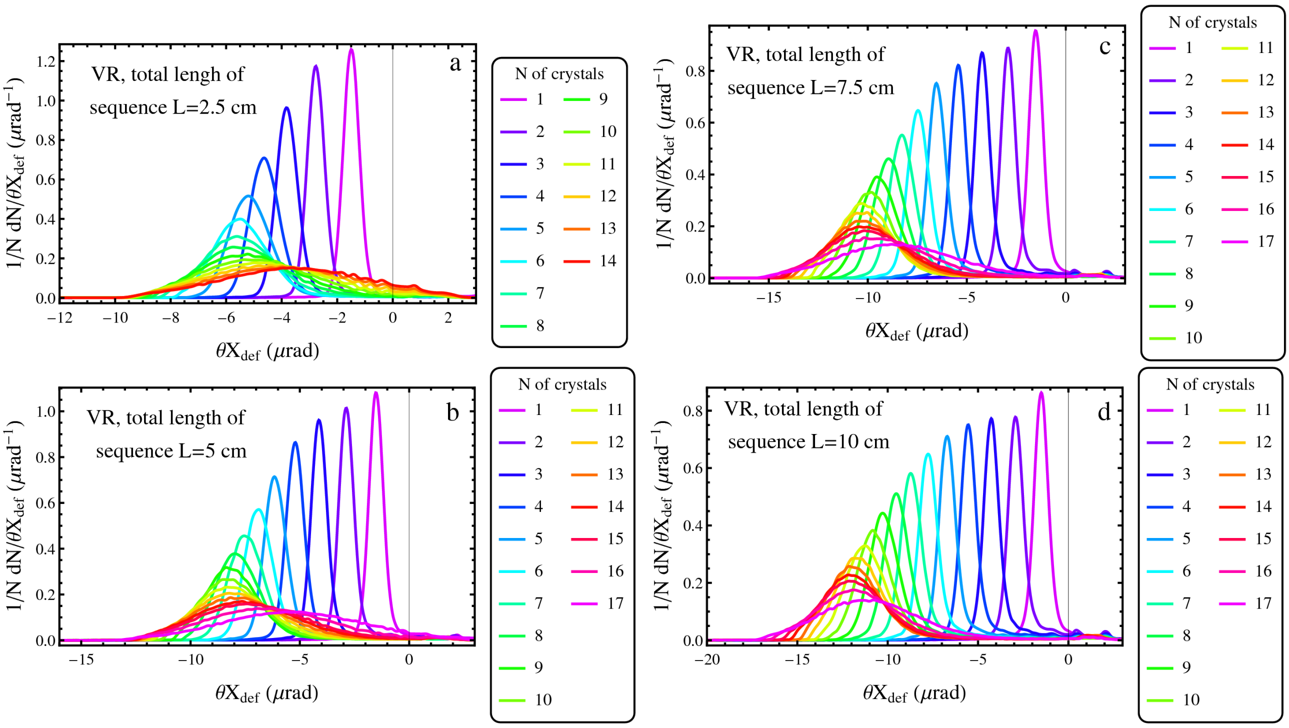

Figure 3.5: Angular distribution behind the crystal for volume reflection of 50 TeV protons in a sequence of (110) bent silicon crystals. Bending radius is calculated according to (3.6).

This equation was applied to calculate the optimal parameters of a sequence of silicon crystals for different length values: 2.5 cm, 5 cm, 7.5 cm and 10 cm and for different number of crystals. These parameters were used for Monte Carlo simulations with application of the CRYSTAL simulation code [A1, A3]. The simulation results for 50 TeV protons deflection with a statistics of 200000 particles are shown in Fig. 3.5. Hereinafter the initial angular divergence is taken at 0.23 μrad which is 4 times lower than θ_L at 50 TeV and more than an order lower than the angular acceptance of volume reflection and MVROC.

The results confirmed the existence of the optimal number of crystals depending on the sequence length. If the number of crystals is too low, the deflection angle is also low. However, for too high crystal number the peak deflection angle decreases, and the divergence of the deflected beam becomes too wide. This is mainly explained by a sharp decrease of deflection angle for small R (see Fig. 3.3) and by increase of over-barrier transverse energy range (see Eq. (3.2) and Fig. 3.2), spreading deflection angles stronger.

Both the peak deflection angle and the optimal number of crystals increases with the rise of L_{seq}. At L_{seq} =10 cm the peak deflection angle achieves 12 μrad for 14 crystals in a sequence. However, depending on the experimental set up one can reduce the number of the crystals to decrease the spread of deflected beam.

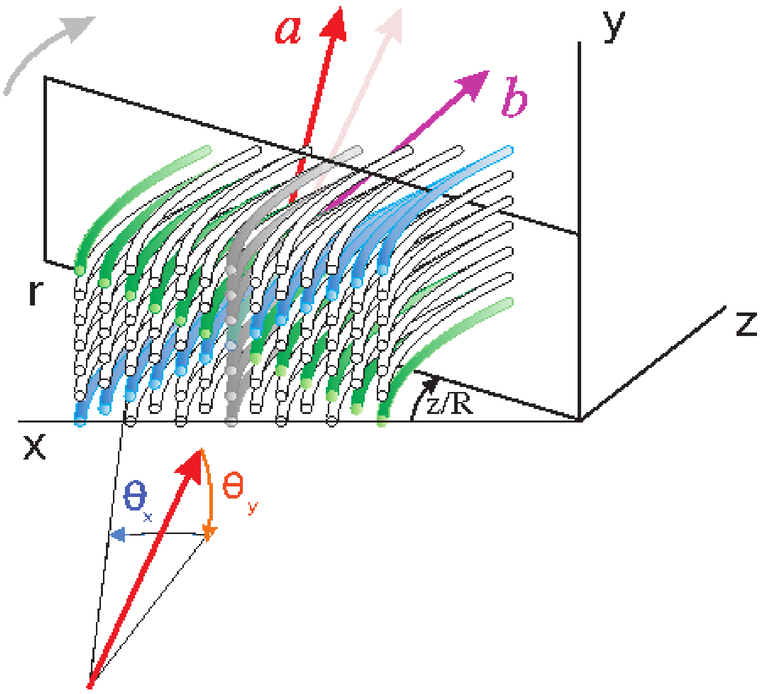

Figure 3.6: Multiple volume reflection in one bent crystal.

3.3 Multiple volume reflection in one and in a sequence of bent crystals

In order to obtain the deflection on a higher angle one can apply the electric field of atomic strings, being several times stronger than that of planes.

One of the coherent effects, exploiting axial electric fields, is the multiple volume reflection in one bent crystal. For <111> silicon crystal axes MVROC deflection angle for protons is 5 times higher than the volume reflection one [24, 107], which was confirmed experimentally [23, 25, 26]. The idea of multiple volume reflection in one bent crystal is volume reflections from skew crystal planes as shown in Fig. 3.6. While in vertical direction these reflections almost compensate each other in the horizontal one they will be summarized.

Indeed, reflections from skew planes result in deflection by the angles $\theta_X = -\theta_R \sin\alpha_{pl}$ and $\theta_Y = \theta_R \cos\alpha_{pl}$ in the horizontal and vertical coordinate planes, respectively. α_{pl} is the inclination angle of skew plane, θ_R the reflection angle by a plane bent with the radius $R/\sin\alpha_{pl}$.

Since $\sin\alpha_{pl} > 0$ for any $0 < \alpha_{pl} < \pi$, all the horizontal deflection angles θ_X will be summarized. On the contrary, since $\cos(\pi - \alpha_{pl}) = -\cos\alpha_{pl}$, the vertical reflections from symmetric skew planes with inclination angles α_{pl} and $\pi - \alpha_{pl}$ compensate each other.

The optimal conditions of MVROC [A5] are mainly defined by horizontal θ_{xcr} and vertical θ_{ycr} angles of crystal alignment and bending angle φ and crystal

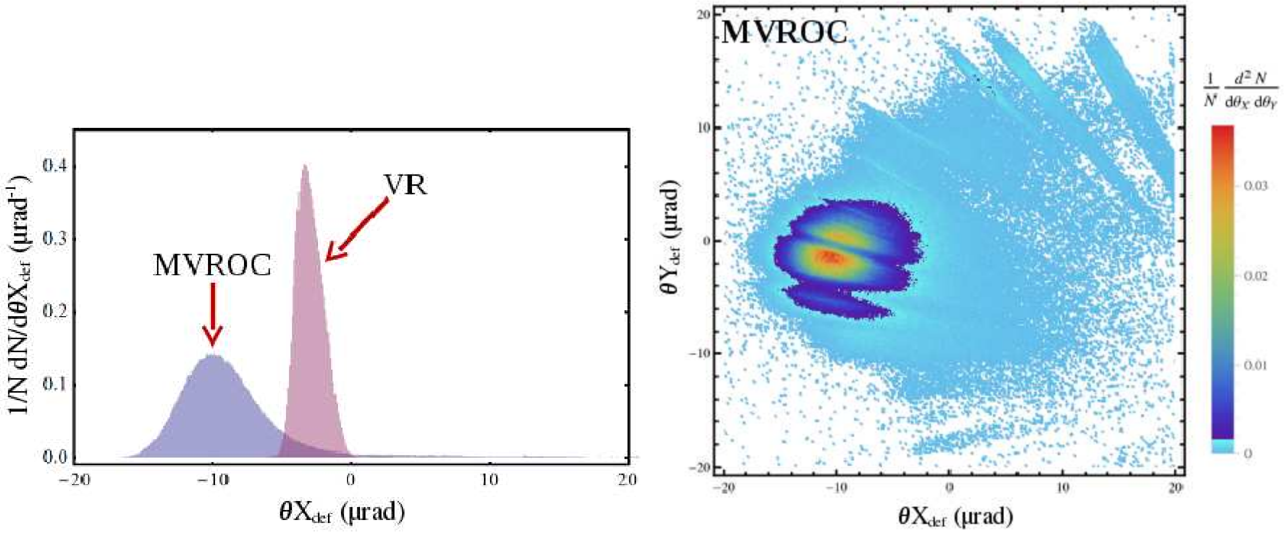

Figure 3.7: Angular distribution on horizontal (left) and both horizontal and vertical (right) angles behind the bent silicon crystal for MVROC of 7 TeV protons. The crystal length is $l_{cr} = 4mm$, the bending angle $\theta_b = 60\mu rad$, the angular alignment $\theta_{xcr} = -30\mu rad$, $\theta_{ycr} = -12\mu rad$ w.r.t. <111> axes. For comparison a single volume reflection from (110) plane of the same crystal is also presented in left Fig.

length l_{cr}. The first condition is that both angles of crystal alignment should be at least 3-4 times higher on module than the axial critical angle [4] ($\theta_{ycr} \approx 4\theta_{Lax} \approx 8\mu rad$ at 50 TeV) to avoid axial channeling.

The second condition establishes the crystal orientation for the beam to be volume reflected by the strongest skew plane ((110) for <111> axes). The inclination angle of the plane should exceed the angle of the plane of particles incidence to the crystal:

$$\alpha_{pl} > \arctan(\theta_{ycr}/\theta_{xcr}) \tag{3.7}$$

for a plane to reflect particles [24, 107]. For <111> axes it will be transformed into condition:

$$\theta_{xcr} < \theta_{ycr}\sqrt{3}, \tag{3.8}$$

in which the sign $>$ is changed to $<$ because angles of crystal alignment are negative. To avoid capture into the channeling mode θ_{xcr} should be smaller at least on 1-1.5 θ_{Lax}. For instance for the energy of 50 TeV one can choose $\theta_{xcr} = -17.5\mu rad$ and $\theta_{ycr} = -8\mu rad$.

The third condition determines the bending angle for the beam to be reflected by all main crystal planes as the symmetrical pairs. By the vertical symmetry of the crystal lattice this angle should be twice larger on module than the horizontal incidence angle:

$$\varphi = -2\theta_{xcr}, \tag{3.9}$$

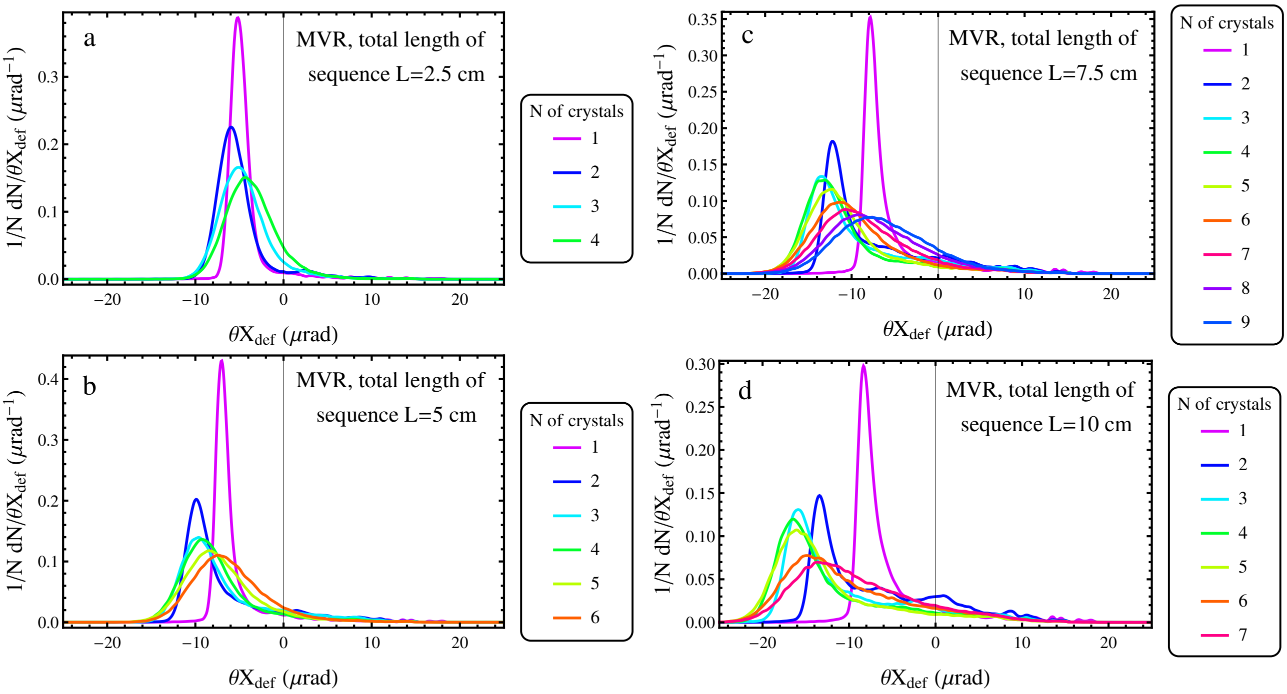

Figure 3.8: Angular distribution behind the crystal for MVROC of 50 TeV protons in one and in a sequence of <111> bent silicon crystals. The alignment and geometry of crystals are calculated according to (3.8-3.13).

giving in our case $\varphi = 35\mu rad$.

The optimal length of the crystal can be obtained from the condition of optimal R for single volume reflection (3.3). However, it is limited by experimental conditions, therefore should be as high as possible.

An example of deflection angle distribution for the MVROC effect is presented in Fig. 3.7 at the LHC energy of 7 TeV as well as compared with single volume reflection from (110) plane. This picture confirms the superiority of MVROC w.r.t. VR as well as compensation of vertical deflection angles by different skew planes.

For the amplification of the deflection angle it is proposed to apply *MVROC in a sequence* of crystals similarly to the technique from the previous section. In a such setup it is very important to avoid capture in the channeling mode by skew crystal planes. Thereby, the condition (3.8) should be fulfilled for all the crystals in the sequence. Therefore, the angle of crystal alignment w.r.t. deflected beam by all the crystals except the last one θ_{xf} should also fulfill this condition:

$$\theta_{xf} < \theta_{ycr}\sqrt{3}. \tag{3.10}$$

The difference between θ_{xf} and θ_{xcr} is equal to the deflection angle by all the crystals except the last one $\theta_{xf} - \theta_{xcr} = (n-1)\alpha_{MVROC}$. The angle of deflection by means of MVROC α_{MVROC} can be estimated as 5 angles of single volume

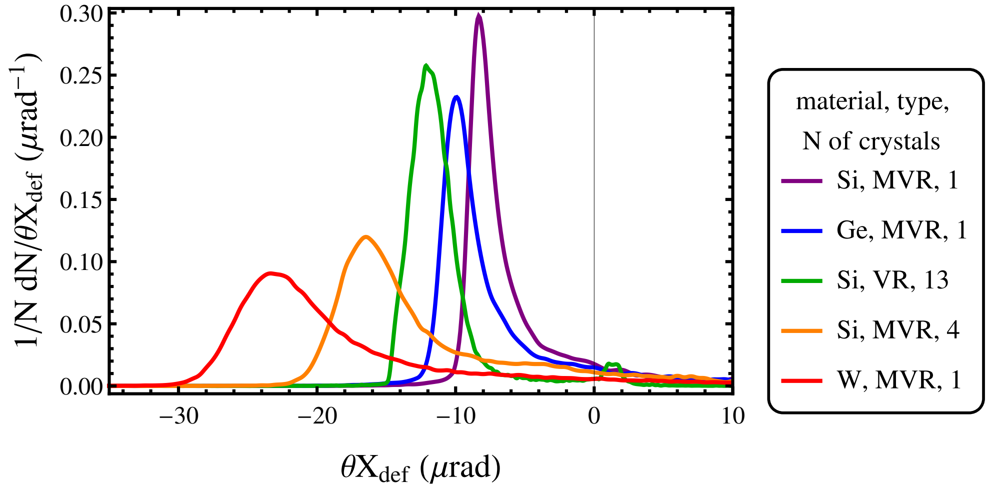

Figure 3.9: Comparison of angular distribution behind the crystal for volume reflection and MVROC of 50 TeV protons in one and a sequence of bent silicon crystals and MVROC in bent germanium and tungsten crystals. The length is 10 cm of the silicon crystal or crystal sequence, 5.4 cm of the germanium crystal and 1.9 cm of the tungsten crystal.

reflection [23, 24, 107], calculated above by Eqs. (3.1-3.2), giving:

$$\theta_{xf} - \theta_{xcr} = 5(n-1)\theta_L < \frac{\alpha}{\theta_L} > (\eta). \tag{3.11}$$

The angle θ_{xcr} can be defined by the condition (3.9). However, it is different for any crystal because of deflections. We suggest to use the average value of the crystal alignment for the first and the last crystal in a sequence $\frac{\theta_{xcr}+\theta_{xf}}{2}$ transforming the condition (3.9) into:

$$\varphi = -\theta_{xcr} - \theta_{xf}. \tag{3.12}$$

Expressing φ from Eq. (3.5), θ_{xcr} from Eq. (3.12) and substituting it into (3.11), one obtains an equation for the variable η for MVROC analogically to Eq. (3.6):

$$2\theta_{xf} + L_{seq}/n\eta R_{cr} = 5(n-1)\theta_L < \frac{\alpha}{\theta_L} > (\eta). \tag{3.13}$$

The angles θ_{xf} and θ_{ycr} are calculated by the same way as for the case of a single crystal. However, we lowed them a bit: $\theta_{xf} = -14\mu rad$ and $\theta_{ycr} = -7\mu rad$ to decrease the bending angle and to increase the deflection angle.

Analogical simulations to that, shown in Fig. 3.5, were conducted for MVROC both in a single crystal and in a sequence of silicon crystals with application of CRYSTAL simulation code [A1, A3] with the statistics of 200000 particles. The results are presented in Fig. 3.8. The initial parameters were optimized according to (3.8-3.13).

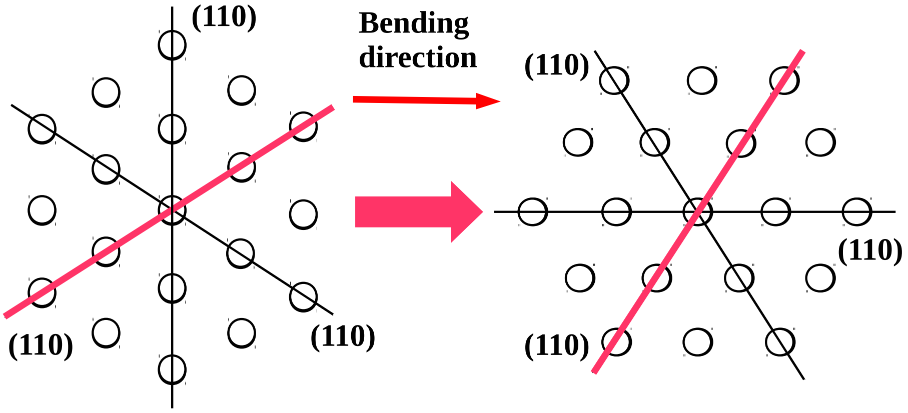

Figure 3.10: Rotation of crystal lattice for application of channeling in skew planes. In both case crystal is bent horizontally. Red line indicates the plane (110) used for channeling.

One can conclude that the optimal number of crystals varies from 2 to 3-4 for the sequence length from 2.5 cm to 10 cm. This is considerably less than the number of the crystals for single volume reflection case. Nevertheless, MVROC in a sequence of crystals provides considerably higher deflection angle than single volume reflection, 16.5 μrad and 12 μrad respectively for $L_{seq} = 10cm$. The comparison of these cases and the case of MVROC only in one crystal (the peak angle is 8.3 μrad) is shown in Fig. 3.9.

However, it is important to underline, that in some cases there is an increase of particle fraction deflected by a low angle, which one can notice in both Figs. 3.8-3.9. This is explained by reduction of fraction entering in the next crystal after deflection by the previous one, being at still optimal conditions for MVROC. Such particles can be, for instance captured by skew crystal planes and deflected in opposite direction. This effect must be also taking into account during parameters optimization for a concrete collimation system.

The problem of deflected fraction on a small angle exists for any coherent effect. This is one of the main problems of collimation inefficiency and must be critically compared during the coherent effect choice and optimization.

In this figure simulations of MVROC in crystals of other materials are also presented, in particular in germanium and tungsten crystals. The atomic strings in crystals of heavy elements possess higher field deflecting particles on higher angles. However, the length of such crystals should be reduced in comparison with silicon to reach the same probability of nuclear inelastic interactions. Anyway they provide larger deflection angles w.r.t. silicon crystals. In particular, the peak deflection angle for 50 TeV protons reaches 23 μrad for tungsten crystal. It 1.4 times exceeds the angle of MVROC in a sequence of Si crystals and twice exceeds the deflection angle of volume reflection in a sequence. Moreover,

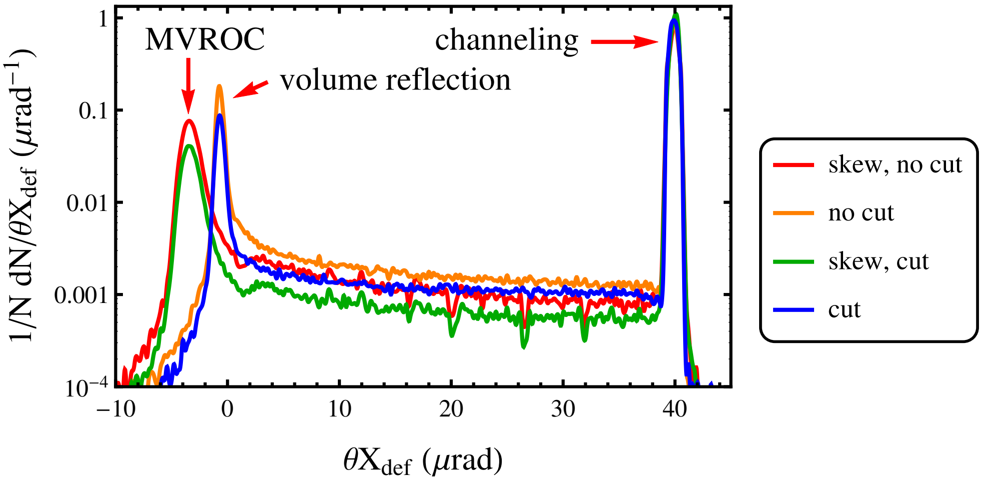

Figure 3.11: The deflection angle distribution behind a bent crystal of 5 cm long for planar channeling in vertical and skew (110) crystal planes of 50 TeV protons. The bending angle it 40 μrad and 53.3 μrad for vertical and skew crystal planes respectively. The parameters of crystal cut are calculated according to [112].

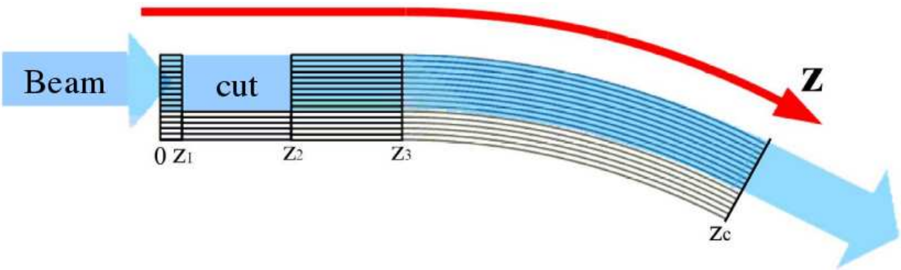

Figure 3.12: A bent crystal with a cut.

potentially the technique MVROC in a sequence can be applied also for tungsten crystals which can double the deflection angle. In addition, it produces one of the lowest fraction of particles deflected at small angles. Thus, all of this can be applied for the crystal-based collimation system.

3.4 Channeling in skew crystal planes and a crystal with a cut

There is a possibility to combine the advantages of channeling and MVROC [A2, A5]. For this we suggest to align the crystal for channeling in skew crystal planes instead to avoid it. In other words, in this case the inequality (3.8) becomes equality, changing the optimal crystal orientation only in x-plane. However, the (110) skew plane with a $\alpha_{pl} = 30°$ is not very useful because provides too high angle in vertical plane and too low in the horizontal one. To double the latter one can rotate the crystal lattice on 30° as shown in Fig. 3.10. The condition (3.8) will be rewritten as:

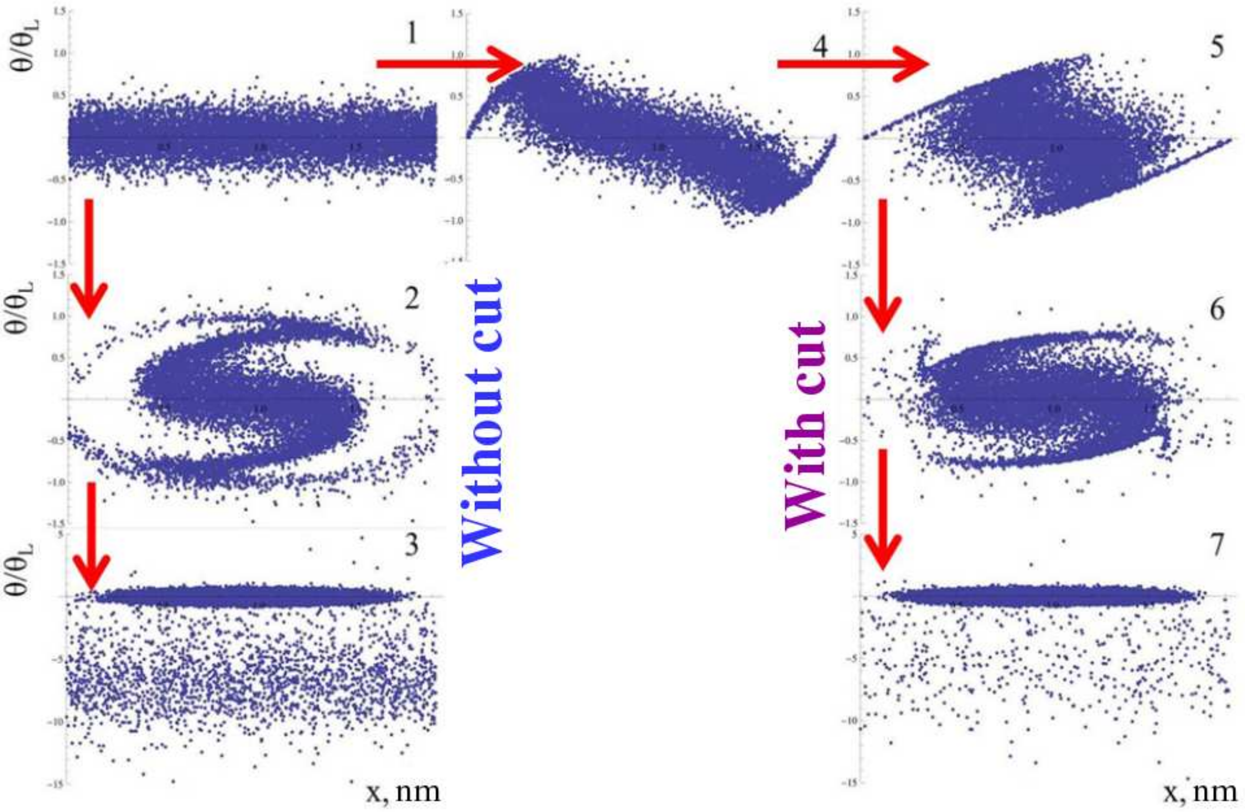

Figure 3.13: Phase space in different points of the crystal (see Fig. 3.13), 1: $z = 0$; 2: $z = 0.01 l_{cr}$; 3: $z = l_{cr}$; 4: $z = z_1$; 5: $z = z_2$; 6: $z = z_2 + 0.01 l_{cr}$; 7: $z = l_{cr}$; 1–3 without the cut, 4–7 with the cut.

$$\theta_{xcr} = \theta_{ycr}/\tan\alpha_{pl} = \theta_{ycr}/\sqrt{3}. \tag{3.14}$$

To reach the same deflection angle as for channeling in vertical planes, one should bend the crystal stronger $1/\sin^2\alpha_{pl}$ times. However, the channeling efficiency will not decrease. Moreover, channeling in skew crystal planes provides higher angular acceptance increasing the channeling efficiency. This is confirmed by simulations (with CRYSTAL simulation code [A1, A3] with a statistics of 10^6 particles, presented in Fig. 3.11. The efficiency of channeling in skew crystal planes reaches 80.5%, while for vertical planes it is 79%.

However, the main advantage of channeling in skew crystal planes is deflection of non-channeled particles by means of MVROC instead of volume reflection. MVROC deflects particles at the angle of 3.3 μrad which is 5 times stronger than volume reflection. This is very important for the crystal-based collimation system, because small deflection angle causes more additional passages of particles through the crystal and, consequently, increases the inelastic nuclear scattering rate. In opposite, the angles of MVROC are high enough to redirect almost all non-channeled particles onto the crystal 2 as shown in Fig. 3.1.

There is a possibility to increase the channeling efficiency in both cases by means of a narrow plane cut [112,113] see Fig. 3.12. To avoid the dechanneling for most particles it is necessary to prevent the particles approach to the high nuclear density regions. It can be achieved by means of a considerable transverse energy decrease.

If one makes a crystal cut it will allow to violate the transverse energy conservation by braking the longitudinal invariance of the planar potential. In other words, a particle will lose a part of its transverse energy by entering the cut. Then if one chooses the cut thickness correctly, a particle will get less transverse energy after the cut passage, than it has lost.

Involving of most of particles in this process is determined by similarity of phases in the channeling mode at the crystal entrance. Therefore, one can focus synphasely particles in the cut to the center of the channel. An example is shown in Fig. 3.13 in the phase diagrams at the different longitudinal positions in a crystal both with and without the cut. The positions inside the crystal are indicated in Fig. 3.12. One can observe "beam squeezing" during and after passage of the cut. Consequently the particles will move far from crystal planes, which considerably decreases the probability of dechanneling.

Unfortunately, it works efficiently only for the beam angular divergence less than a quarter of the θ_L and requires a very exact crystal alignment of the same order. Anyway, in the current case (see Fig. 3.11) it allows one to increase the channeling efficiency up to 87.5% for usual planar channeling and up to 89% for channeling in skew planes.

3.5 Double crystal-based collimation system

The main function of the collimation system as well as of coherent effects proposed is to intercept as more particles as possible during only one passage through betatron cleaning insertion. Therefore, a considerable decrease of non-intercepted particles fraction w.r.t. the standart (single) crystal-based collimation scheme will testify an advantage of the new collimation scheme.

In order to verify this approach the crystal-based collimation scheme described in Fig. 3.1 was used [A5]. For simulations four variants of collimation scheme were chosen:

1) single collimation scheme with the first crystal, bent along (110) vertical planes, and with an absorber at 12.6 σ instead of the second crystal;
2) the same with the first crystal with a cut;
3) double crystal-based collimation scheme with the first crystal, aligned for channeling along (110) skew crystal planes, formed by <111> axes, and the

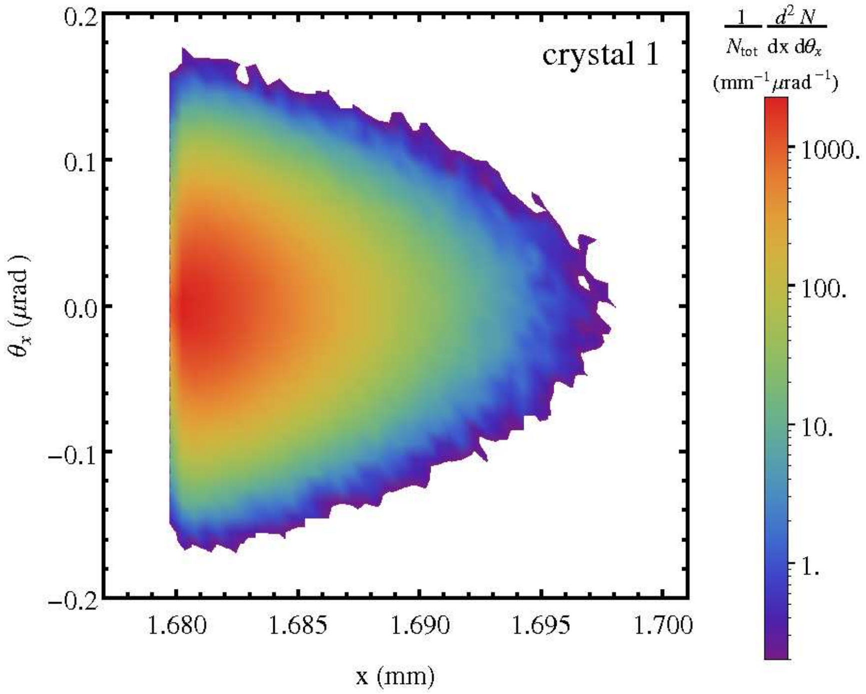

Figure 3.14: Beam phase space at the first crystal entrance.

second one, designed for the MVROC effect;
4) the combination of 2) and 3).
The parameters of the first crystal are the same as in simulations, presented in Fig. 3.11, i.e. a 5 cm silicon crystal, with the bending angle of 40 μrad for vertical and 53.3 μrad for skew (110) crystal planes, ideally aligned for the channeling mode. The second crystal is the same as used in simulations, shown in Fig. 3.9, namely a 10 cm silicon crystal, with the bending angle of 35 μrad.

The beam distribution at the first crystal entrance, generated using the diffusion model [N3], is shown in Fig. 3.14. The angular divergence, being approximately 0.04 μrad, is considerably lower than the Lindhard angle. The Future Circular Collider parameters [119, 121–125] were used for all our simulations. The simulations were carried out by CRYSTAL simulation code [A1, A3] with a statistics of 10^6 particles in each case, taking into account both betatron and synchrotron oscillations. The absorbers are assumed to intercept all the incident particles.

The beam phase space was generated at the longitudinal positions of the first absorber/second crystal and the second absorber for all the variants of collimation schemes, as shown in Figs. 3.15-3.16. In the latters one can also easily distinguish the coherent effects deflecting the particles. In order to demostrate the amount of particles, intercepted by the absorber, all phase spaces were normalized to the total number of particles, passed through the cleaning insertion N_{tot}.

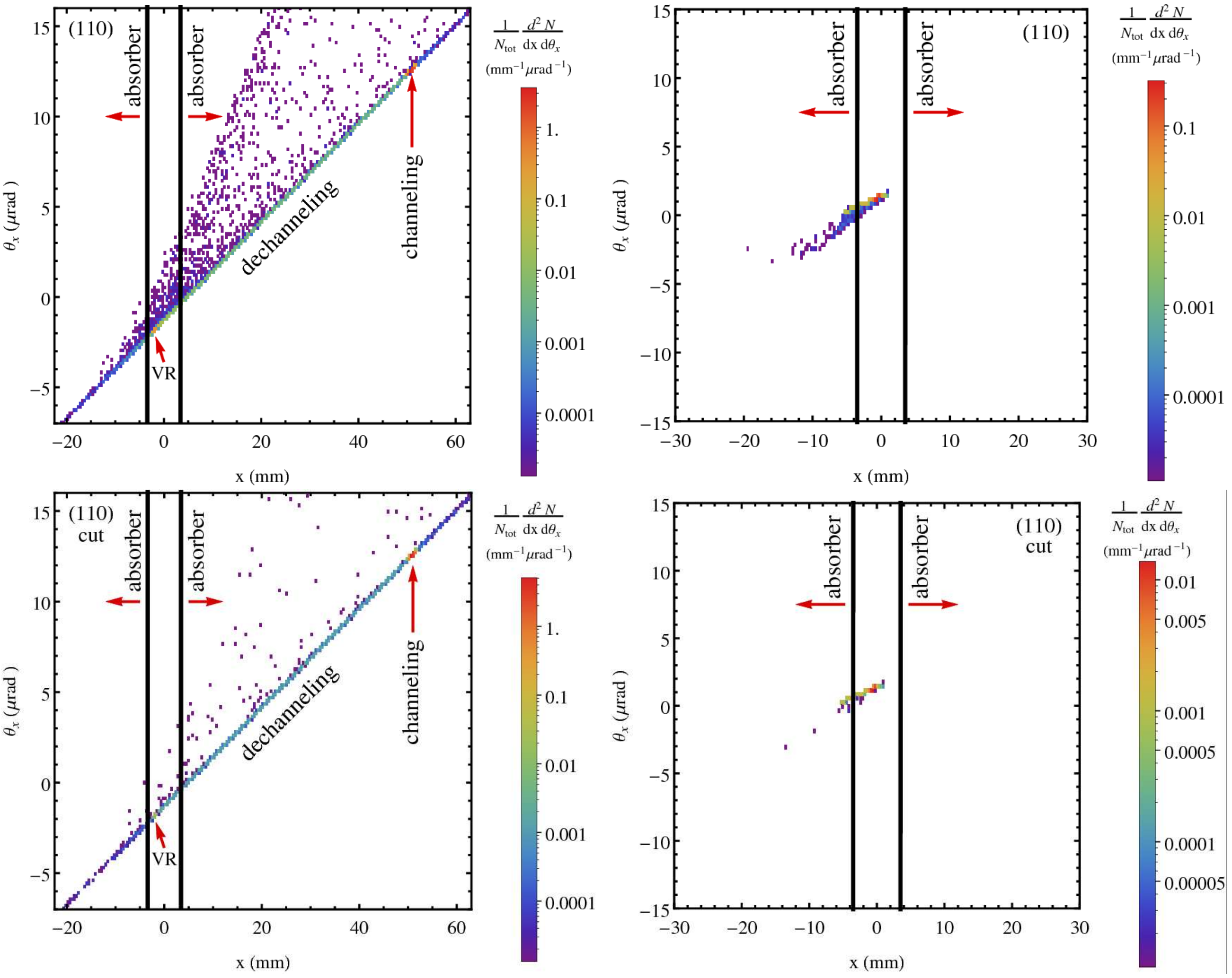

Figure 3.15: Beam phase space, normalized to the total number of particles, passed through the cleaning insertion, at the position of the first (left) and the second (right) absorber for single crystal-based collimation system. The Si crystal the same as in Fig. 3.11, aligned for planar channeling in (110) vertical crystal planes without cut (top) and with cut (bottom). The crystal and the absorbers are placed at 7.2 and 12.6 σ, respectively.

The crystal with the cut, providing considerably higher channeling efficiency, demostrates considerable reduction of particles, non-intercepted by the betatron cleaning insertion, namely from 9.6% (without the cut) down to 0.5% (with the cut). One can easily observe this result from the scale in the right column of Fig. 3.15 decreased on an order of magnitude for the crystal with the cut.

The double crystal-based collimation scheme also demonstrates a considerable decrease of non-intercepted beam fraction, namely down to 1.3% (see Fig. 3.16). Moreover, since the deflection angle of non-channeled particles becomes considerably higher in the first crystal due to MVROC effect, channeling in skew planes also enhances the efficiency of the single crystal-based collimation scheme. Additionally, the application of the cut in the first crystal of the double

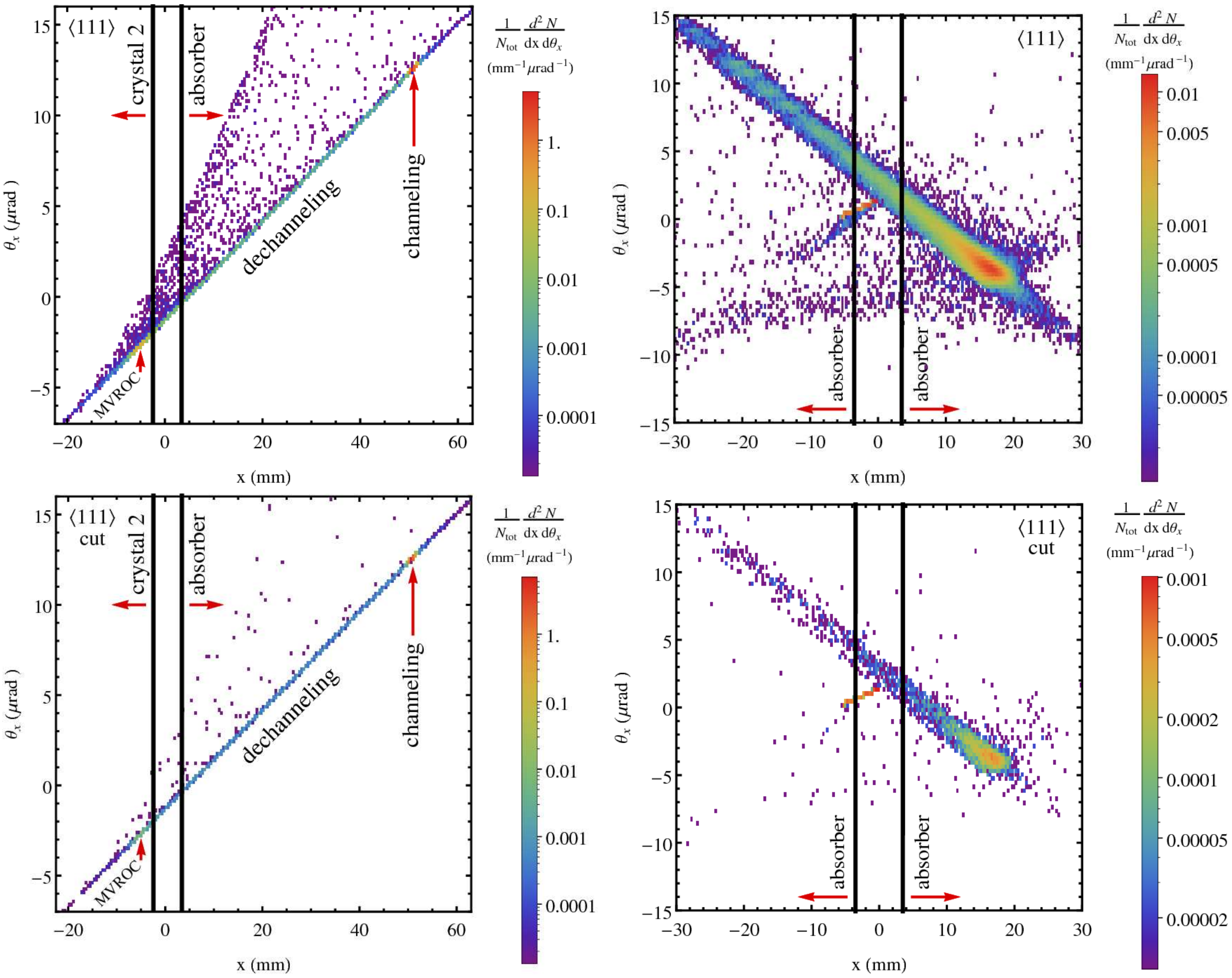

Figure 3.16: Beam phase space, normalized to the total number of particles, passed through the cleaning insertion, at the position of the first (left) and the second (right) absorber for double crystal-based collimation system. The first Si crystal the same as in Fig. 3.11, aligned for planar channeling in skew (110) crystal planes, formed by <111> axes, without the cut (top) and with the cut (bottom). The second Si crystal is the same as in Fig. 3.9, aligned for MVROC. The first and second crystal are placed at 7.2 and 9 σ, respectively, as well as the absorbers are placed at 12.6 σ.

collimation system reduces the non-intercepted fraction on one more order of magnitude, down to 0.1%.

Moreover, the impact parameters of particle incidence to absorbers are high enough to prevent particle leakage at the absorber boundaries. Therefore, the absorber length can be chosen high enough to intercept all the particles. For instance, for 1m long tungsten absorber the leakage, caused by non-absorbtion, is $\sim 4 \cdot 10^{-5}$, being $\sim 2 \cdot 10^{-9}$ for 2m of tungsten, calculated using nuclear interaction length [94].

Therefore, the double crystal-based collimation scheme as well as coherent effects proposed allow one to intercept approximately 99 % of particles by only one passage through the betatron cleaning insertion. The application of the crystal cut in the double crystal-based collimation scheme increases this number up to 99.9%.

3.6 Conclusions

The double crystal-based collimation system, combined with the layout of the betatron cleaning insertion of the Future Circular Collider [119], has been suggested, based on application of the second bent crystal to amplify the deflection angle of non-channeled particles and to reduce, therefore, the leakage to sensitive equipment. The effects of multiple volume reflection in one bent crystal, volume reflection in a crystal sequence as well as MVROC in a crystal sequence have been proposed for the second crystal. Though they also produce a fraction deflected on small angles, this fraction is considerably smaller, than that of the first crystal. Nevertheless, it must be also taking into account for a concrete collimation setup.

A theoretical model of optimization of crystal geometry and alignment has been proposed. It is mainly based on estimation of the dependence of the ratio of the volume reflection angle to the Lindhard angle on the ratio of the bending radius to its critical value, being independent on particle energy.

By this model the parameters of a bent crystal sequence were optimized for both volume reflection and MVROC at a fixed crystal number and length of the sequence. Monte Carlo simulations conducted for various lengths and crystal numbers allow one to choose the optimal crystal number for each length as well as to compare the peak deflection angle of volume reflection and MVROC.

Volume reflection in a silicon crystal sequence provides higher deflection angle than MVROC (12 μrad and 8.3 μrad at 10 cm of the length at the FCC energy of 50 TeV). However, MVROC in a silicon crystal sequence increases this angle up to 16 μrad. Additionally, it requires 3-4 crystals, while for volume reflection 13 crystals in a sequence are necessary at the given length. However, MVROC in heavy crystals allows one to reach deflection angles even higher, in particular 23 μrad for the tungsten crystal.

For the first crystal in the double crystal-based collimation system channeling in skew planes have been suggested. On the one hand it five times increases the deflection angle of non-channeled particles by means of application of MVROC instead of volume reflection. On the other hand it increases the angular acceptance and, therefore, the channeling efficiency, in particular from 79% up to 80.5% in the case simulated. In addition, the application of a crystal cut has been suggested allowing one to increase the channeling efficiency from 79% and 80.5% up to 87.5% and 89%.

The double crystal-based collimation system as well as all the effects of particle deflection by a bent crystal listed above allow one to intercept approximately 99 % of particles by only one passage through the betatron cleaning insertion at the FCC. The application of the crystal cut increases the intercepted fraction up to 99.9%. Moreover, high impact parameters of particle incidence to absorbers prevent leakage at the absorber boundaries. Therefore the collimation schemes proposed are potentially applicable at high-energy accelerators and colliders, in particular the Future Circular Collider.

CHAPTER 4

STEERING OF 855 MEV ELECTRONS BY SI AND GE BENT CRYSTALS

4.1 Introduction

Over the years, positive particle beam steering has been well investigated in a wide range of energies, from few MeV up to the recent result at LHC with 6.5 TeV protons. Conversely, the negatively charged particle case has been poorly investigated and only recently, thanks to the realization of very short bent Si crystals, it has become possible to steer negatively charged particles beams [10, 14, 19, 27, 29–31, 51–53, 55]. However, the possibility to steer electron beams is promising for applications in electron-positron collider collimation systems [53, 126–129] as well as innovative high-intensity X- or γ-radiation sources [51–53, 55, 56].

Usually, silicon is selected as prime material for the fabrication of bent crystals due to its high-quality crystalline lattice and low cost. Nevertheless, other materials, like germanium, which provides a higher atomic number, Z, than silicon and can be also realized with a similar perfection, deserve investigation. Indeed, since a Ge crystal provides a stronger potential, one expects an increase in the angular acceptance for channeling and an enhancement of e.m. radiation emission. Currently, a few channeling experiments have been performed with bent Ge, only with positively charged particles and only in the hundreds GeV energy range [15–18], while with electrons and at lower energies there are no data in literature due to the technical difficulties of fabrication of an ultra-short bent Ge crystal.

Only recently an investigation on sub-GeV electron steering by both silicon and germanium bent crystals under channeling and VR has been carried out [A7]. With the aim of determining the different behavior of these effects vs. the atomic number Z, two 15 μm Si and Ge crystals, bent along the (111) planes, were selected and an experiment was performed at the Mainz Mikrotron (MAMI) with 855 MeV electrons. The dependence of the channeling efficiency and of the dechanneling length, which is the main parameter for planar channeling, on the crystal curvature has been also investigated for the first time with electrons and absolutely for the first time with a germanium crystal.

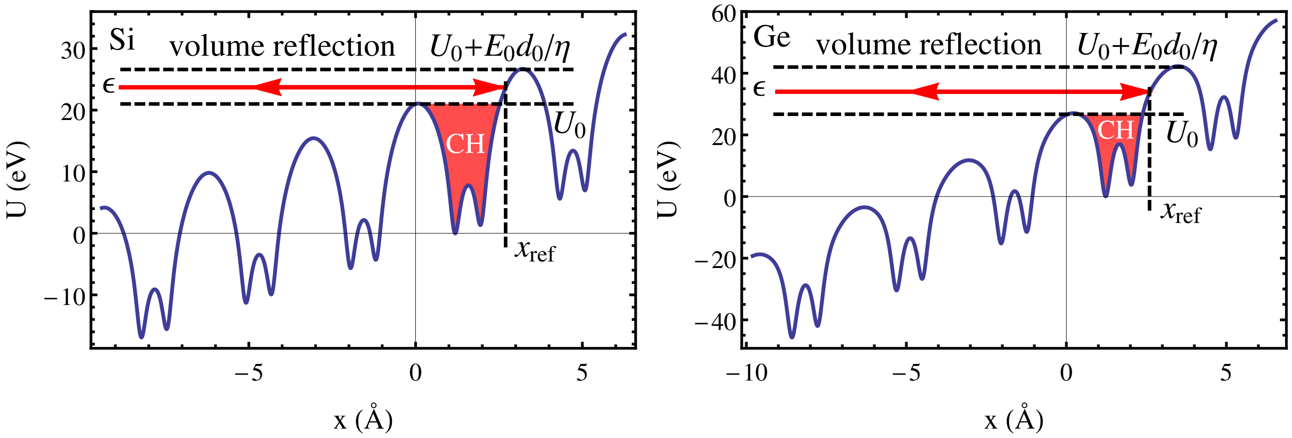

Figure 4.1: Interplanar potential of (111) Si and Ge crystals for maximal bending radii (4.76 cm and 1.83 cm respectively) used in the experiments.

4.2 Channeling, dechanneling and VR of sub-GeV electrons

Channeling proved to be an efficient way to steer positive particle beams, achieving deflection efficiencies larger than 80 %. On the other hand, the maximal deflection efficiency for electrons recorded in the literature slightly exceeds 20 % [29] and is about 30 % for negative pions [28]. The main source of inefficiency is *dechanneling*, which consists in particles escaping from the channeling mode caused by Coulomb scattering on atoms [62,63,98]. The main pecularity of channeling of electrons at sub-GeV energy is rather large angle of multiple scattering, being comparable with the Lindhard angle even for short crystals, i.e. of several channeling oscillation lengths. For 855 MeV electrons at MAMI channeled in the (111) planes one obtains the following values of the Lindhard angle: $\theta_{L,Si} = 232\ \mu$rad and $\theta_{L,Ge} = 274\ \mu$rad, for Si and Ge, respectively.

As was mentioned in previous chapters, the process of dechanneling is determined by the dechanneling length, which is the mean free path of a channeled particle before its transverse energy becomes larger than the potential barrier, thus escaping from the channeling condition (CH in Fig. 4.1, representing interplanar potential in bent silicon and germanium crystals for experimental conditions, considered below). Electron dechanneling lenght has already been experimentally measured with Si straight [34–36] and bent [14, 29–31] crystals. In contrast to positrons, electrons dechannel faster [14, 29–31, 62, 63, 98]. Indeed, negatively charged channeled particles oscillate around atomic planes, thereby being more subject to the strong scattering with lattice nuclei.

The dechanneling length L_{dech} is usually defined [62] according to the dependence of the channeling fraction population f_{ch} on the penetration depth z (compare (1.58,1.73)). As was mentioned in the first chapted negatively charged particles cross the crystal planes, being in the channel center. Consequently nuclear dechanneling plays the main role for all the negative particles, not only with large amplitude as for the positive once. Therefore, it is enough to consider only one exponent from (1.73):

$$f_{ch} = A_0 \exp(-z/L_{dech}), \tag{4.1}$$

where A_0 is the normalizing factor.

Both the dechanneling lenght and exponential channeling fraction decay were introduced by Kumakhov to describe the dechanneling process induced by electron scattering of non relativistic ions. This approach is well grounded for positively charged particles [62], while even the recent inclusion of nuclear scattering [98], which is dominant for the dechanneling of negative particles, failed to extend quantitatively the same approach to this second case. Despite all this, the usage of the dechanneling length is justified by the practical use as a qualitative characteristical lenght for channeling, which depends on the crystalline material, thichkness and bending radius. Thereby, extrapolating L_{dech} from experimental results is of interest for channeling application.

The main diffuculty on the theoretical description of electron dechanneling process is the frequent strong changes in the negative particle transverse motion that leads to a limited applicability of a diffusion approach. These effects can anyway be taken into account in Monte Carlo simulations. For instance, the process of recapture under the channeling conditions of a dechanneled particle, the so-called rechanneling, was described well only using Monte Carlo simulations [29]. However, in first approximation the exponential character of dechanneling (Eq. (4.1)) for negatively charged particles is maintained for highly-bent crystals, as shown by different experiments as well as Monte Carlo simulations [28–31], ensuring its usage for our experimental cases (see below).

The volume reflection process can be treated for the negatively charged particles in the same way as for the positive ones. Therefore the formulae (3.1-3.2), allowing one to calculate the maximal angle for VR are still valid. The only difference is the correct usage of the interplanar potential being turned over for negative particles (see Figs. 1.11,4.1). One must remember that the volume reflection angle [99, 100] can be calculated by (3.1-3.2) in a form independent of the beam energy. However, these formulae do not take into account multiple scattering, though they provide a good estimate of the volume reflection peak position, as will be shown below. Since formulae (3.1-3.2) hold for both positively and negatively change particles, they will be applied for electrons.

All the coherent effects mentioned above, such as channeling and VR, are strongly dependent on the ratio between the initial transverse energy and the

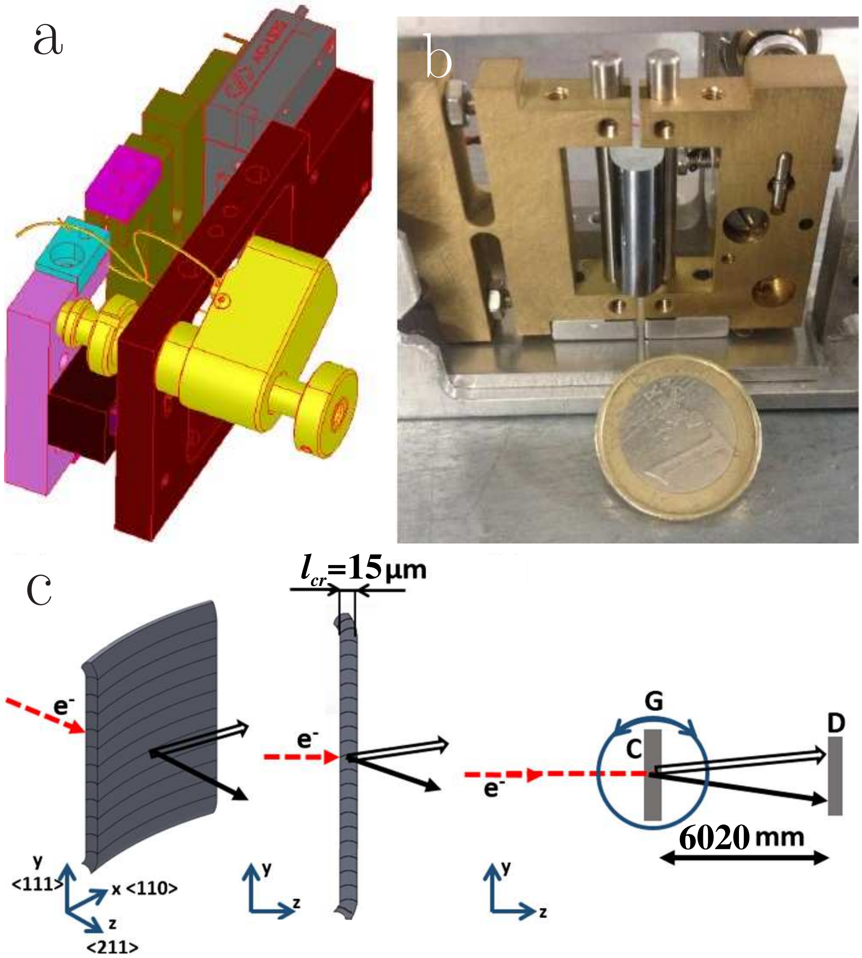

Figure 4.2: Piezo motor (a), dynamical holder (b) and bending of a silicon crystal (c). The dashed arrow indicates the incoming beam, impinging on the crystal mounted on a high-precision goniometer (G). The solid-black arrow indicates particles deflected under the channeling mode, while the solid-white arrow corresponds to VR particles. The deflected beam impinges on the LYSO Screen (D).

planar potential well depth, which depends on the bending radius, and hence on the incidence angle. In this work, a detailed and quantitative investigation of this dependence will be presented, to obtain the optimal parameters of bent crystals for applications.

4.3 Bent crystal manufacturing and experimental setup

A sample holder prototype aimed to bend the crystal with a remote controlled system was realized at the INFN-LNL lab in Legnaro, Italy. This innovative holder permitted to experimentally investigate important bent crystal parameters for application, such as the channeling and VR deflection angle and efficiency and the dechanneling length as a function of the curvature radius R, without manually re-bending the crystal. This allows a smooth increase of the curvature, performing it by numerical control, avoiding stress concentrations that causes the sample breaking during the mounting procedures in a normal fixed curvature sample holder. The sample holder is also equipped with a remotely controlled distortion correction system. If the sample curvature is not perfect, the channeling angle could vary along the beam dimension (torsion) causing a detrimental effect on efficiency [130]. The correction system is an additional degree of freedom allowing one to vary the torsion when the sample is into the chamber, to immediately check the effect on the efficiency. Furthermore, this innovative holder permits to re-bent the crystal without vacuum breaking, permitting a considerable speed up of the data taking to access a more extended set of data.

Fig. 4.3a shows the piezo motor step (grey) that translates a movable part (green) with respect to a fixed one (brown). It can be done with 400 nm steps. Two plugs are in-built in the two parts and translate one against the other by actioning the step motor. The plugs (steel cylinders) have two rabbets to secure the sample by a special gluing procedure. The plugs can rotate freely in brass holes and are supported by pins screws. When the plug gets closer due to translation caused by the motor, the sample is forced to bend (see Fig. 4.3b). To regulate the torsion a fine movement is obtained by a never ending piezo driven screw (yellow) that pushes a rotating part (magenta) containing the plug hole. The angular resolution is better than 1 μrad. The system was calibrated in order to know the primary curvature radius as a function of the number of steps of the translator motor. The capability of the second motor to modify the crystal torsion was verified by means of high-resolution X-ray diffraction.

The 15 μm long Si and Ge crystals samples were sequentially mounted onto the dynamical bending holder; the picture in Fig. 4.3b shows the Si sample mounted on the holder. Such an ultralow length is essential for our experiment, because it must not exceed too much the dechanneling length as well as to reduce the multiple scattering angle. A bending moment supported the crystal at two opposite edges, leaving it free at the remaining edges. In this way, the crystal surface, which is parallel to the (211) planes, was bent along the (111) direction, obtaining a secondary bending of the (111) planes due to the quasimosaic effect [131]. The advantages of crystals exploiting the quasimosaic effect is represented by the possibility to manufacture ultra thin crystals large enough to completely intercept the beam. In addition, due to the shape of the potential well, the (111) bent planes (see Fig. 4.1) are the most efficient for the deflection of negatively charged particles. The anticlastic effect could be a drawback of quasimosaic bent crystals but in the case of the present data, the large bending and small thickness guarantee a complete anticlastic suppression as demonstrate in [132]. This was checked by high resolution X-ray diffraction by measuring the (111) orientation at different positions along the y-axis. No anticlastic trend was evidenced with an exception of about 2mm close to the sample border. On the other hand, a residual variation of the (111) plane orientation of about ± 50 μrad inside the dimension of the measuring X-ray beam (100 μm) was evidenced. This is interpreted as a residual sample rippling induced by imperfections caused by the glueing procedure.

An experiment was carried out in the Hall B of the Mainzer Mikrotron (MAMI) with 855 MeV electrons. The experimental setup is the same as in [133] with the substitution of the Si microstrip detector to measure the beam profile after the interaction with the crystal with a LYSO Screen (see Fig. 4.3c). The screen has a thickness of 200 μm and is inclined of 22.5 degrees toward the camera in the perpendicular direction with respect to the beam deflection plane and was placed downstream the crystal of 6020 mm. The crystal holder was mounted on a high-precision goniometer with 5 degrees of freedom. Translations along the x and y axes were used to geometrically align the crystal with the beam direction, while rotations around the x, y and z axes with an accuracy of 17.5, 30, and 50 μrad respectively, were used to achieve angular alignment of the crystal planes with the electron beam. The entire experimental setup was kept under vacuum to avoid multiple scattering of the beam by air. The beam was focused through dedicated quadrupole lenses: the resulting beam size and angular divergence were 105 μm and 21 μrad along the vertical direction, which is the crystal bending direction. The beam divergence is smaller of the Lindhard critical angle for channeling, which is about 220 μrad at 855 MeV. A schematic view of the experimental setup is shown in Fig. 4.3c: it allows to characterize, with very high precision, Si and Ge crystals in terms of both deflection efficiency and dechanneling length.

4.4 Experimental results and analysis

By exploiting the dynamical bending holder, channeling and VR of 855 MeV electrons was tested for 4 and 3 different curvatures in case of Si and Ge crystals, respectively. For each bending radius, R, the distribution of the particles angles θ_x after the interaction with the crystal θ_{Xdef} vs. crystal-to-beam orientation θ_{cr} was measured by rotating the goniometer around the ideal alignment with bent (111) planes. As an example, the experimental angular scan for the silicon

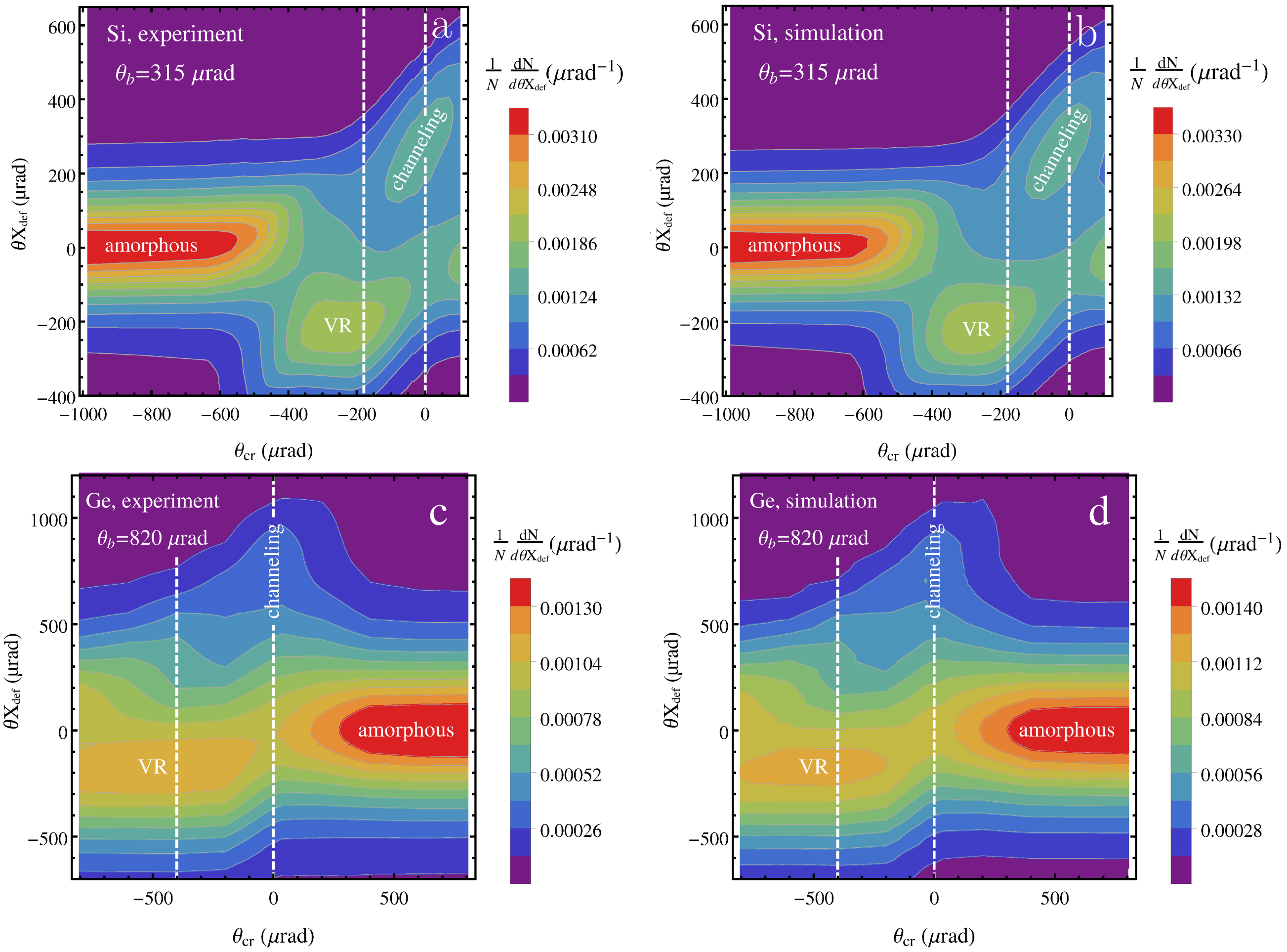

Figure 4.3: Experimental (a,c) and simulated (b,d) angular scans. Deflection angle vs. the crystal-to-beam orientation of Si (a,b) and Ge (c,d) crystals, bent at 315 μrad and 820 μrad respectively. Vertical white dashed lines represent the distributions in Fig. 4.4 at both channeling and volume reflection orientation.

crystal with a deflection angle of $\theta_b = 315$ μrad and the germanium crystal of $\theta_b = 820$ μrad are shown in Fig. 4.3. Fig. 4.4 shows the beam deflection distributions with Si and Ge crystals oriented in channeling and in the middle of VR region, for the angular position highlighted by dashed lines in Fig. 4.3. These plots allow one to follow the transition between the main processes occurring while changing the crystal-to-beam orientation. In the angular distributions for channeling orientation ($\theta_{cr} = 0$) the right peak represents the channeling mode as well as the left one is for the over-barrier particles. By decreasing θ_{cr} to about the middle of the range $[-\theta_b + \theta_L; -\theta_L]$ one sets up the VR orientation. At the latter, the right peak represents volume captured particles. Finally, a crystal alignment beyond this range suppresses all the coherent effects, leading to the "amorphous" region where multiple scattering dominates.

The crystal bending angle and alignment has been measured experimentally and verified by computer simulations using the CRYSTAL simulation code [A1,

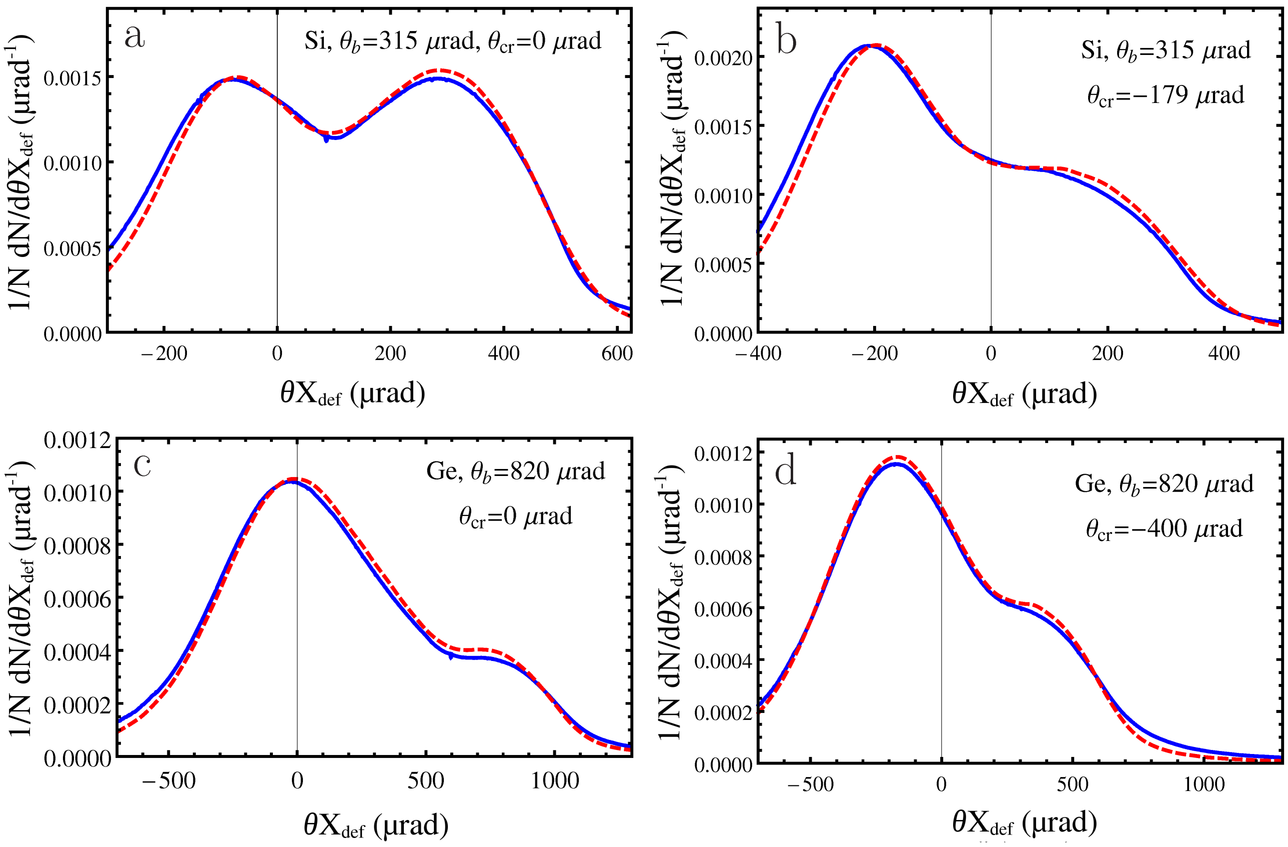

Figure 4.4: Experimental (solid) and simulated (dashed) distributions of deflected beam by Si (a,b) and Ge (c,d) crystals, bent at 315 μrad and 820 μrad respectively, for channeling (a,c) and volume reflection (b,d) crystal alignment. These curves are represented by white vertical lines in Fig. 4.3. Experimental values represent the projection of the beam spot collected by the screen along the vertical direction (y) of bending. Simulations were performed with a statistics of $5 \cdot 10^6$ particles for each plot.

A3]. The perfect alignment with bent planes, i.e., $\theta_{cr} = 0$, was experimentally determined by the highest intensity of the channeling peak, recorded during the angular scan. The channeling peak position also provided the crystal bending angle, verified by CRYSTAL simulations. The Monte Carlo simulations permitted to take into account the incoming angle distribution and sample rippling. The outcomes of the CRYSTAL code with a statistics from $2 \cdot 10^6$ up to $5 \cdot 10^6$ particles are displayed in Figs. 4.3 and 4.4 for comparison with experimental measurements.

The analysis of the angular distributions was carried out through a fitting procedure based on the one presented in Refs. [14, 31]. The fitting function represents the sum of the channeling part, described by gaussian:

$$\frac{df_{ch}}{d\theta_{Xdef}} = \frac{A_{ch}}{\sigma_{ch}\sqrt{2\pi}} \exp\left(-\frac{(\theta_{Xdef} - \theta_{ch})^2}{2\sigma_{ch}^2}\right), \tag{4.2}$$

the volume reflection part, containing also a non-reflected overbarrier fraction and described by the sum of two gaussians:

$$\frac{df_{VR}}{d\theta_{Xdef}} = \frac{A_{VR}}{\sigma_{VR}\sqrt{2\pi}} \exp\left(-\frac{(\theta_{Xdef}-\theta_{VR})^2}{2\sigma_{VR}^2}\right) + \frac{1-A_{VR}}{r\sigma_{VR}\sqrt{2\pi}} \exp\left(-\frac{(\theta_{Xdef}-\theta_{VR})^2}{2r^2\sigma_{VR}^2}\right) \quad (4.3)$$

and the dechanneling part, being an exponential distribution, convolved with the first gaussian in (4.3):

$$\begin{gathered}\frac{df_{dech}}{d\theta_{Xdef}} = \frac{A_{dech}}{2\theta_{dech}} \exp\left(\frac{\sigma_{VR}^2}{2\theta_{dech}^2} + \frac{\theta_{ch}-\theta_{Xdef}}{\theta_{dech}}\right) \times \\ \left(\operatorname{erf}\left(\frac{\theta_{VR}-\theta_{Xdef}+\frac{\sigma_{VR}^2}{\theta_{dech}}}{\sqrt{2}\sigma_{VR}}\right) - \operatorname{erf}\left(\frac{\theta_{ch}-\theta_{Xdef}+\frac{\sigma_{VR}^2}{\theta_{dech}}}{\sqrt{2}\sigma_{VR}}\right)\right).\end{gathered} \quad (4.4)$$

The total fitting function can be written as:

$$\frac{1}{N}\frac{dN}{d\theta_{Xdef}} = \frac{df_{ch}}{d\theta_{Xdef}} + B_{VR}\frac{df_{VR}}{d\theta_{Xdef}} + \frac{df_{dech}}{d\theta_{Xdef}}. \quad (4.5)$$

In (4.2-4.5) A_{ch}, A_{VR}, B_{VR}, A_{dech} and r are the normalizing factors, θ_{ch}, θ_{VR} and σ_{ch}, σ_{VR} the mean angles and the standard deviations of corresponding gaussians respectively as well as θ_{dech} the "dechanneling angle", defining the dechanneling length, found from the angular distribution, as $L_{dech} = R\theta_{dech}$. The channeling efficiency is defined as the integral value of the gaussian fit of the channeling peak (4.2), within $\pm 3\sigma_{ch}$ around the channeling peak, namely $\eta_{ch} \approx 0.9973 A_{ch}$.

The fit procedure was carried out in two steps. First, Eq. (4.3) was applied for the fit of the angular distribution of the crystal, aligned in amorphous direction. The values A_{VR} and r, extracted in the first step were used in the fit (4.5) [14,31].

The main difference with the fitting procedure from [14,31] are the coefficients A_{ch}, B_{VR}, A_{dech}, treated independently. Though the increase of the free parameters number reduces the accuracy, it is necessary in this case for a correct description of initially overbarrier particles, as will be explained later in the text.

In order to provide the most accurate simulation results as possible, the simulated channeling efficiency values were directly computed by using the CRYSTAL simulation code through the calculation of channeled (under-barrier) particles population. The deflection efficiency obtained through the fitting of simulated beam profiles is nearly the same calculated directly counting the number of under-barrier particles for $R/R_{cr} < 20$, determining the goodness of the fitting procedure (4.2-4.5) to estimate the deflection efficiency. The limitation of this procedure in the range $R/R_{cr} > 20$ is connected with the overlap of

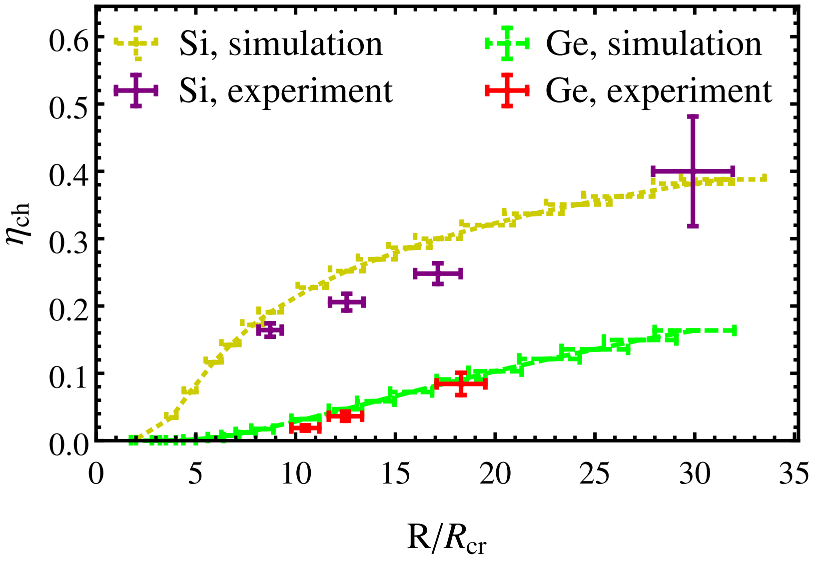

Figure 4.5: The experimental and simulated depedences of channeling efficiency of Si and Ge crystals at optimal channeling orientation on the ratio of the bending radius to its critical value.

the channeling and over-barrier peaks in the deflected beam profile for too high bending radii as explained later in the text.

The experimental results were critically compared to CRYSTAL simulations, highlighting a good agreement between them. The dependence of the channeling deflection efficiency on the ratio R/R_{cr} is shown in Fig. 4.5 for both experimental and simulation results. The errors on the experimental efficiencies are due to the fitting error with an additional uncertainty connected with the normalization procedure. On the other hand, the x-error of simulated results is connected with the uncertainty of the crystal length, while the small y-error is due to statistics. Table 4.1 displays all values of the curvature radii, bending angles, θ_b, and channeling efficiency used in the experiment; Table 4.2 represents

Table 4.1: Measured Si and Ge crystal bending radia, angles and channeling efficiency.

Material	θ_b (μrad)	$\frac{R}{R_{cr}}$	θ_{VR} (μrad)	η_{ch}
Si	315	29.9	224	0.40 ± 0.08
Si	550	17.1	204	0.248 ± 0.016
Si	750	12.6	194	0.206 ± 0.013
Si	1080	8.72	183	0.165 ± 0.010
Ge	820	18.3	172	0.084 ± 0.017
Ge	1200	12.5	165	0.036 ± 0.007
Ge	1430	10.4	162	0.019 ± 0.004

Table 4.2: Simulated Si and Ge crystal bending radia, angles and channeling efficiency.

Material	θ_b (μrad)	$\frac{R}{R_{cr}}$	θ_{VR} (μrad)	η_{ch}
Si	315	29.9	235	0.3818 ± 0.0004
Si	550	17.1	203	0.3000 ± 0.0004
Si	750	12.6	190	0.2519 ± 0.0003
Si	1080	8.72	182	0.1907 ± 0.0003
Ge	820	18.3	178	0.0909 ± 0.0002
Ge	1200	12.5	161	0.0468 ± 0.0002
Ge	1430	10.4	156	0.0320 ± 0.0002

the same results obtained with simulations. As expected, the dependence of channeling efficiency is monotonic [13], since the potential well depth decreases while R becomes smaller.

The experimental results highlighted a channeling efficiency larger than 35 % for silicon in agreement with simulations. Through the fitting procedure (4.2-4.5) it was not possible to extract the dechanneling length for silicon in the case $R/R_{cr} > 20$, while the channeling efficiency values was found with very large errors as explained later in the text. The experimental error is rather high for the curvature of $\theta_b = 315$ μrad, because channeling and volume reflection peaks are very close, and it is difficult to distinguish the channeling fraction. By this reason, the angular distance between the channeling and volume reflection peaks is the main restriction of the fit (4.2-4.5). Nevertheless, it is clear from Fig. 4.4 upper left that high-efficiencies as those in this paper have never been achieved so far for electrons.

On the other hand, channeling efficiency for germanium achieves 8 % at the lowest experimental bending angle. This is indeed the first evidence of negative beam deflection via channeling in a bent Ge crystal.

Although, channeling efficiency for germanium is much lower than for silicon, this effect should not be attributed to the quality of the crystal, because both germanium and silicon crystals were manufactured through the same procedures leading to high performance of both crystals at much higher energy [16–18]. The only reason for such a difference owes to the influence of Coulomb scattering, which is about 2.2 times stronger for Ge than for Si. Indeed, this angle can be roughly estimated by multiple scattering formula [94]:

$$\theta_{sc} = \frac{13.6\text{MeV}}{pv}\sqrt{l_{cr}/X_{rad}}[1 + 0.038\ln(l_{cr}/X_{rad})], \tag{4.6}$$

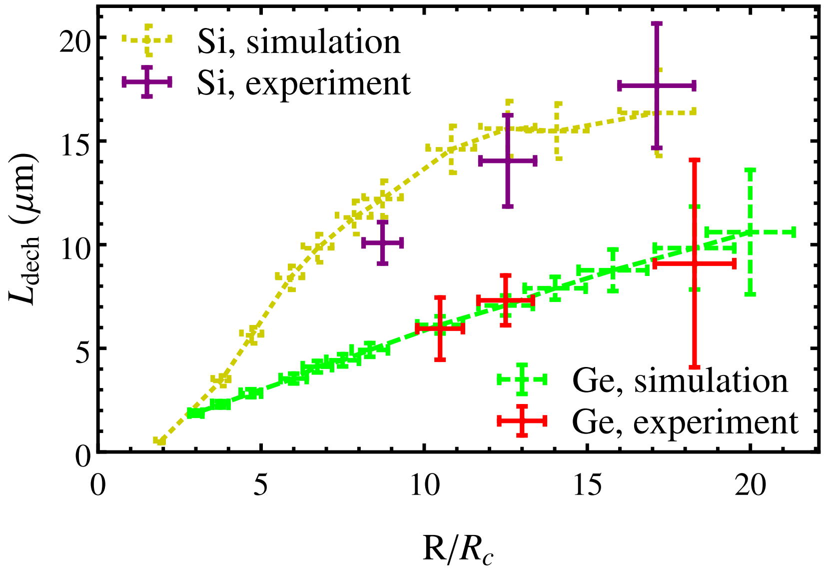

Figure 4.6: The experimental and simulated dependence of the dechanneling length on the ratio of the bending radius to its critical value at ideal channeling orientation. The dechanneling length for the first silicon curvature of $\theta_b = 315$ μrad, was not extracted because channeling and volume reflection peaks were too close, thus making the fit (4.2-4.5) practically inapplicable.

where X_{rad} is the radiation length, l_{cr} the crystal length along the beam direction. By substituting the crystal parameters into (4.6), one obtains the estimated multiple scattering angles for silicon and germanium crystals, being 130 μrad and 290 μrad, respectively. While the first value is 1.8 less than the Lindhard angle, the second one is of the same order. This fact explains our choice of ultra-thin crystals (15 μm), otherwise multiple scattering would cover all the coherent effects, leading to the impossibility to measure neither channeling or VR.

To complete the analysis on channeling, one should evaluate the main parameter that determines the steering capability of a crystal through the dechanneling length. Such parameter has been extracted by using the fit (4.2-4.5) of both experimental and simulated deflection distributions. The dependences of extracted dechanneling length on the ratio of bending radius and critical radius for both silicon and germanium are shown in Fig. 4.6. The corresponding experimental and simulation values are listed in Table 4.3.

As for channeling efficiency, the measured dechanneling length depends monotonically on the crystal radius in agreement with simulations. The silicon dechanneling length is comparable with the length of the crystal, while for germanium being at least 1.5–3 times less. This fact explains the difference in channeling efficiency between the two materials, being due to the different multiple scattering contribution for different atomic number Z.

The present data demonstrate that negative particles steering efficiency is

Table 4.3: Experimental ($L_{dech\ \mathrm{Exp}}$) and simulated (both from distribution ($L_{dech\ \mathrm{Sim}}$) and directly from the dependence of channeling efficiency on the penetration depth ($L_{dech\ \mathrm{DSim}}$) as well as from the same dependence excluding overbarrier particles captured under the channeling mode and then dechanneled ($L'_{dech\ \mathrm{DSim}}$) Si and Ge dechanneling lengths. All dechanneling lengths are measured in μm.

	$\frac{R}{R_{cr}}$	$L_{dech\ \mathrm{Exp}}$	$L_{dech\ \mathrm{Sim}}$	$L_{dech\ \mathrm{DSim}}$	$L'_{dech\ \mathrm{DSim}}$
Si	17.1	17.7 ± 3.0	16.4 ± 2.1	18.96 ± 0.05	21.14 ± 0.10
Si	12.6	14.0 ± 2.2	15.6 ± 1.4	16.48 ± 0.05	18.05 ± 0.07
Si	8.72	10.1 ± 1.0	12.2 ± 0.9	13.62 ± 0.05	14.73 ± 0.06
Ge	18.3	9 ± 5	10 ± 2	7.97 ± 0.07	8.95 ± 0.26
Ge	12.5	7.3 ± 1.2	7.1 ± 0.5	6.02 ± 0.03	6.46 ± 0.11
Ge	10.4	5.9 ± 1.5	6.1 ± 0.4	5.29 ± 0.03	5.58 ± 0.09

mainly regulated by dechanneling length and not by the channeling well depth that would have benefit Germanium. It is worth to note that this is a peculiar feature of negative particles since for positive ones, the influence of the potential well depth dominates the dechanneling process, and once Ge and Si efficiency for short crystal are compared, Ge performances prevail on Si [16–18]. This insight into the channeling performances by changing the atomic number suggests that low scattering materials such as diamond could be an interesting candidate to be investigated to improve the steering efficiency.

Given the good agreement between experiments and simulations, we may exploit the latter to investigate deeply the dechanneling process. In particular, one may separate the different contributions on the dechanneling distribution (10), between the VR and channeling peaks. In fact, already in [29] it was demonstrated that the rechanneling process (capture under channeling of dechanneled particles, see section 2) may have a strong influence on the dechanneling length. Here we investigate also the contribution of overbarrier particles to the dechanneling distribution. Fig. 4.7 displays different fractions in the angular distributions obtained directly from simulations (solid), namely channeling, dechanneling with taking into account rechanneling as well as the volume reflection/overbarrier fraction for both silicon (a) and germanium (b). For comparison the same fractions were extracted from the angular distributions by using the fit (4.2-4.5) (dashed).

Fig. 4.7 highlights a contribution of initially overbarrier particles, that can be captured and dechanneled from the channeling mode several times (marked in Fig. 4.7 as rechanneled ovebarrier). In a bent crystal, the contribution of

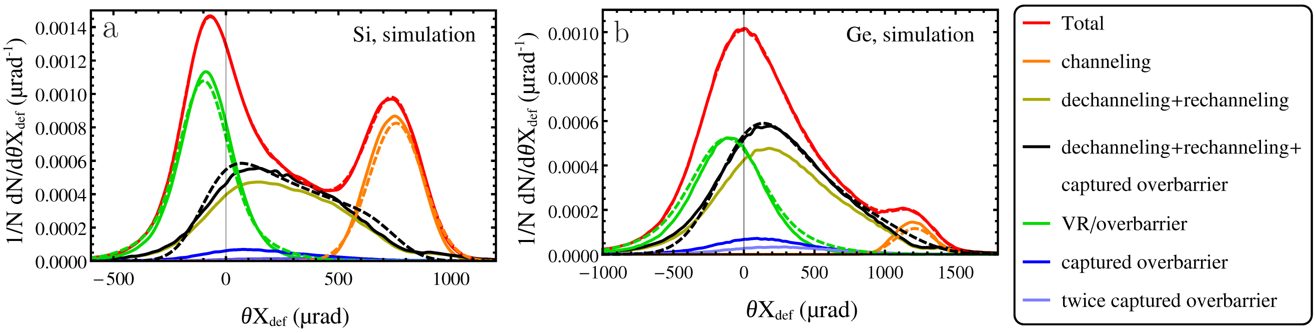

Figure 4.7: Simulated distributions of deflected beam by Si (left) and Ge (right) crystals, bent at 750 μrad and 1200 μrad respectively, and the channeling, dechanneling, initially overbarrier, overbarrier, captured under and escaped the channeling mode one and two times (captured overbarrier) and the sum of captured overbarrier and dechanneling fractions. Dashed curves represent the total, channeling, overbarrier and dechanneling fractions, obtained by means of the fit (4.2-4.5).

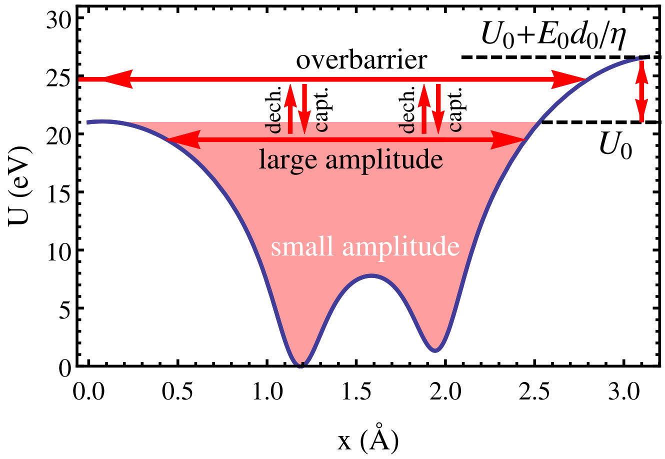

Figure 4.8: Interplanar potential of (111) Si for maximal bending radius (4.76 cm) used in the experiment. Overbarrier marks initially overbarrier fraction of particles that can be captured into the channeling mode or rechaneled (rech.) and dechanneled (capt.) once or several times.

overbarrier particle cannot be eliminated, even considering a parallel beam. Indeed, due to the asymmetry in the potential barrier introduced by the bending, particles approaching with zero transverse kinetic energy to the right potential barrier are reflected to the left, gaining a non-zero transverse kinetic energy. A sketch of initially overbarrier particles is depicted in Fig. 4.8; such particles follow the bent crystal planes and can be deflected to a considerable angle.

The solid black line in Fig. 4.7 represents the contribution of dechanneled and rechanneled particles with the contribution of captured overbarrier particles. If compared with the dotted solid black line, representing the result of the fit (4.2-4.5), it is clear that from the experimental deflection distribution is not possible to extract a dechanneling length correspondent to only initially

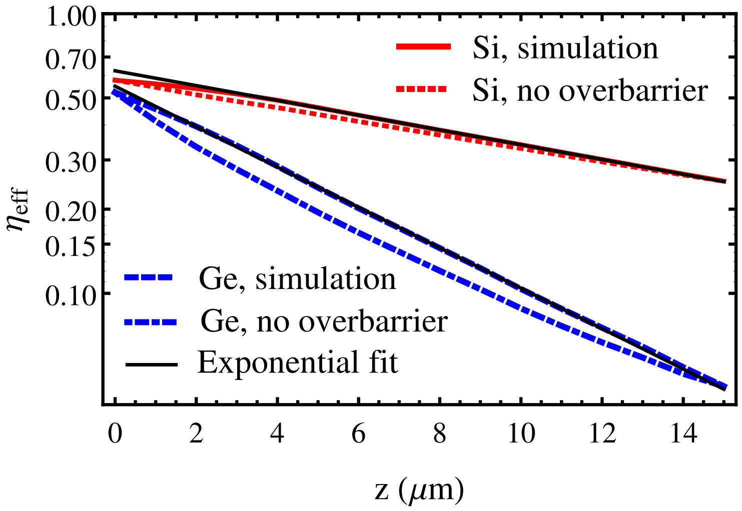

Figure 4.9: Exponential fit of the depedence of the channeling efficiency in the penetration depth in Si and Ge crystals with the same parameters as in Fig. 4.7 and the same dependences without the overbarrier particles, captured under and escaped the channeling mode.

channeled particles. By this reason the fit [14, 31] was modified to (4.2-4.5).

To highlight deeply the contribution of captured overbarrier particles, channeling efficiency was also simulated in a dependence on the penetration depth z, taking (solid) and not taking (dashed) into account this contribution for both Si (red) and Ge (blue) crystals as shown in Fig. 4.9. By using an exponential fit (4.1) the values of dechanneling length were extracted (see Table 4.3, $L_{dech\ DSim}$ and $L'_{dech\ DSim}$, for the cases with and without captured overbarriers, respectively). The values $L_{dech\ DSim}$ differ from the extracted ones from experimental and simulated angular distributions, no more than on $\sim$ 1–2 μm, lying usually within the frame of the error.

On the contrary, the simulated dechanneling length without the contribution of captured overbarrier particles, $L'_{dech\ DSim}$, (see Table 4.3), exceed $L_{dech\ DSim}$ by 5–10%. In other words, the initially overbarrier particles decrease the total dechanneling length by several percent because can usually be captured slightly below the potential well barrier, as shown in Fig. 4.8. Since these large amplitute particles dechannel faster, the dechanneling length of these particles is lower than for the stable ones. Consequently, the capture of initially overbarrier particles reduce the total measured dechanneling length. Furthermore, even if these values were obtained in the same way as $L_{dech\ DSim}$, the depedence of $L'_{dech\ DSim}$ on the penetration depth evidently differ from the exponent function. Indeed, one has to remember that the dechanneling of negative particles is mainly due to strong scattering with nuclei that has an intrinsic non-slow diffusive nature [98].

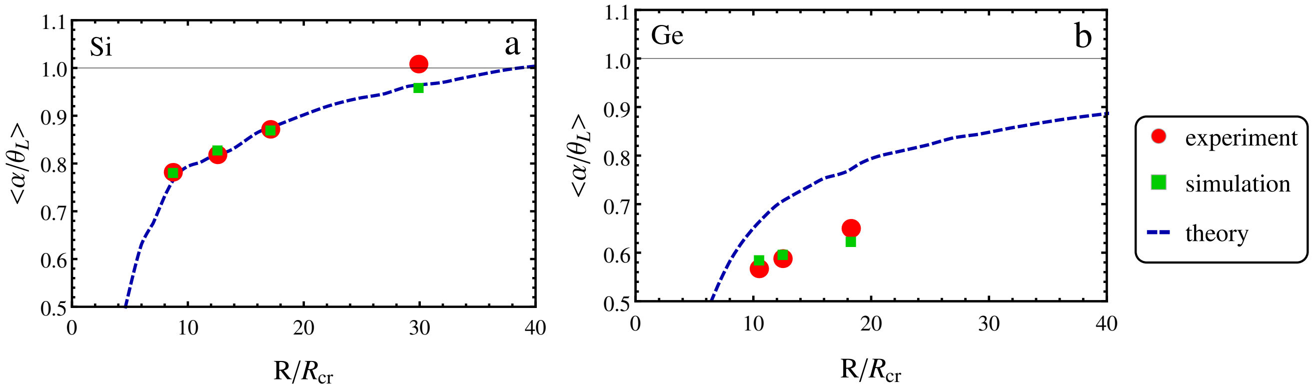

Figure 4.10: Theoretical, experimental and simulated dependence of the maximal value of volume reflection peak position w.r.t. the Lindhard angle on the bending radius w.r.t. its critical value for both Si and Ge (111) bent crystals.

The relative difference between $L'_{dech\ DSim}$ and $L_{dech\ DSim}$ increases with crystal radius rise. This is explained by decreasing of the difference $E_0 d_0/\eta$ ($\eta = R/R_{cr}$, see chapter 3) between the right and left potential barriers. Consequently such overbarrier particles are closer to the potential boundary. This means that such particles will remain near the potential barrier for a longer distance due to low transverse velocities, having the influence on the total dechannelling length also for a longer distance at higher radius values. Therefore, initially ovebarrier particles, captured under channeling mode and then dechanneled, can make a several percent contribution into dechanneling length value.

Finally, we also investigated the other mechanism of beam deflection, i.e., the VR. In particular we studied VR deflection angle vs. the curvature radius, while comparing to the maximal angle expected from the theory (3.1-3.2).

In order to verify the theoretical dependence of the maximal angle of VR on R (see Eqs. 3.1-3.2), we used the experimental and simulated values for the modules of a maximal VR angle (determined by gaussian fit) comparing them in Fig. 4.10. For channeling deflection angle, the agreement between theory and both experimental and simulated results is very good for silicon, while being worse for germanium. This fact is explained again by the contribution of multiple scattering of non-volume reflected particles, allocated around 0 angle (see Figs. 4.3, 4.4), that shifts the volume reflection peak center towards 0 on the angular distribution. Multiple scattering has a much stronger influence for germanium, for which its r.m.s. angle is 2.2 times higher than for silicon. By this reason the measured maximum VR for silicon of 235 μrad is about θ_L angle for silicon (in agreement with previous experiments [29, 30]), while it is only $0.6\theta_L$ for germanium, being equal to 178 μrad.

4.5 Conclusions

An experiment on beam steering of 855 MeV electrons by using 15 μm bent silicon and germanium crystals has been carried out at the Mainzer Mikrotron. Through the exploitation of an innovative piezo-actuated mechanical bender, it was possible to test planar channeling and volume reflection for several radii of curvature.

Experimental results, in agreement with Monte Carlo simulation, demonstrated that maximum channeling efficiency were about 40% and 8 % for silicon and germanium, respectively. The difference between these two materials has to be ascribed to the higher atomic number Z for Ge, which results in a higher Coulomb scattering contribution, causing stronger dechanneling. Indeed, the main parameter of planar channeling, i.e., the dechanneling length was also measured, resulting to be close to the crystal length for Si, but 2 times shorter for the Ge crystal at the largest bending radius. In particular, the usage of a Si crystal with the length comparable to the dechanneling length permitted an unprecedented level of steering efficiency for an electron beam.

On the other hand, it is important to remark that any measurements of a negatively charged beam steering in a germanium bent crystal at the energies lower than hundreds of GeV have never been done before, due to the lack of properly designed crystals, i.e. with a length of the order of the dechanneling length. Therefore, the evidence of beam steering of sub-GeV electrons in a Ge crystal was demonstrated for the first time.

The influence of initially non-channeled particles on the dechanneling processes, which causes a reduction of the dechanneling length in case the crystal thicknesses are comparable with the dechanneling length, was also highlighted.

Finally, the dependence of the ratio between the volume reflection angle and the Lindhard angle vs. the R/R_{cr} (see Eq. (3.1-3.2)) was investigated, demonstrating that it does not depend on the energy, being very useful to make prediction at different energies.

The presented results, in particular the studies of beam efficiency and dechanneling length vs. the crystal curvature and atomic number, are of interest for application, such as generation of e.m. radiation in higher Z-materials bent and periodically bent crystals. Given the good agreement with Monte Carlo simulation, one may also think to apply the presented approach to extrapolate information on charged particle steering at higher energies, for instance to investigate the possibility of crystal-based collimation/extraction at current and future electrons accelerators.

CHAPTER 5

PLANAR CHANNELING AND QUASICHANNELING OSCILLATIONS IN THE DEFLECTION ANGLE DISTRIBUTION

As has been already mentioned above, interplanar electric field induces harmonic-like transverse oscillations. These oscillations are called *planar channeling oscillations*, which correspond to an *under-barrier* motion along the crystal planes.

Planar channeling oscillations at low energies in backscattering were predicted by J.H. Barrett [134, 135] in simulations. Later they were observed in several experiments with a straight crystal [136–142] with ion beams of the energy of the order of MeV and well described in [57, 60].

In this chapter a new effect, connected with planar channeling oscillations at high energies is predicted [A3, A4]. Namely, the planar channeling oscillations in a bent crystal are transformed at certain conditions into series of equidistant peaks, called dechanneling peaks. In other words, the way of direct observation of planar channeling oscillations in a bent crystal at high energies is suggested.

Moreover a new kind of oscillations in the deflection angle distribution, strictly related to the motion of over-barrier particles, i.e. quasichanneled particles, is predicted [A4]. Such oscillations, named planar quasichanneling oscillations, possess a different nature than channeling oscillations. It is shown that channeling oscillations can be observed only for positive particles while quasichanneling oscillations can exist for particles with either sign. The conditions for experimental observation of channeling and quasichanneling oscillations at existing accelerators with available crystal are found and optimized. Finally, the experimental observation of quasichanneling oscillations is reported [A6].

5.1 Planar channeling oscillations in the deflection angle distribution

An example of dechanneling peaks, corresponding to the planar channeling oscillations in the angular distribution of particles passed through the crystal, is shown in Fig. 5.1 for (110) planes. This result was obtained by simulations with the CRYSTAL code.

The origin of the dechanneling peaks consists in a high-phase correlation

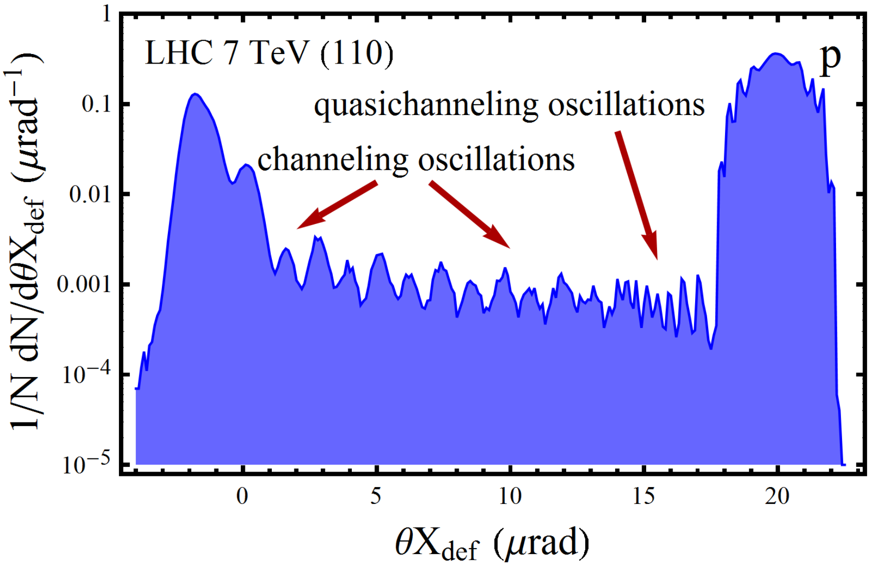

Figure 5.1: Angular distribution of the 7 TeV proton beam after interaction with the silicon crystal at the channeling orientation. The simulation layout is: r.m.s. beam angular divergence $\theta_{in} = 0.5\mu rad$, crystal length $l_{cr} = 2mm$, bending angle $\theta_b = 20\mu rad$, (110) planes.

of trajectories of different particles, dechanneling close to the atomic planes where the nuclear density is high. Note that the number of dechanneling peaks corresponds to the number of particle approaches to a crystal plane where the probability of scattering is high. In other words, the dechanneling peak number in Fig. 5.1 is equal to the number of channeling half oscillations. In particular, particles entering the crystal near the left (right) side of a channel, bent to the right, are dechanneled after even (odd) number of half oscillations.

For positive particles, the oscillation length is nearly the same for most of particles with the same energy and different amplitudes of channeling oscillations. This gives rise to *phase correlation* of different trajectories. Depending on the difference in the oscillation lengths, such correlation can be conserved for several or, at certain conditions, even several tens of oscillations.

The channeling oscillation length can be evaluated directly by integration of the equation of motion. Examples of the dependence of this length on the coordinate of the left turning point of the trajectory are shown in Fig. 5.2. The corresponding potential wells are also drown in Fig. 5.2. Note that the particles dechannel with high probability only near the lower potential maximum, to which the particles approach closer as shown in Fig. 5.2.

Let us determine the dechanneling zone as an energy range limited by the potential energy values in the following points. The first point is the left potential maximum of a channel bent to the right. The other one is to the right from this maximum at the distance of one amplitude of atomic thermal vibra-

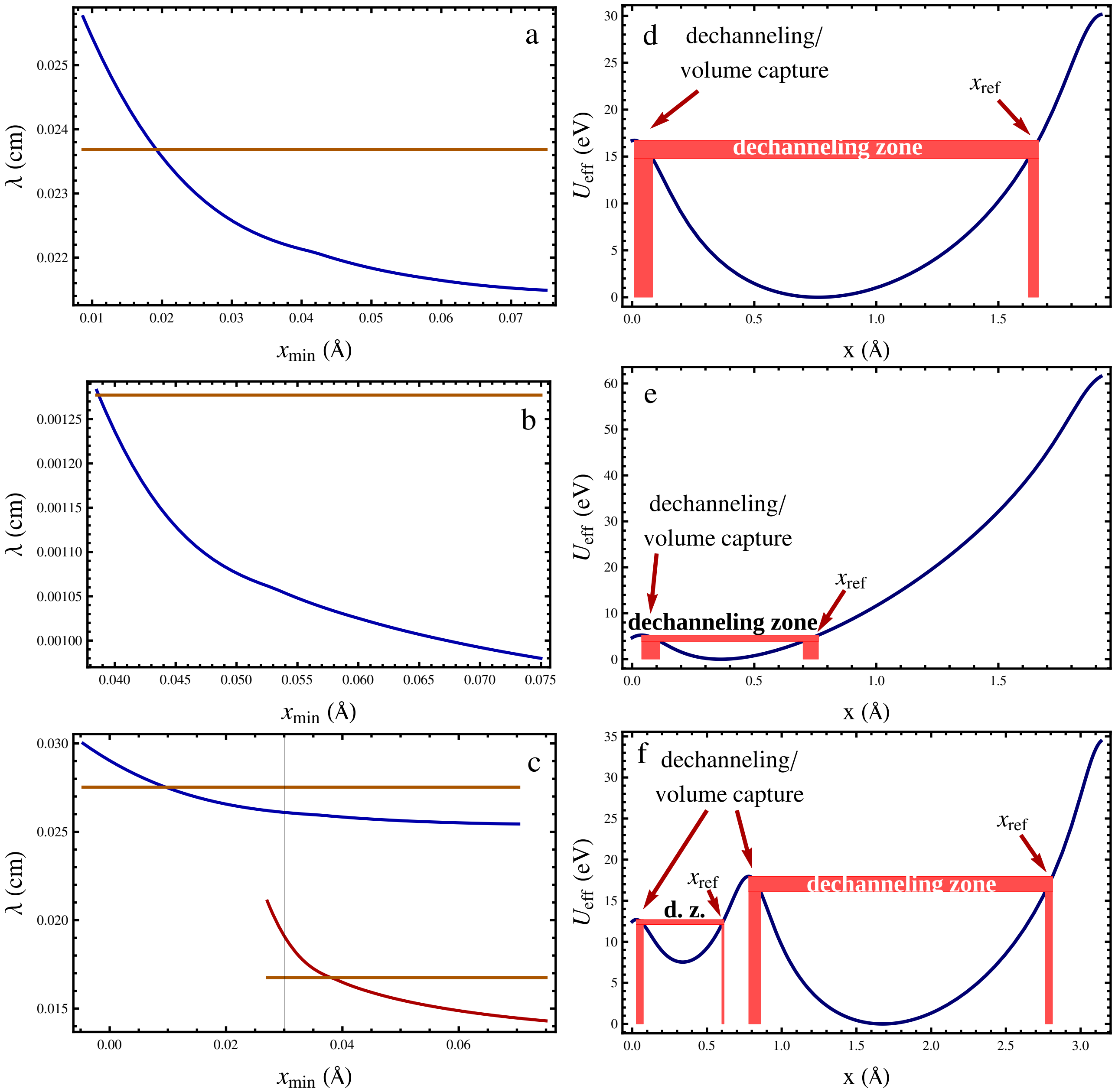

Figure 5.2: The channeling oscillation length *vs* the left turning point of the trajectory (left column) and the corresponding potential wells (right column) in a bent crystals: a,d: 7 TeV protons, $l_{cr} = 2mm$, $\theta_b = 20\mu rad$, (110) planes; b,e: 20.35 GeV positrons, $l_{cr} = 0.11mm$, $\theta_b = 1600\mu rad$, (110) planes; c,f: 7 TeV protons, $l_{cr} = 2mm$, $\theta_b = 20\mu rad$, (111) planes. Larger channeling oscillation length corresponds to the wider potential well. Horizontal lines correspond to the channeling length estimation by (1.29). The left point placed at x=0 indicates the coordinate of the crystal plane.

tions (0.075 Å for Si at room temperature [57]) from the nearest crystal plane (see Fig. 5.2). In the space of transverse coordinates the dechanneling zone covers the extreme points of particle trajectories with transverse energies in the interval defined above.

It is important to underline that dechanneling effect implies two stages: exceeding of the critical value of the transverse energy and consequent escape from the channel. Hereinafter, the dechanneling point and probability of dechanneling mean scattering of a particle, leading to the transverse energy rise, i.e. the first stage of dechanneling. Consequently, if such particle is deflected toward the center of the channel it will pass another oscillation length before the escape.

It is shown in Fig. 5.2 that indeed the channeling oscillation length varies rather weakly in the dechanneling zone and Eq. (1.29) can be applied. Consequently there is a phase correlation of different trajectories for positive particles in the dechanneling zone. Thus, such particles dechannel almost at the same depths modulo $\lambda/2$.

The decrease of the ratio of the crystal bending radius to its critical value R/R_{cr} reduces the phase correlation of the trajectories, resulting in deterioration of the structure of dechanneling peaks as will be shown below. The length estimated by Eq. (1.29) becomes a bit overestimated at small radii of curvature (see Fig. 5.2b). This results in a higher number of dechanneling peaks.

The channeling oscillation length in Fig. 5.2 is proportional to $\sqrt{pv}$ (like in the formula (1.29)) for fixed form of the potential well and fixed value of the transverse energy. Thereby, phase correlation should take place at different lengths for different energies of positive particles.

For the negative particles, the interplanar potential $U(x)$ becomes inverted, resulting in the atomic plane being in the channel center. Thus, the dechanneling zone includes all the amplitudes of oscillations. Depending on the amplitude, the channeling oscillation length can differ several times as is shown in Fig. 5.3. In addition, electrons cross crystal planes in the middle of the channel when their angle θ_x is maximal in magnitude [89]. Positrons, on the opposite, approach the planes at the minimal angle values. Consequently the transverse energy change $\Delta\epsilon$ for electrons is proportional to the scattering angle ϑ_x while for positrons to its square ϑ_x^2 [89]:

$$\Delta\epsilon = pv\theta_x\vartheta_x + pv\frac{\vartheta_x^2}{2} \rightarrow \begin{cases} pv\theta_x\vartheta_x, & \text{if } \theta_x \rightarrow \theta_{xmax}; \\ pv\frac{\vartheta_x^2}{2}, & \text{if } \theta_x \rightarrow 0. \end{cases} \tag{5.1}$$

Thereby, the amplitude of electron oscillations due to scattering changes more for electrons than for positrons. Thus, any phase correlation will quickly

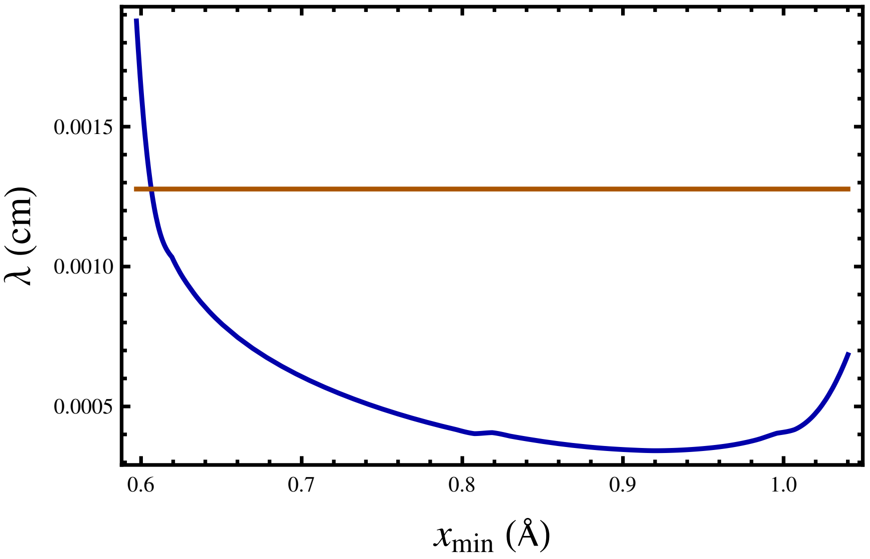

Figure 5.3: Channeling oscillation length for 20.35GeV electrons, $l_{cr} = 0.11mm$, $\theta_b = 1600\mu rad$, (110) planes.

disappear and the planar channeling oscillations for electrons will not be observable in the angular distribution.

It is also important to explain why the pattern of peaks is a sequence of a high peak followed by a lower one (see Fig. 5.1). This is explained by an asymmetry of the potential well displayed in Fig. 5.2. In particular, in the space of transverse coordinates the dechanneling zone close to the left side of the potential is wider than the zone near the opposite reflection point. Indeed, if one takes the dechanneling zone width to be equal to the thermal vibration amplitude (0.075 Å for (110) silicon crystal planes), one obtains the corresponding potential energy difference $\Delta U \sim 2$ eV. Its value as well as the dechanneling zone width does not considerably change for different crystal bending and beam energies. In contrast, the width of the zone near the reflection point x_{ref} (see Fig. 5.2) strongly depends on the crystal bending:

$$\Delta x \approx \Delta U / U'_{eff}(x_{ref}). \tag{5.2}$$

Through the use of the numerical parameters of the potential in Fig. 5.2d, one obtains $\Delta x = 0.042$ Å, which is almost two times less than the thermal vibration amplitude. This ratio explains the alternation of high and low peaks.

Planar channeling oscillations can also be observed for (111) crystal planes. The main contribution here is due to the wider channel because the dechanneling zone introduced above is considerably narrower for the small channel as is shown in Fig. 5.2f. This is because a potential maximum and a crystal plane do not coincide due to both the centrifugal force influence and non-equidistance of (111) crystal planes. Therefore, the distance between the potential maximum and the nearest crystal plane is less at the left side of the small channel than

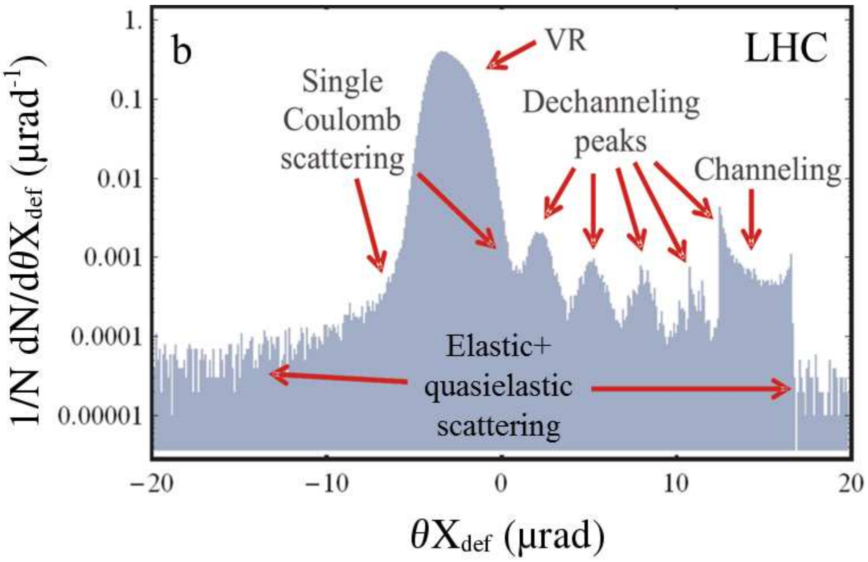

Figure 5.4: The angular distribution of 7 TeV protons behind the (110) bent crystal of 4 mm length and 50 μrad bending angle and volume reflection orientation is -35 μrad (b).

of the large one. The channeling oscillation length varies strongly in the case of the small channel, causing smearing of phase correlations. The oscillation length value is also smaller for the small channel than for the larger one. This causes reduction of the distance between the peaks, resulting in complicated detection. Thereby, only the planar channeling oscillations in the wider channels will be practically observable.

The appearance of dechanneling peaks is also possible for volume-captured particles (see Fig. 5.1b). when the orientation of volume reflection [A3, A4] is set up. In this case, the lower peaks will completely disappear because a particle can be captured with a high probability only near the left potential maximum due to the asymmetry of the potential well (see Fig. 5.2 and 1.13). It results in a good phase correlation of transverse motion of volume captured particles, even better than for the channeling orientation. For this reason, the spacing between the peaks corresponds to one channeling oscillation length for the volume reflection orientation.

The dechanneling peaks may be observed if the inter-peak angular distance $\Delta\varphi_{ch}$ exceeds the doubled incoherent scattering angle θ_{sc} [A3]:

$$\frac{\Delta\varphi_{ch}}{2\theta_{sc}} = \frac{\lambda\theta_b}{4l_{cr}} \frac{pv\sqrt{\frac{X_r}{l_{cr}}}}{13.6MeV\left(1+0.038\ln\left(\frac{l_{cr}}{X_r}\right)\right)} > 1, \tag{5.3}$$

where l_{cr} and θ_b are the crystal length and bending angle, respectively, X_r is the radiation length equal to 9.36 cm for silicon. The Coulomb scattering angle was estimated according to [94]. For the volume reflection orientation this condition will be twice softer because half of the peaks will not appear as mentioned above. Thus, volume-reflection orientation provides a still better conditions than that for channeling.

Another important condition is the crystal bending radius R to be larger than the critical one, R_{cr} [62]:

$$\frac{R}{R_{cr}} > 1. \tag{5.4}$$

As mentioned above, this is the condition for the channeling to occur in a bent crystal [5, 62].

The third important condition is the angular divergence of the incident beam should not be greater than half of the critical channeling angle θ_L.

$$\theta_{in\ r.m.s.} < \theta_L/2. \tag{5.5}$$

Indeed, the angular divergence, approaching the critical angle, results in a considerable oscillation phase shift. Such trajectories are, of course, uncorrelated. This concerns both channeling and volume reflection orientations.

Some sort of scaling of the channeling oscillation picture with energy can readily be introduced. Such a scaling can be assured by the conservation of both the peak number:

$$n_{peaks} = \frac{2l_{cr}}{\lambda} = Const; \tag{5.6}$$

and of the ratio of the inter-peak interval to the Coulomb scattering angle:

$$\frac{\Delta\varphi_{ch}}{2\theta_{sc}} = Const. \tag{5.7}$$

By substituting Eq. (1.29) into (5.6) one obtains:

$$l_{cr} \sim \sqrt{pv}. \tag{5.8}$$

Substituting further Eq. (5.3) into (5.7), using (5.8) and neglecting the logarithmic factor one obtains that:

$$\theta_b \sim 1/(pv)^{3/4}. \tag{5.9}$$

Finally the bending radius scaling can be simply obtained from Eqs. (5.8) and (5.9):

$$R \sim (pv)^{5/4}. \tag{5.10}$$

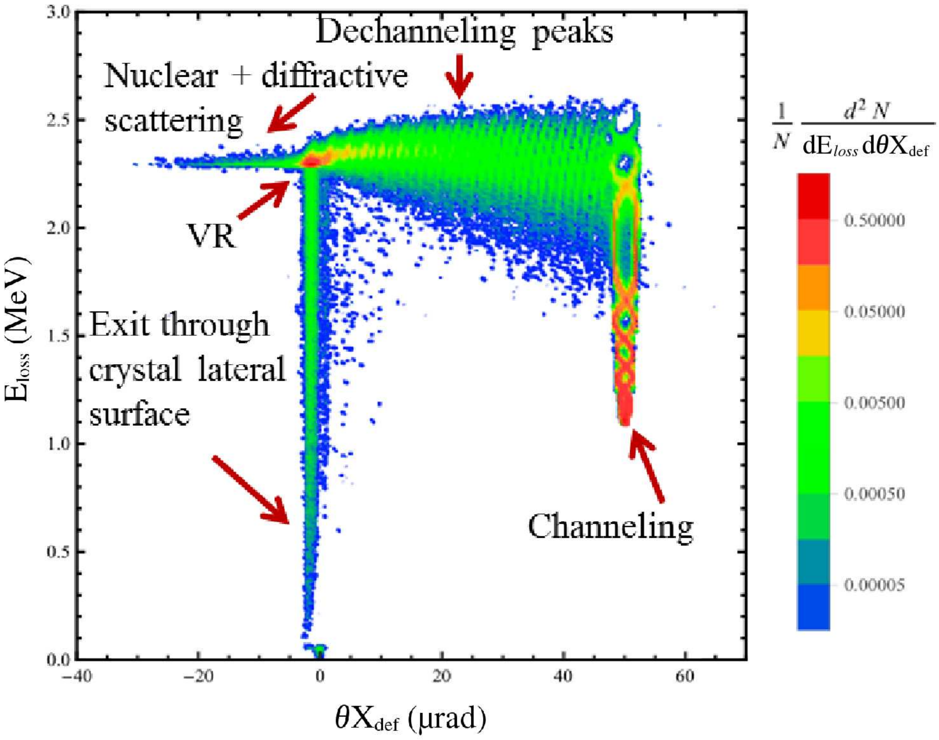

Figure 5.5: Ionization losses map at channeling orientation of the (110) crystal.

5.2 Ionization energy losses

The planar channeling oscillations can be revealed not only in the angular distributions but also in ionization losses map. An example of such a map (particles distribution on both deflection angles and energy losses E_{loss}) at the channeling orientation for the (110) crystal at 7 Tev is shown in Fig. 5.2. Indeed, the “waves” at the dechanneling zone represent dechanneling peaks.

However one can observe in Fig. 5.2 another effect. Namely, the channeled particles with high amplitude of oscillations can lose even more energy than in the amorphous silicon. This is because the particles spend considerable time before dechanneling near crystal planes where the electron density is much higher than the electron density of the crystal as it is illustrated in Fig. 5.2. Thus, the electron density averaged along the trajectory will be higher than its average value in the crystal, since the ionization losses are considerably higher near the crystal plane than in the center of a channel. These particles dechannel fast as a consequence.

The trajectory correlations are presented not only for planar channeling oscillations. The loop-like picture for the channeled particles is explained by the different number of channeling oscillations as well as by the different level of ionization losses depending on the oscillation amplitude.

The effect of excess of the ionization losses over the amorphous level was

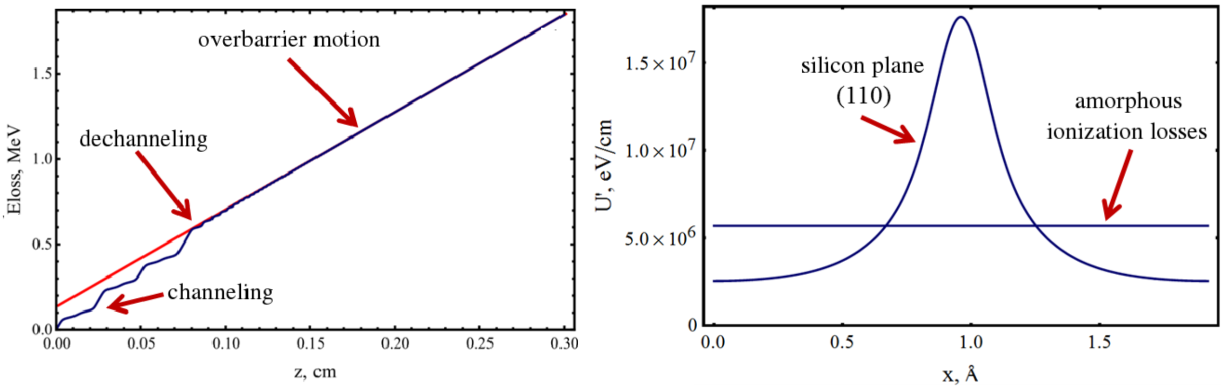

Figure 5.6: Ionization losses along a trajectory of a dechanneling particle (left) and depending on the transverse coordinate (right).

observed before [143–145] only for the (111) atomic planes. This naturally exerts an excess of the electron density over the average level in a crystal simply due to the proximity of the (111) planes grouped in closely spaced pairs.

5.3 Planar quasichanneling oscillations in the deflection angle distribution

Planar channeling oscillations in backscattering experiments at low energy were observed [136–142] while they have not been observed yet at higher energy. However, there is another kind of oscillations not observed before under neither regimes. This kind of oscillations manifests itself as the peaks in the angular distribution which are close to the channeling peak (Fig. 5.1). Hereafter, such new kind of oscillations will be called *planar quasichanneling oscillations in the deflection angle distribution*.

Such oscillations have a different nature than planar channeling oscillations because the distance between them is smaller than the lowest possible half channeling length. In addition, the location of the peaks is almost the same for particles with different charge signs. As we will show below, this indicates the involvement of over-barrier particles.

A qualitative explanation can be obtained from the analysis of the over-barrier trajectories, shown in Fig. 5.7, highlighting the dependence of the particle deflection angles in the laboratory reference system on z:

$$\theta_{Xdef} = \frac{z}{R} - \sqrt{\frac{2(\epsilon - U_{eff}(x(z,\epsilon)))}{pv}}, \tag{5.11}$$

where ϵ is the initial transverse particle energy, x and z the particle transverse and longitudinal coordinates respectively. At $z = l_{cr}$, the first term in Eq.

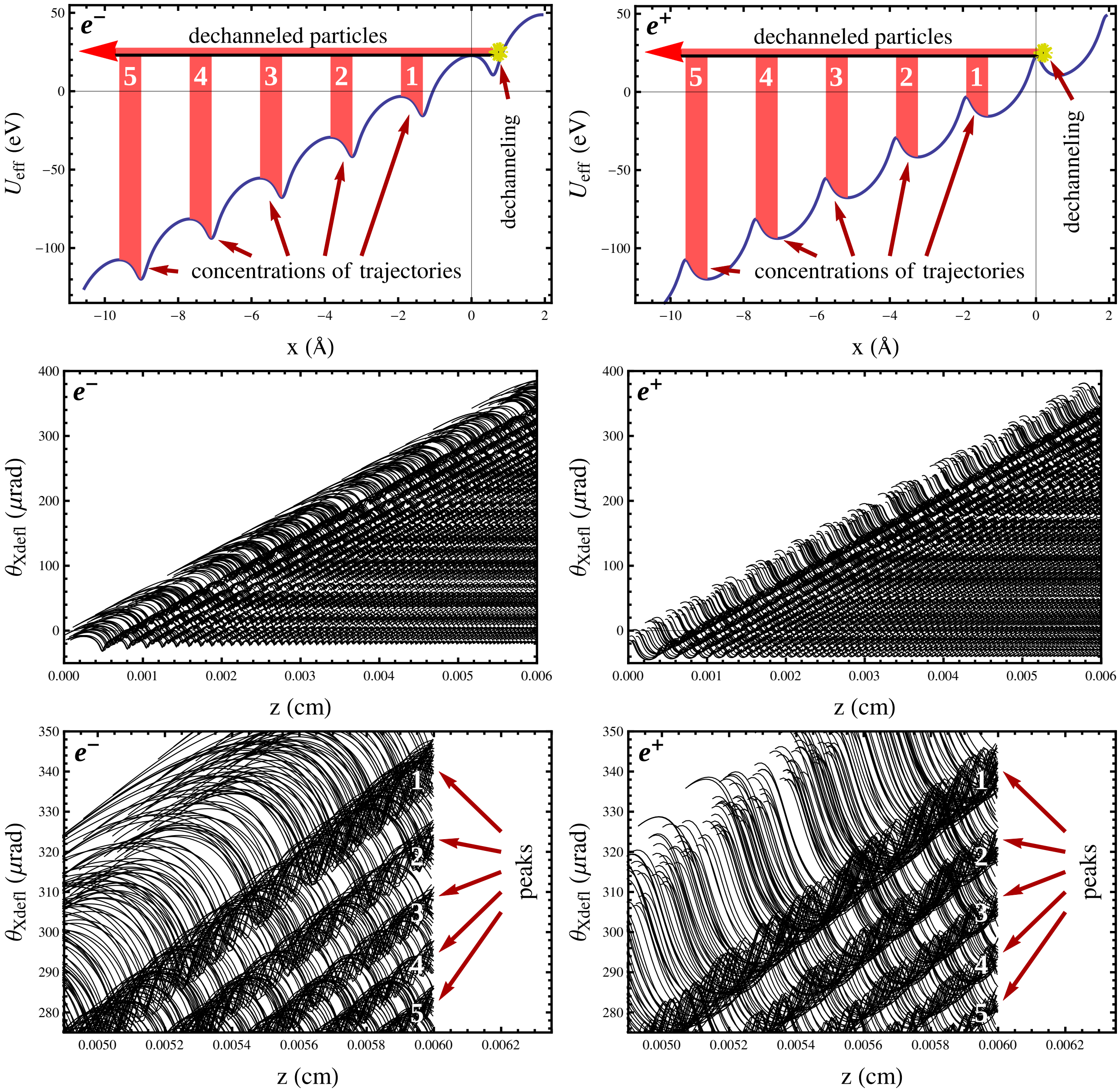

Figure 5.7: The effective potential U_{eff} (top) and the ideal over-barrier trajectories (middle and bottom) (angle (5.11) *vs* longitudinal coordinate) of 20.35 GeV electrons (left column) and for positrons (right column) without scattering. The transverse starting point of trajectories is fixed at $x = 0$, the longitudinal one varies randomly. The transverse energy varies in the range of several eV above the potential barrier at $x = 0$. The crystal parameters are: $l_{cr} = 60\mu rad$, $\theta_b = 400\mu rad$, (110) planes. The longitudinal coordinates in bottom figures are close to the crystal end.

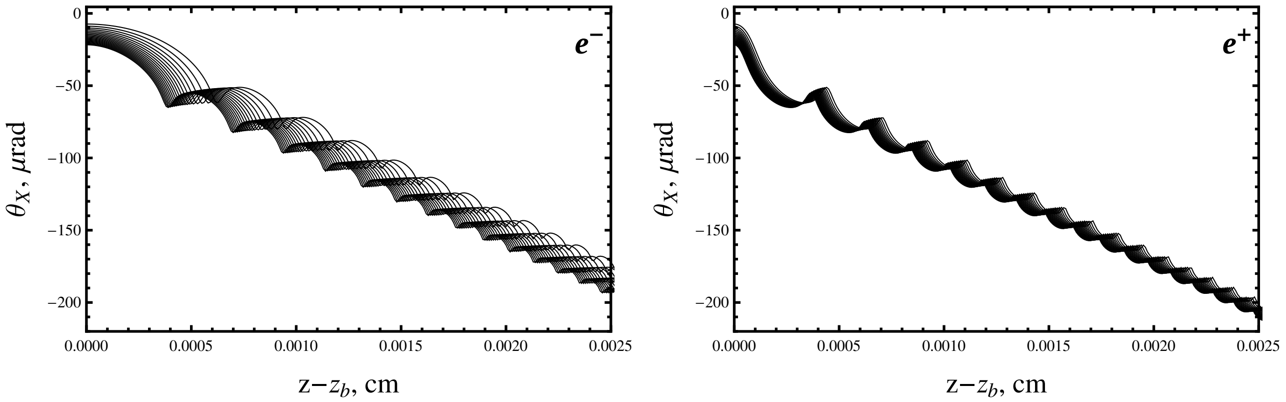

Figure 5.8: Ideal over-barrier trajectories (angle (5.15) *vs* longitudinal coordinate starting at the point of the first potential barrier crossing after dechanneling) of 20.35 GeV electrons (left column) and positrons (right column) in the co-rotating reference system without scattering. All the conditions are the same as in Fig. 5.7.

(5.11) becomes $z/R = \theta_b$ and θ_{Xdef} is the observed particle deflection angle as in Fig. 5.1.

Let us consider the ideal trajectories without any incoherent scattering or energy losses. Also, only dechanneled particles are considered because usually most of the particles initially not captured under channeling state will not achieve the angles close to the channeling direction. Let us also fix the starting point of the over-barrier trajectories in a point above the potential barrier, neighboring the dechanneling point (in Fig. 6 the point is indicated as $x = 0$). Only the longitudinal starting coordinate will be varied randomly. Fig. 5.7 demonstrates that the trajectories tend to group together at certain phases into parallel lines separated by one over-barrier oscillation. Such concentration will generate a new series of peaks in the angular distribution at the crystal exit.

All the lines formed are parallel to the line representing the angle of bending of a crystal plane:

$$\theta_{Xdef} = z/R. \tag{5.12}$$

The main reason for their appearance, is correlation of different over-barrier trajectories even in the first potential well (see Fig. 5.7). These trajectories have almost the same oscillation lengths with the only exception of a small region near the closest barrier to the point of dechanneling. Let us define the n-th oscillation length λ_n of an over-barrier particle as a longitudinal distance passed by this particle traveling between two neighboring potential barriers n and $n+1$, the first of which $U_{eff}(0)$ is the closest to the value of the transverse energy ϵ and $U_{eff}(0) < \epsilon$. Therefore, all the over-barrier trajectories differ only by a starting longitudinal coordinate which varies along a bent crystal plane parallel to the line (5.12) according to Eq. (5.11).

The oscillation length of different trajectories is almost the same by the reason that the main contribution to the quasichanneling peaks is due to dechanneling process. The transverse energy change $\Delta\epsilon$ (Eq. 5.1) is mainly due to soft Coulomb scattering and, therefore, ϵ can exceed the closest potential barrier at most by several eV. The relative change of the n-th over-barrier oscillation length can be calculated by formula:

$$\frac{\Delta\lambda_n}{\lambda_n} = \frac{\Delta\epsilon}{2}\frac{\int_{(n-1)d_0}^{nd_0}\frac{dx}{(\epsilon-U_{eff}(x))^{3/2}}}{\int_{(n-1)d_0}^{nd_0}\frac{dx}{\sqrt{\epsilon-U_{eff}(x)}}}. \tag{5.13}$$

As a rule, this ratio does not exceed $\sim 10\%$ for dechanneled particles. However, this also applies to the particles, initially not captured under the channeling mode but achieved the deflection angle close to the channeling direction. Thereby, they must provide the peaks of quasichanneling oscillations to the same locations as the dechanneled ones.

The location of parallel lines can be found by the condition that the tangent lines $d\theta_{Xdef}/dz$ to the trajectories are parallel to the line (5.12). This condition transforms to:

$$\frac{dU_{eff}}{dx} = 0, \tag{5.14}$$

which implies the locations of local minima and maxima of the potential U_{eff} (see Fig. 5.7). Therefore, the trajectories group between the minima and maxima as shown in Fig. 5.7 because $d\theta_{Xdef}/dz \simeq z/R$.

The same concept can be explained in a different way if one builds a particle trajectory in the co-rotating reference system starting in the point of the first crossing potential barrier z_b after dechanneling represented by:

$$\theta_X = -\sqrt{\frac{2(\epsilon - U_{eff}(x(z-z_b,\epsilon)))}{pv}}. \tag{5.15}$$

An example of such trajectories is shown in Fig. 5.8. These trajectories have a series of oscillations becoming shorter and shorter and tending to the line $(z-z_b)/R$. The oscillations correspond to accelerating ($\frac{d\theta_X}{dz} < 0$) and decelerating phases ($\frac{d\theta_X}{dz} > 0$). The decelerating phases are indicated by red strips in Fig. 5.7).

The particle angular distribution at this crystal exit (like in Fig. 5.1) is given by:

$$\frac{dN}{d\theta_X} = \frac{dN}{dz} \sum_i \frac{1}{|d\theta_X/dz|_i}, \tag{5.16}$$

where the summation bears on the roots z_i of the Eq. (5.15) at the crystal exit. It has asymmetric peaks at $\frac{d\theta_X}{dz} = 0$ corresponding to extrema of U_{eff}. Indeed, when a particle crosses one extremum, it keeps nearly the same angle θ_X for a long distance. By application of the potential values U_{eff} for minima and maxima and using Eq. (5.11), one obtains the equations of two parallel lines which are the boundaries of trajectory concentrations:

$$\begin{aligned} \theta'_{Xdef\ n} &= z/R - \sqrt{\frac{2V_0 n}{pv}}; \\ \theta''_{Xdef\ n} &= z/R - \sqrt{\frac{2(V_0 n + \Delta V)}{pv}}, \end{aligned} \tag{5.17}$$

for the potential maxima and minima respectively. ΔV is the potential energy difference between the neighboring local maximum and minimum while V_0 is the difference between two neighboring maxima of the potential [62]:

$$V_0 = pvd_0/R. \tag{5.18}$$

By substituting Eq. (5.18) in (5.19) and taking into account $z = l_{cr}$ at the crystal exit one finally obtains the location of the bounds containing the peaks of *quasichanneling oscillations in the deflection angle distribution*:

$$\begin{aligned} \theta'_{Xdef\ n} &= \theta_d - \sqrt{\frac{2d_0 n}{R}}; \\ \theta''_{Xdef\ n} &= \theta_d - \sqrt{\frac{2d_0 n}{R} + \frac{2\Delta V}{pv}}. \end{aligned} \tag{5.19}$$

In this equations the bending angle θ_b was replaced by the peak deflection angle in channeling mode θ_d to describe a possible misalignment of a bent crystal $\theta_{cr} = \theta_d - \theta_b$ which shifts both the channeling peak and quasichanneling peaks.

Negative particles tend to be closer to the first angle while the positive to the second one, where the derivative $d\theta_{Xdef}/dz$ is smoother.

However, under influence of scattering the peaks can be blurred and overlapped because of close values of particle deflection angles in the interval $[\theta'_{Xdef\ n}, \theta''_{Xdef\ n}]$. Generally such pair of peaks will form a “combined” peak, located between them. As it will be shown in our simulations, the intervals (5.19) can also overlap depending on R, when $\Delta V > V_0$, which approximately corresponds to $R > 7R_{cr}$. Therefore, the peaks can be formed at the intersection of these zones.

The angular difference between such neighboring peaks $\Delta\varphi_{qch}$ can be found from these equations as:

$$\Delta\varphi_{qch} = \sqrt{\frac{2d_0}{R} + (\theta_d - \theta_{Xdef})^2} - (\theta_b - \theta_{Xdef}). \tag{5.20}$$

Both of Eq. (5.19) give the same result (5.20). Thus, having the position of one peak of quasichanneling oscillations located between boundaries (5.19), one can use the formula (5.20) to obtain the next one on the left side from the previous (see Fig. 5.1). For large n, the equation (5.20) reduces into:

$$\Delta\varphi_{qch} \approx \frac{d_0}{R(\theta_d - \theta_{Xdef})}. \tag{5.21}$$

It is important to stress that such formula does not depend on the particle energy but only on crystal characteristics, such as interplanar distance and bending radius.

Being an over-barrier effect, quasichanneling oscillations can be experimentally observed for any angular divergence less, of course, than the crystal bending angle. The main constraint here is the limited statistics of the over-barrier particles in the angular distribution, which depends in turn on channeling efficiency. Therefore, short crystals are preferred to provide the highest efficiency.

In order to find the extremal conditions where the observation of quasichanneling oscillations is still possible, one can estimate only the first oscillation forming the closest peak to the channeling one. For the initial angle θ_{Xdef} in (5.21) one should take the left boundary of the channeling peak to be $\theta_b - \theta_L$. In this case one obtains the highest possible angular difference between the channeling peak and the peak of a quasichanneling oscillation:

$$\frac{\Delta\varphi_{qch}}{2\theta_{sc2}} = \frac{d_0}{2R\theta_L} \frac{pv\sqrt{\frac{X_r}{\lambda_1}}}{13.6MeV\left(1 + 0.038\ln\left(\frac{\lambda_1}{X_r}\right)\right)} > 1. \tag{5.22}$$

λ_1 can be roughly estimated to be equal to half of the channeling oscillation length (1.29), i.e. $\lambda_1 \sim \lambda/2$, in contrast to (5.3) representing the remaining particle distance in a crystal after dechanneling.

In order to observe quasichanneling oscillations, one should also satisfy the condition of the bending radius to be larger than the critical one (5.4).

Since Eq. (5.22) for quasichanneling oscillations depends on energy like Eq. (5.9) for channeling oscillations, they scale on energy in the same way.

The ratio of maximal interpeak distance of quasichanneling oscillations to that of channeling oscillations can be estimated by using (1.29), (5.3), (5.5) and (5.22), resulting in:

$$\frac{\Delta\varphi_{qch}}{\Delta\varphi_{ch}} < \frac{2}{\pi}. \tag{5.23}$$

For volume reflection, the analogous ratio will be two times lower. Thus, the width between the peaks for channeling oscillations is considerably higher than for the quasichanneling ones. However, the different role of multiple scattering (compare (5.3) and (5.22)) and angular divergence makes the conditions for observation of quasichanneling generally more preferable.

5.4 Simulation results

For a deeper understanding of both channeling and quasichanneling oscillations we performed a numerical simulation.

The program CRYSTAL [A1, A3] was applied for simulations. The simulations were performed for a single passage of charged particles through the crystal. The typical statistics was 10^6 particles. The angular divergence of the initial beam was set to be less than $\theta_L/4$. The bent crystal parameters were chosen to fulfil the conditions (5.3-5.4, 5.22) for clear observation of both channeling and quasichanneling oscillations.

The simulation of the distributions of the particle angles after interaction of particles with the crystal is shown in Figs. 5.9-5.10 for channeling and in Fig. 5.11 for volume reflection orientations. The energy in the simulation was chosen in correspondence to the beam energy in currently operating accelerators.

Both channeling and quasichanneling oscillations are observable. Moreover, they are in a good agreement with the estimations obtained above. In particular, the simulated interpeak distance for channeling oscillations is consistent with the estimation of channeling oscillation length (1.29). The highest deviation is for 20.35 GeV because in that case the bending radius is close to the critical radius. The correlations quickly disappear also because of rather small bending radius. As mentioned above for volume reflection, the interpeak distance corresponds to one oscillation length, in contrast to channeling for which interpeak distance is half of one oscillation length. As expected, the planar channeling oscillations are not observed for negative particles.

Simulated quasichanneling oscillations agree with formulae (5.19-5.20) for both signs of particles even for the first oscillation, i.e., the closest one to the channeling peak. Vertical lines calculated by (5.19) define the location of peaks

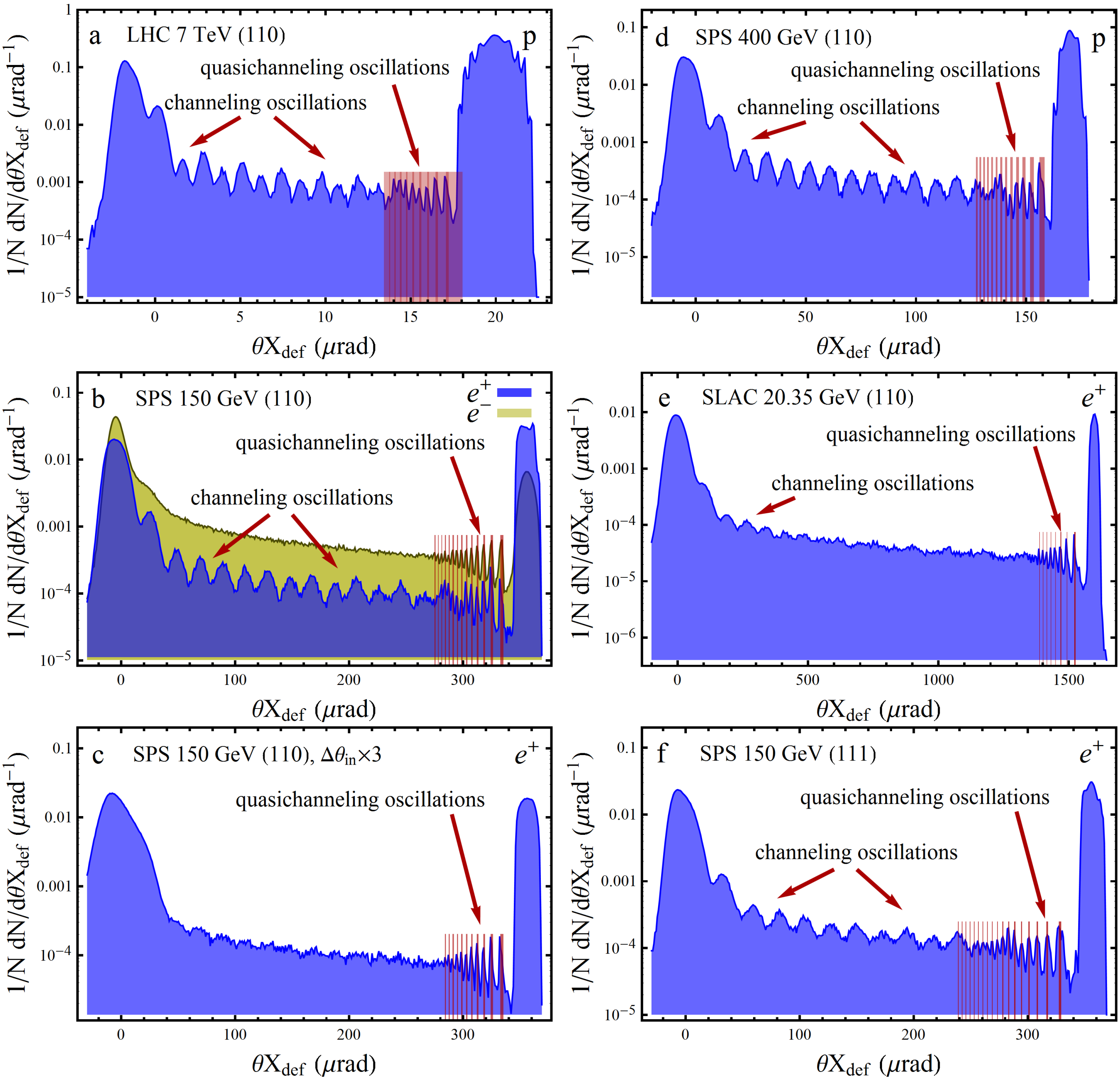

Figure 5.9: The angular distributions of particles after interaction with the silicon crystal at the channeling orientation. Vertical lines indicate the zone of quasichanneling oscillations manifestation calculated by Eq. (5.19). The simulation layouts were as follows: (a) LHC, 7 TeV protons, r.m.s. beam angular divergence $\theta_{in} = 0.5\mu rad$, $l_{cr} = 2mm$, $\theta_b = 20\mu rad$, (110) planes; (b) SPS, 150 GeV positrons and electrons, $\theta_{in} = 3.5\mu rad$, $l_{cr} = 0.29mm$, $\theta_b = 357\mu rad$, (110) planes; (c) the same as the previous except the angular divergence $\theta_{in} = 10.5\mu rad$; (d) SPS, 400 GeV protons, $\theta_{in} = 2\mu rad$, $l_{cr} = 0.48mm$, $\theta_b = 170\mu rad$, (110) planes; (e) SLAC, 20.35 GeV positrons, $\theta_{in} = 10\mu rad$, $l_{cr} = 0.11mm$, $\theta_b = 1600\mu rad$, (110) planes; (f) the same as (b) for (111) planes.

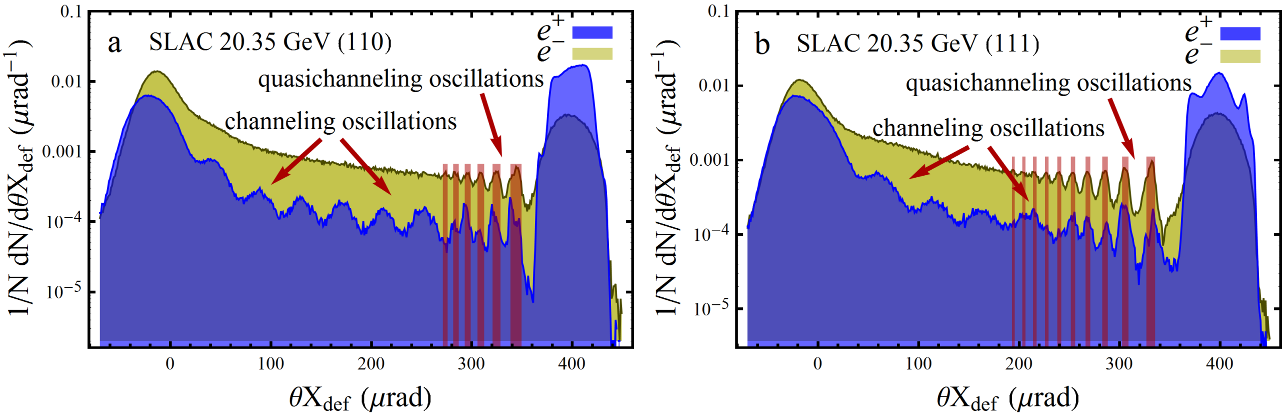

Figure 5.10: (a) SLAC, 20.35 GeV positrons and electrons, $\theta_{in} = 10\mu rad$, $l_{cr} = 60\mu m$, $\theta_b = 400\mu rad$, (110); (b) the same as (g) for (111) planes.

for quasichanneling oscillations and their agreement with the simulations. It is important to underline that for the case of 7 TeV the quasichanneling oscillations are revealed not in the zones predicted by Eq. (5.19) but at intersections of such zones.

It is important to emphasize that the angular difference (5.20-5.21) is on the left of the peak located at θ_{Xdef}. The angular distance between the peaks decreases w.r.t. the angle measured from the channeling peak. In addition, the particles in next peaks undergo more oscillations and travel longer under over-barrier state, resulting in increased scattering angle. Because of this, only the peaks of quasichanneling oscillations near the channeling bump can be observed. Qualitatively, this is the manifestation of condition (5.22).

One can notice in Figs. 5.9-5.11 the asymmetric peaks due to the particles that remain channeled at the crystal exit. It is explained by the particles with large amplitudes in channeling oscillations, keeping the same angles for a long distance near the potential bottom or top. For a straight crystal this effect could also be observed.

The angular distribution of particles after their interaction with the crystal was obtained also with the increased angular divergence of the initial beam by approximately $3/4\theta_L$. The corresponding cases are shown in Figs. 5.9 and 5.11 for 150 GeV. Indeed, too large an angular divergence leads to the disappearance of the peaks of planar channeling oscillations. As mentioned above, quasichanneling oscillations do not directly depend on the angular divergence. Thereby, such peaks remain visible.

In Fig. 5.9 the four upper plots represent the scaling on energy (5.8-5.9) introduced in the previous section. The same scaling is represented in Fig. 5.11 for volume reflection.

Such scaling is good for the energies of the same order. In the opposite

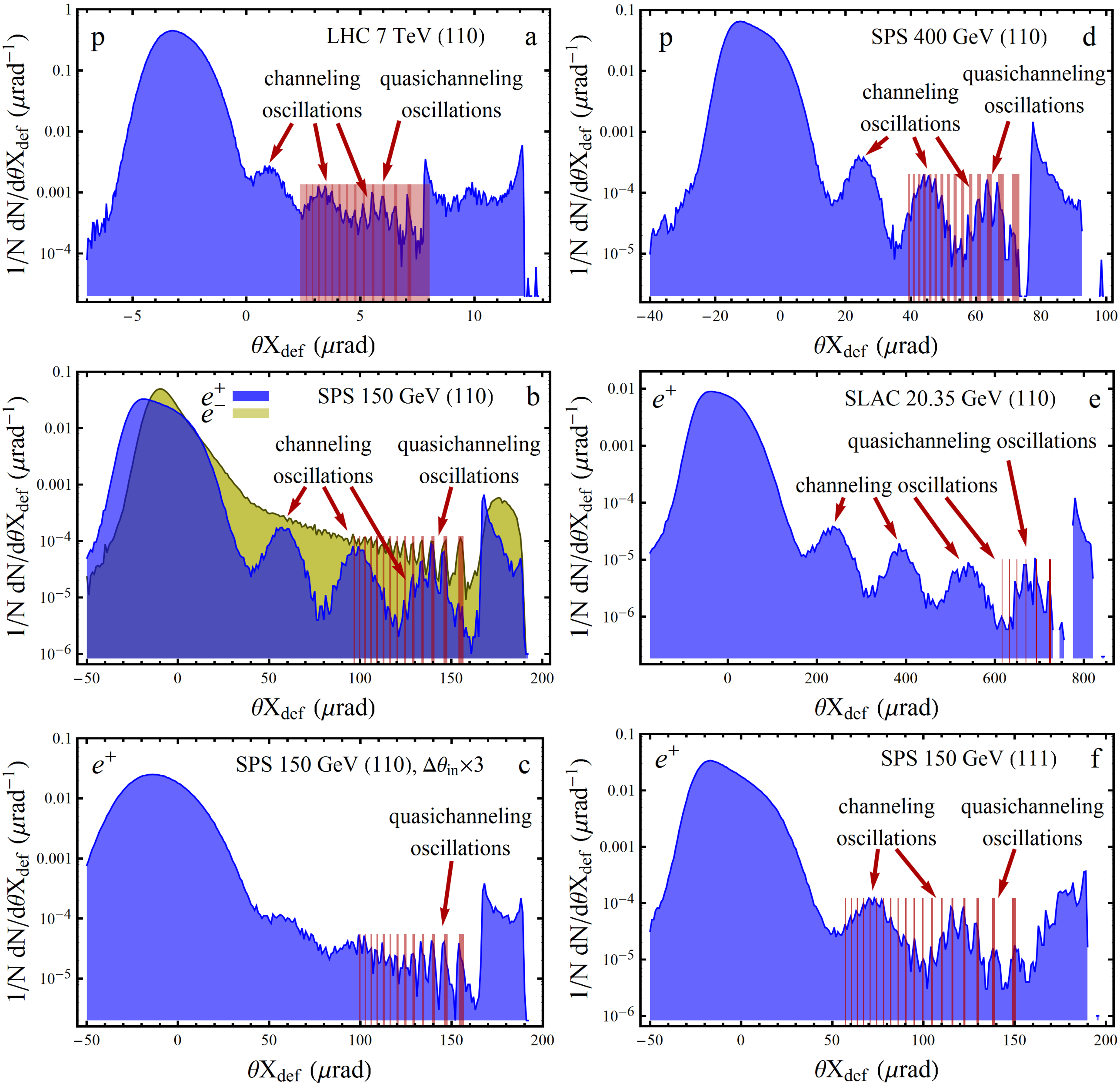

Figure 5.11: The angular distributions of particles after interaction with the silicon crystal at the volume reflection orientation for the crystal tilt $-\theta_b/2$. Vertical lines indicate the zone of quasichanneling oscillations manifestation calculated by Eqs. (5.19). The simulation layouts were as follows: (a) LHC, 7 TeV protons, r.m.s. beam angular divergence $\theta_{in} = 0.5\mu rad$, $l_{cr} = 2mm$, $\theta_b = 20\mu rad$, (110) planes; (b) SPS, 150 GeV positrons and electrons, $\theta_{in} = 3.5\mu rad$, $l_{cr} = 0.29mm$, $\theta_b = 357\mu rad$, (110) planes; (c) the same as (b) for the angular divergence $\theta_{in} = 10.5\mu rad$ for positrons; (d) SPS, 400 GeV protons, $\theta_{in} = 2\mu rad$, $l_{cr} = 0.48mm$, $\theta_b = 170\mu rad$, (110) planes; (e) SLAC, 20.35 GeV positrons, $\theta_{in} = 10\mu rad$, $l_{cr} = 0.11mm$, $\theta_b = 1600\mu rad$, (110) planes; (f) the same as (b) for (111) planes for positrons.

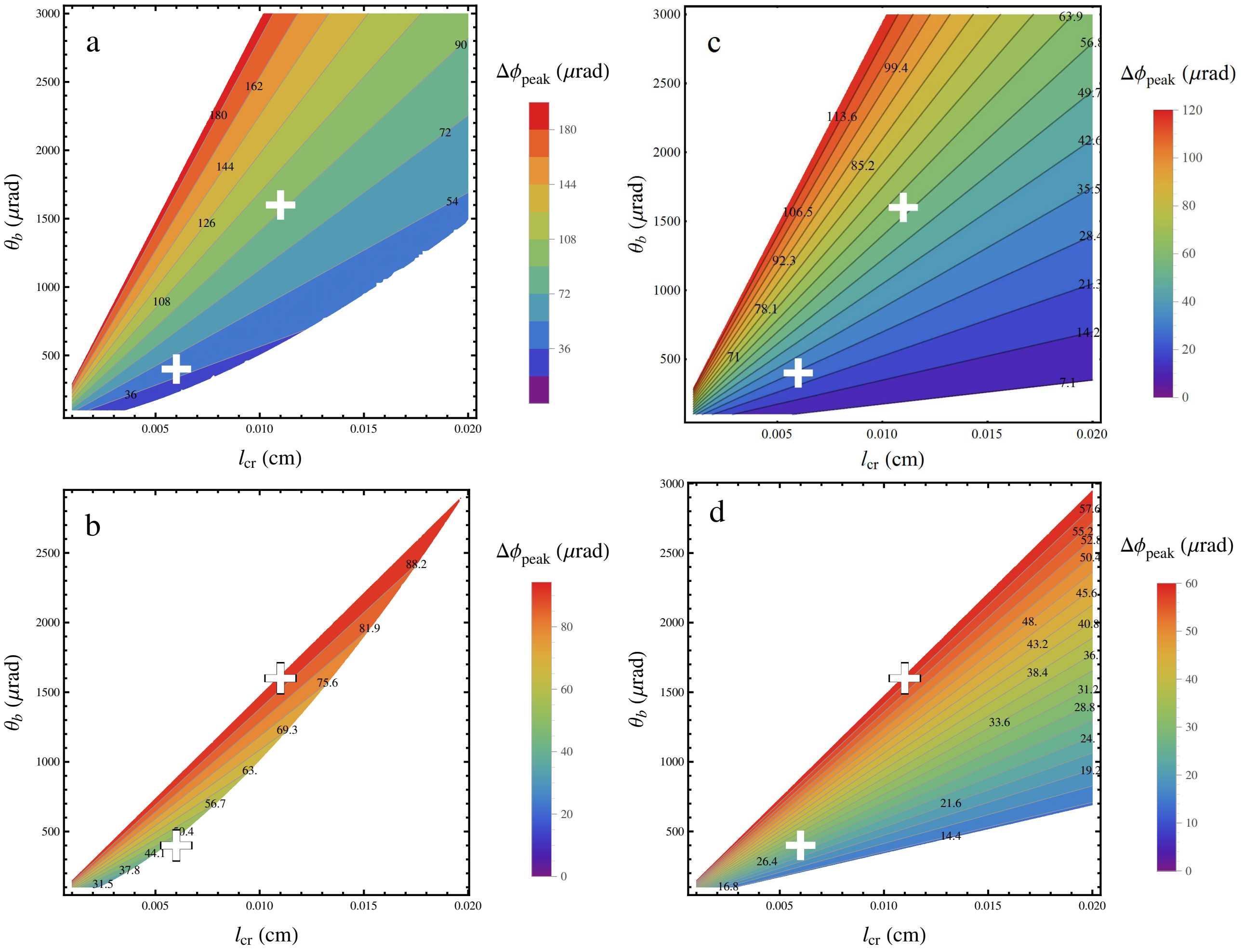

Figure 5.12: The dependence of the angular distance between the peaks corresponding to the channeling (a) and quasichanneling (c) oscillations on the crystal length and the bending angle for the positrons of 20.35 GeV. The (110) silicon planes are considered. The zone for the dechanneling peaks observation is formed by (5.3-5.4). (b,d): the optimal zones for the same cases for the channeling and quasichanneling oscillations respectively, the ratios in (5.3-5.4) and (5.22, 5.4) exceed two.

case, the radius can approach to the critical one, when the conditions for the observation of the planar channeling oscillations are not optimal. This is shown in Fig. 5.9 for channeling and in Fig. 5.11 for volume reflection. The obtained scaling provides a similar picture for different energies from hundreds of GeV up to 7 TeV. At the same time, the picture for the case of 20.35 GeV is different and not so evident because the bending radius approaches to its critical radius.

For the (111) crystal planes the picture observed is analogous to that for the (110) planes (see Figs. 5.9-5.10). For planar channeling oscillations the interpeak distance is proportional to the channeling oscillation length in the larger channel as shown in Fig. 5.2. The quasichanneling oscillations are well described by formulae (5.19-5.20) if the interplanar distance is determined as a transverse period being equal to 3.13Å for silicon.

5.5 Possible experimental set-up to observe planar channeling and quasichanneling oscillations

In this section we provide information on possible experimental set-ups for observation of planar channeling and quasichanneling oscillations through existing accelerators worldwide. In order to span over different energy and charge, we considered the cases of both positrons and electrons at SLAC (20.35 GeV) and SPS, CERN (150 GeV) and of electrons at MAMI (855 MeV).

For successful observation, it is very important to choose the proper parameters for the crystal geometry. They are provided by Eqs. (5.3-5.4) for channeling oscillations and by Eqs. (5.22, 5.4) for quasichanneling. However, in a real experiment the angular distance between the peaks should be as large as possible to better resolve them. All these conditions can be visually combined in the dependence of the distance between the peaks on the crystal length and bending angle.

Such dependence is shown in Fig. 5.12 for the channeling oscillations at the channeling orientation of the energy of 20.35 GeV. White crosses mark the crystal geometry simulated in this paper and presented in Fig. 5.9-5.10. The conditions (5.3-5.4) determine the area, where the observation of planar channeling oscillations is allowed. In order to optimize the crystal parameters the ratios (5.3-5.4) should be safely taken as 2-3 times as much. For equation (5.3) this choice results in a clearer picture of the peaks. At the same time, for the ratio (5.4), it provides higher channeling efficiency for better statistics of the experiment.

An example of optimized zone for crystal geometry for a SLAC case is shown in Fig. 5.12b. The estimates (5.3-5.4) provide a sufficiently narrow region of crystal parameters. However, in any case a concrete experimental layout should be checked by Monte-Carlo trajectory simulations.

Similar conclusion can be inferred by application of Eqs. (5.22, 5.4) to the plots for quasichanneling oscillations. These dependencies are represented in Fig. 5.12 for 20.35 GeV. White crosses in the optimal zone indicate the parameters used in this paper. Quasichanneling oscillations are indeed observed for our simulations for all the cases considered.

The algorithm for crystal geometry optimization remains the same as for the quasichanneling oscillations. The only difference is that the initial angular divergence of the beam should be much less important than for planar channeling oscillations. The angular divergence in our simulations was equal to 10 μrad, a value which may be experimentally achieved. Thus, the SLAC case satisfies all the conditions of the observation of planar channeling and quasichanneling

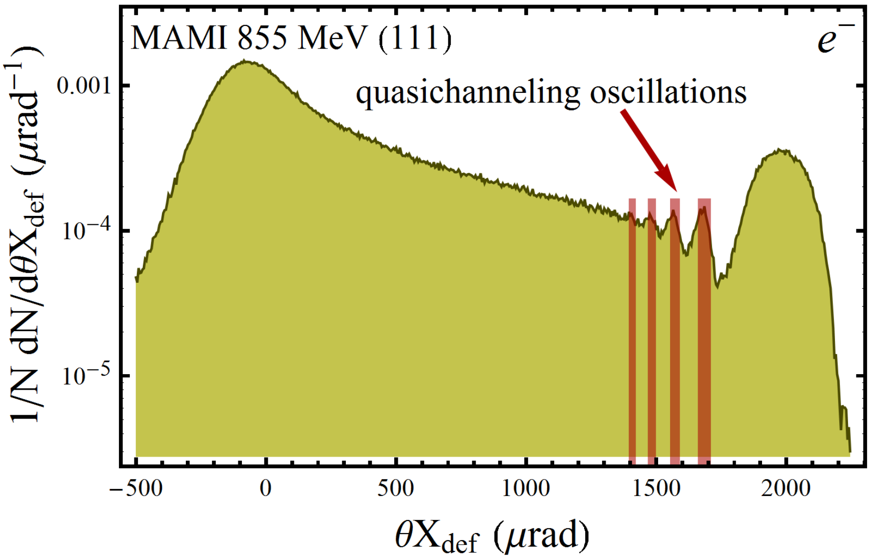

Figure 5.13: The angular distributions of particles after interaction with the silicon crystal at the channeling orientation. The simulation layout is: 855 MeV electrons, $\theta_{in} = 50\mu rad$, $l_{cr} = 15\mu m$, $\theta_b = 2000\mu rad$, (111) planes.

oscillations.

For the SPS case, the crucial factor is the angular resolution of the detector. At energies of the order of hundreds GeV, the resolution of at least several microradians should be provided. At the SPS, additional scattering by air and the silicon strip detectors contributes to the measurements. This contribution can be taken into account by including the corresponding r.m.s. scattering angle θ_{det} to the denominator of (5.3) and (5.22):

$$\frac{\Delta\varphi_{ch}}{2\sqrt{\theta_{sc}^2 + \theta_{det}^2}} > 1. \tag{5.24}$$

The angular divergence at the SPS is expected to be higher when using secondary beams of positrons or electrons. In this case only quasichanneling oscillations can be observed.

For electrons only quasichanneling oscillations can be observed as at the MAMI microtron (see setup in [133] and the previous chapter). The simulation of such experiment is shown in Fig. 5.13. The main problem for this experiment is crystal manufacturing. For operation of sub-GeV energies, a very short and strongly bent crystal is required, which is at the limit of existing technologies.

(111) crystal planes provide wider angular distance between the peaks. Thus, they should be preferable. Moreover, it is simpler to manufacture (111) bent crystal than for any direction, when strong bending is required [146]. The latter case especially relates to smaller energies of 1 GeV order at which such crystals were successfully applied [29,30,53] and [A7]. For electrons (111) planes provide a deeper potential well than the (110) ones. This results in a higher

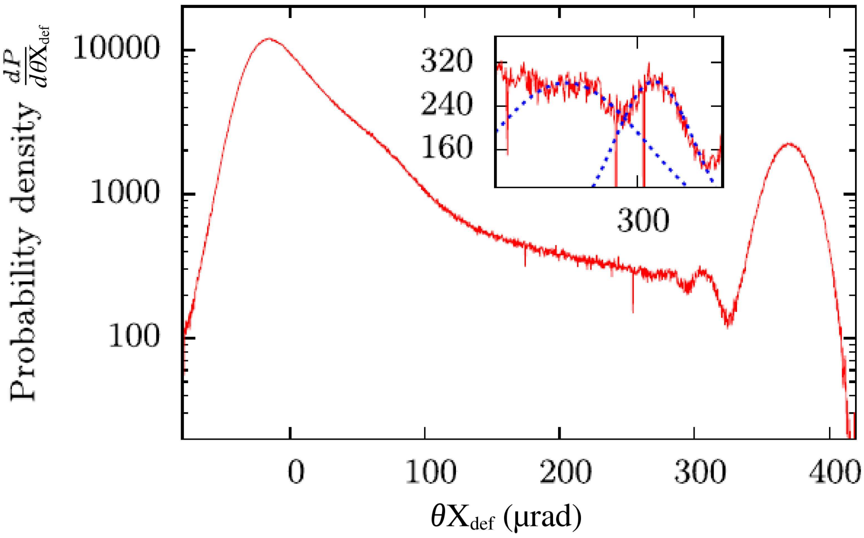

Figure 5.14: Angular distribution of electrons obtained at channeling conditions. The inserted plot provides a zoom in the regions around the quasichanneling peaks. The blue curves represent gaussian fit for each peak, carried out to obtain the position of its center. Fits were performed for the angles of deflection of 0.33–0.36 mrad and 0.36–0.39 mrad, respectively.

channeling efficiency which is also preferred.

5.6 Experimental observation of quasichanneling oscillations

The experiments were carried out at the SLAC Facility for Advanced Accelerator Experimental Tests (FACET) with both electrons and positrons at the energy 20.35 GeV, as considered above. The bent silicon crystal, fabricated at the University of Ferrara [146] was of $l_{cr} = 60 \pm 1\mu$m length. The (111) bent planes of this crystal were obtained by using the quasimosaic effect [131]. The bending angle was $\theta_b = 402 \pm 9\mu$rad as well as, the bending radius was $R = 15.00 \pm 0.42$cm. The spatial resolution of the $e^{\pm}$ detector screen was 3.5μm.

The experimental angular distribution of electron beam, deflected at channeling conditions is shown in Fig. 5.14.

At angles slightly below the channeling peak, the quasichanneling oscillations are visible, as predicted above [A4]. Namely two quasichanneling peaks can be revealed. The positions of these two peaks were obtained by Gaussian fit functions as well as the angular distance between them, being $30.5 \pm 2\mu$rad. This is a bit higher than the theoretical estimate for the distance between the quasichanneling peaks μrad, based on Eq. (5.19). The agreement, though not perfectly, is rather convincing to approve the theory by experimental observa-

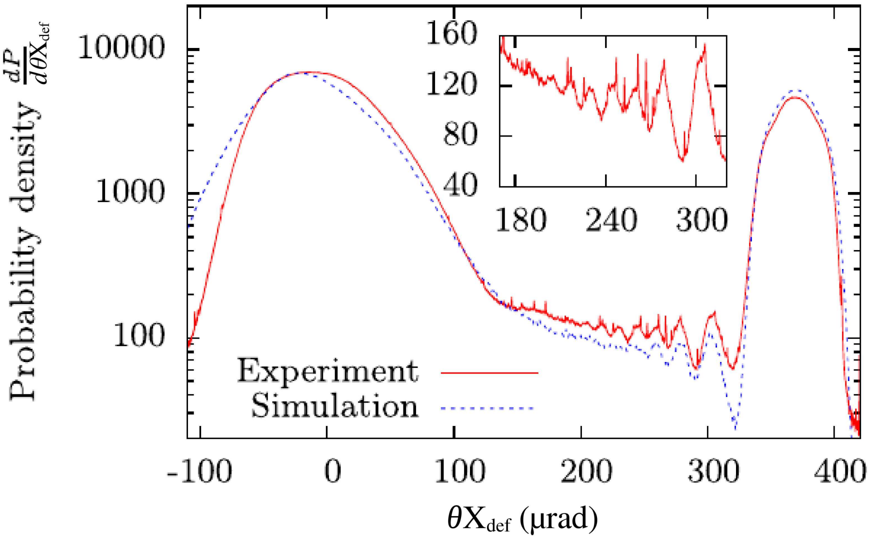

Figure 5.15: Angular distribution of positrons obtained at channeling conditions. The dashed blue line shows the result of simulations.

tions.

The experiment was carried out for positrons at channeling orientation [A6]. At the experimental angular distribution, shown in Fig. 5.15, quasichanneling oscillations can be clearly revealed at deflection angles of ∼0.2–0.36 mrad. This angular region, zoomed in, is also shown in Fig. 5.15. The simulations results, carried out with the CRYSTAL simulation code, shown in Fig. 5.15 as the blue dashed line, are in good agreement with the experiment.

The experimental peaks were fitted by Gaussian fit to obtain their positions, see Table 5.1.

Table 5.1: A table showing the positions and uncertainty (σ) of the quasichanneling peaks for positrons.

n	2	3	4	5	6	7	8
θ_{peak} (μrad)	299	275	256	241	226	213	201
σ_{peak} (μrad)	4.1	3.5	3.8	3.5	3.6	3.9	3.7

These positions were used as an input to a fitting procedure based on Eq. (5.19), which should be rewritten for (111) planes in the form:

$$\theta_{Xdef\ n} = \theta_d - \sqrt{\frac{2d_0(n-1)}{R} + 2d_s/R}, \tag{5.25}$$

where d_s is the distance between the closest planes, being equal for (111) planes to $d_0/4$. Therefore the equation (5.25) can be rewritten as:

$$\theta_{Xdef\ n} = \theta_d - \sqrt{\frac{d_0}{R}}\sqrt{2(n-1)+1/2}. \tag{5.26}$$

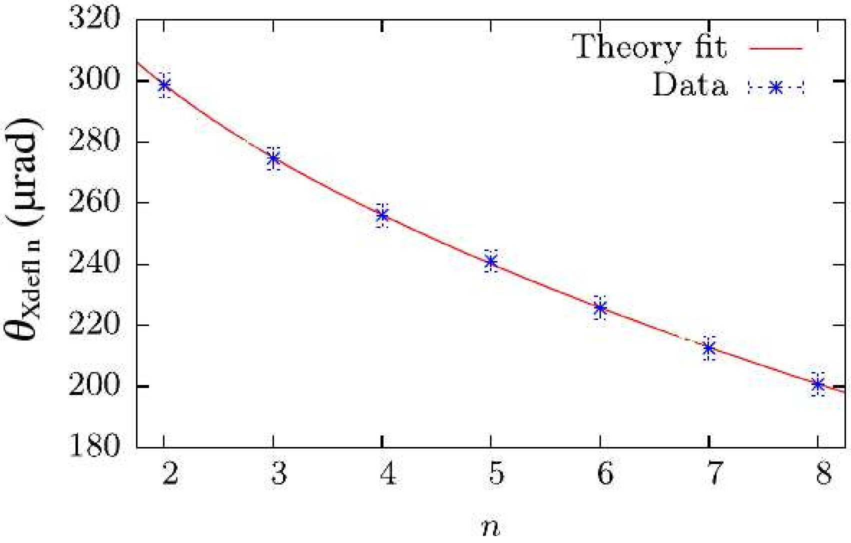

Figure 5.16: The experimentally obtained positions of the quasichanneling peaks for positrons along with a fit based on Eq. (5.25).

Consequently, the fit will be carried out on the two parameters, namely θ_d and $a = \sqrt{\frac{d_0}{R}}$. The peak number starts from $n = 2$ since the first peak is hidden inside the channeling peak.

From the fit, one obtains $a = (4.39 \pm 0.13) \times 10^{-5}$ and $\theta_d = (368 \pm 1.8)\mu$rad. The value of θ_d fits well with the observed position of the channeling peak in Fig. 4 of 369μrad. The comparison of the fit and data can be seen in Fig. 5.16. From Eq. (5.25), the value of $a = (4.57 \pm 0.06) \times 10^{-5}$ is expected, where the uncertainty comes from the uncertainty on R. Therefore, one can conclude that theory and experiment show agreement within the experimental uncertainty. It is important to stress that the peaks, observed experimentally, are not equidistant and, by this reason, cannot be explained by channeling oscillations. This is also confirmed by the fact, that the peaks with nearly the same positions are observed also for electrons and cannot be explained by channeling oscillations as was mensioned above. Basing on this reason as well as on agreement between theory and experiment one can conclude that the observed oscillations must be the quasichanneling oscillations.

The experiment was performed with a β-function of $\beta_x = \beta_y = 10$m, leading to an angular divergence in the deflection plane of approximately 20μrad for e^+ and 10μrad for e^-, with about a factor of 2 systematic uncertainty. For electrons, additional measurements were done for other values of beam divergences, i.e., beta functions of $\beta_x = \beta_y = 20$m and $\beta_x = \beta_y = 100$m. No quasichanneling oscillations were observed for these values of the β-function for electrons. The reason is that not only the angular divergence but also the size of the beam also increases with increasing beta functions. This becomes detrimental to the observation of the quasichanneling oscillations, because in fact the value of beam size, divided by the optical distance from the crystal to the detector $\Delta\sigma/L_{acc}$ can exceed the angular distance between the quasichanneling peaks (see Eq. (5.24), $\theta_{det} = \Delta\sigma/L_{acc}$), erasing in a such way the quasichanneling oscillations in the angular distribution. Therefore, for the observation of quasichanneling oscillations one needs small transverse size of the beam.

One can conclude that the quasichanneling oscillations, presented for the first time in an experiment, are observed in good agreement with theory and simulations.

5.7 Possible application of channeling and quasichanneling oscillations

By measuring the positions of the quasichanneling peaks, one can extract information for both bent crystal radius R and orientation $\theta_{cr} = \theta_d - \theta_b$ in one single measurement, i.e., for one goniometer position. Indeed, existing methods require the rotation of the goniometer at different positions around channeling to measure the crystal-to-beam orientation and consequent analysis of the beam deflection efficiency, which is not always so straightforward. The knowledge of the position of the quasichanneling peaks would improve the alignment procedure between the bent crystal planes and the beam direction, even for large misalignment, in high-energy accelerators, where the crystal can be exploited as a passive and inexpensive tool for beam extraction or collimation. Furthermore, with the use of a bent crystal, one may provide a direct measurement of the quasichanneling oscillation wavelength, in analogy with the channeling one (λ), as a function of the distance between quasichanneling peaks: $\lambda_{qch} = R\Delta\varphi_{qch}$. The same can be done with channeling oscillations: $\lambda_{ch} = R\Delta\varphi_{ch}$. Such values may provide an insight to the interplanar potential shape and strength and on the dynamics of over-barrier particles, thus giving important information for applications in high-energy particle accelerators for either beam steering or intense electromagnetic radiation generation.

5.8 Conclusions

The effects of *planar channeling* and *quasichanneling oscillations in the deflection angle distribution* of particles passed through a bent crystal has been predicted. Both of them possess a fine structure in the angular distribution as visualized by Monte Carlo simulations for a wide range of energies. The effect of quasichanneling oscillations was observed experimentally for the first time. In addition, the effect of ionization losses excess over the amorphous level was obtained in simulations at ionization losses map in which the trajectory correlations, transforming into channeling oscillations in the deflection angle distribution were clearly revealed.

The theoretical interpretation of both kinds of oscillations was proposed. Quasichanneling oscillations appear near the direction at which channeling particles leave the crystal. They arise due to the correlations of over-barrier oscillation lengths of dechanneled particles. Channeling oscillations can be observed in all over the angular range of deflected particles after interaction with a crystal. This effect arises from correlated dechanneling of particles moving along phase-correlated trajectories under channeling mode. An equation for the angular positions of quasichanneling peaks was found. It demonstrates the independence of peak position on charge sign and energy.

Since phase correlation for channeled particles is conserved only for positive particles, the channeling oscillation peaks can not be observed for negative charges. At the same time, since both negatively and positively charged particles may experience over-barrier oscillations, the effect of quasichanneling oscillations can be observed for both of them.

The possibility to observe both channeling and quasichanneling oscillations is limited by incoherent scattering of particles under over-barrier states. Both of them can be observed if only the r.m.s. angle of incoherent scattering is twice smaller than the interpeak angular intervals. The angular resolution of particle detectors is crucial for the observation of both types of oscillations. However, the low angular divergence of the incident beam is necessary only for an observation of the channeling oscillations.

The optimal conditions for experimental observation of both channeling and quasichanneling oscillations are also proposed. These conditions are applied to elaborate the optimal values of crystal thickness and bending angle (radius) at SLAC, SPS, MAMI and LHC. A comparison of (110) and (111) planar crystal orientation reveals the higher interpeak distance and higher electron channeling efficiency in the case of the latter. (111) orientation is also preferable from the point of view of strong bending of thin crystals to observe the predicted effects at the SLAC and MAMI energies.

Quasichanneling oscillations were observed experimentally at SLAC for both electrons and positrons at the energy of 20.35 GeV for (111) bent crystal planes. For positrons the peak positions were verified by fit, provided by theoretical model, which gave the values being in agreement with theory within the experimental uncertainty.

Similarly to channeling oscillations, which are used in low-energy RBS experiments to assess the quality of a crystal, channeling and quasichanneling oscillations could be used to determine the precision of alignment of a high-energy beam with a crystal. In fact, the pattern of the distribution of particles after interaction with a bent crystal is highly sensitive to the beam-to-crystal alignment. Moreover, the interpeak distance between both dechanneling and quasichanneling peaks is proportional to the oscillation length of channeling and quasichanneling oscillations respectively. This can give an insight to the interplanar potential shape and strength and on the dynamics of channeling and over-barrier particles. All this information can be used for all the applications for which bent crystals are used in accelerators, such as beam collimation, extraction and e.m. radiation generation.

CONCLUSIONS

The work in this thesis has been dedicated to the coherent effects of beam steering in bent crystals and their application at high energy accelerators. These effects were studied both theoretically and by simulations. Some of them were observed experimentally, analysed as well as critically compared with theoretical predictions and simulations.

The effects of channeling and volume reflection were simulated for 50 TeV protons, i.e. at the energy of the Future Circular Collider. For volume reflection angle a model independent on the particle energy has being presented. Moreover a number of modifications of these effects were studied. Namely volume reflection in a sequence of bent crystals, multiple volume reflection in one bent crystal as well as the combination of both was simulated. In addition a theoretical model to optimize the parameters of the crystal geometry as well as its orientation w.r.t. the initial beam direction has been introduced. The effects were simulated not only for silicon, but also for more high-Z crystals, namely germanium and tungsten. The maximal angle of deflection, comparable with the angle of deflection under channeling conditions has been achieved.

Channeling in skew planes provides considerably higher deflection angle of non-channeling particles by application of MVROC instead of volume reflection. A bent crystal in fact works as a beam splitter, deflecting charged particles in two directions. The application of a crystal with a cut allows one to increase the channeling efficiency on about 10% for the cases considered.

The double collimation scheme has been suggested for the Future Circular Collider, basing on the coherent effects studied in this work. This collimation scheme includes two crystals. The first one is suggested as a beam splitter, deflecting most particles under the channeling conditions into the collimator as well as the remaining part onto the second crystal. The main idea of such collimation setup is interception of most of halo particles during only one passage of the collimation insertion, namely up to 99.9%.

Channeling and volume reflection have been also studied for negatively charged particles, namely for 855 MeV electrons at Mainzer Mikrotron MAMI. The experimental results demonstrated a record channeling efficiency of negative particles in a silicon crystal, i.e. close to 40%. Moreover beam steering of sub-GeV eletrons in germanium bent crystal has been demonstrated for the very first time.

Dechanneling length and channeling efficiency as well as volume reflection angle was measured in dependence of the value of crystal curvature for both silicon and germanium bent crystals. It was done by application of the innovative pieso-activated dynamical holder, allowing one to bend a crystal inside an accelerator facility without vacuum breaking. The results were critically compared with both theoretical model and simulations, showing a good agreement. The influence of initially non-channeled particles on the process of dechanneling, causing a reduction of the dechanneling length in case the crystal thicknesses are comparable with the dechanneling length, was also exposed.

These results, are of interest for applications, such as generation of e.m. radiation in higher Z-materials crystals. Moreover the can be extrapolated on charged particle steering at higher energies, for instance for crystal-based collimation/extraction at future electrons accelerators.

The effects of planar channeling and quasichanneling oscillations in the deflection angle distribution have been predicted both theoretically and by simulations. Both effects allow one to observe directly the particle oscillations under the channeling and quasichanneling conditions, being trasformed in the angular distribution into a series of peaks equidistant and non-equidistant respectively. The theoretical model of both effects has been introduced as well as experimental conditions have been formulated. In addition, the effect of excess of the ionization losses over the amorphous level for (110) planes, has been highlighted. It is directly connected with the effect of planar channeling oscillations, being also another representation of the latter.

The effect of planar quasichanneling oscillations in the deflection angle distribution has been observed experimentally at the FACET accelerator facility at SLAC for both electrons and positrons of 20.35 GeV. The experimental results are in agreement with the theoretical model proposed. Moreover the procedure of fitting of crystal alignment and geometry, based on the peaks positions was carried out. This procedure represents the measuring of the alignment by using only one angular distribution of deflected beam, being useful at high energy accelerators, to align a bent crystal more precisely. Moreover, both planar channeling and quasichanneling oscillations can give an insight to the interplanar potential characteristics as well as on the dynamics of channeling and over-barrier particles. These applications are also relevent for beam steering, and in particular for crystal-based collimation and beam extraction at modern and future accelerators and colliders.

BIBLIOGRAPHY

1. J. Stark, Zs. Phys. **13**, 973–977 (1912).
2. J. A. Davies, J. Friesen, J. D. McIntyre, Can J. Chem. **38**, 1526–1534 (1960).
3. M. T. Robinson, O. S. Oen, Appl. Phys. Lett. **2**, 30–32 (1963).
4. J. Lindhard, Kgl. Dan. Vid. Selsk. Mat.-Fys. Medd. **34** No 4, 2821–2836 (1965).
5. E.N. Tsyganov, *Some aspects of the mechanism of a charge particle penetration through a monocrystal*, Tech. Rep. (Fermilab, 1976) preprint TM-682.
6. A. Taratin, Phys. Lett. A **119** No. 8, 425 (1987).
7. A. M. Taratin and S. A. Vorobiev, Nucl. Instrum. Methods in Phys. Res. B **26**, 512–521 (1987).
8. W. Scandale et al. Phys. Lett. B **680**, 129–132 (2009).
9. M. Pesaresi et al., JINST **6**, P04006 (2011).
10. S. Hasan et al. Nucl. Instr. and Meth. in Phys. Res. B **269**, 612–621 (2011).
11. R. Rossi et al., Nucl. Instr. and Meth. in Phys. Res. B **355**, 369–373 (2015).
12. E. Bagli *et al*, Phys. Rev. Lett. **115**, 015503 (2015).
13. E. Bagli et al., Eur. Phys. J. C **74**, 2740 (2014).
14. E. Bagli et al. Eur. Phys. J. C **77**, 71 (2017).
15. C. Biino et al., Phys. Rev. B **403**, 163 (1997).
16. D. De Salvador et al. Appl. Phys. Lett. **98**, 234102 (2011).
17. D. De Salvador et al. AIP Conf. Proc. **1530**, 103-110 (2013).
18. D. De Salvador et al. Appl. Phys. Lett. **114**, 154902 (2013).
19. W. Scandale et al. Phys. Lett. B **680**, 301-304 (2009).
20. W. Scandale et al., Phys. Rev. Lett. **101**, 164801 (2008).
21. L. Bandiera *et al*, Eur. Phys. J. C. **76**, 80 (2016).
22. L. Bandiera et al, Nucl. Instr. and Meth. in Phys. Res. B **402**, 296–299 (2017).
23. W. Scandale et al., Phys. Lett. B **682**, 274 (2009).
24. V. Guidi, A. Mazzolari, and V. Tikhomirov, J. of Appl. Phys. **107**, 114908 (2010).
25. A. G. Afonin et al., JETP Lett. **93** No. 4, 187 (2011).
26. W. Scandale et al., EPL **93**, 56002 (2011).
27. W. Scandale et al. Phys. Lett. B **681**, 233-236 (2009).
28. W. Scandale et al. Phys. Lett. B **719**, 70 (2013).
29. A. Mazzolari et al., Phys. Rev. Lett. **112**, 135503 (2014).

30. U. Wienands et al. Phys. Rev. Lett. **114**, 074801 (2015).
31. T.N. Wistisen et al. Phys. Rev. Acc. and Beams **19**, 071001 (2016).
32. U. Wienands et al, Nucl. Instr. and Meth. in Phys. Res. B **402**, 11–15 (2017).
33. T.N. Wistisen et al. Phys. Rev. Lett. **119**, 024801 (2017).
34. H. Backe et al., Nucl. Inst. Meth. Phys. Res. B **266**, 3835–3851 (2008).
35. H. Backe et al., Nucl. Inst. Meth. Phys. Res. B **309**, 37 (2013).
36. H. Backe, and W. Lauth, Nucl. Instr. Meth. Phys. Res. B **355**, 24–29 (2015).
37. A. V. Korol, V. G. Bezchastnov, A. V. Solov'yov Eur. Phys. J. D **71**, 174 (2017).
38. A. G. Afonin et al., Phys. Rev. ST Accel. Beams **15**, 081001 (1–9) (2012).
39. A. G. Afonin et al., JETP Letters **84** No. 7, 37276 (2006).
40. A. Afonin et al., in *Proc. of 7th ICFA mini-workshop*, Lake Como 1999, pp. 127–130.
41. A. G. Afonin et al., Instr. and Exp. Techn. **54** Issue 1, 1 (2011).
42. Yu.A. Chesnokov et al., Nucl. Instr. and Meth. in Phys. Res. B **309**, 105 (2013).
43. N. V. Mokhov et al., Intern. J. of Mod. Phys. A **25**, Suppl. 1, 9875 (2010).
44. N. Mokhov et al., JINST **6**, T08005 (2011).
45. R.P. Fliller III et al., *RHIC crystal collimation* Nucl. Instr. and Meth. in Phys. Res. B **234**, 47–56 (2005)
46. W. Scandale et al., Phys. Lett. B **692**, 78–82 (2010).
47. W. Scandale et al., Phys. Lett. B **703**, 547–551 (2011).
48. W. Scandale et al., Phys. Lett. B **714**, 231–236 (2012).
49. W. Scandale et al., Phys. Lett. B **758**, 129-133 (2016).
50. R. Carrigan et al., Phys. Rev. ST Accel. Beams **5**, 043501 (2002).
51. V. Guidi, L. Bandiera, V. Tikhomirov, Phys. Rev. A **86**, 042903 (2012).
52. L. Bandiera et al., Nucl. Instr. and Meth. in Phys. Res. B **309**, 135-140 (2013).
53. L. Bandiera et al., Phys. Rev. Lett. **111**, 255502 (2013).
54. L. Bandiera et al., Journal of Physics: Conference Series **517**, 012043 (2014).
55. L. Bandiera et al., Phys. Rev. Lett. **115**, 025504 (2015).
56. L. Bandiera et al., Proc. of Science (ICHEP2016), 069 (2016).
57. D. S. Gemmell, Rev. Mod. Phys. **46**, 129 (1974).
58. M. A. Kumakhov, G. Shirmer, *Atomic Collisions in Crystals* (Atomizdat, Moscow 1980).

59. V. G. Baryshevsky, *Channeling, Radiation and Reactions in Crystals under High Energy* (Publishing house of Belarusian State Unuversity, Minsk, 1982)
60. L. Feldman, J. Mayer, and S. Picraux, *Materials analysis by ion channeling* (Academic Press, 1982).
61. Y.-H. Ohtsuki, *Charged Beam Interaction with Solids* (Taylor & Francis, London 1983).
62. V. Biryukov, Y. Chesnokov, and V. Kotov, *Crystal Channeling and its Application at High-Energy Accelerators* (Springer-Verlag, Berlin, 1997).
63. V. Baier, V. Katkov, and V. Strakhovenko, *Electromagnetic Processes at High Energies in Oriented Single Crystals* (World Scientific, Singapore, 1998).
64. U. I. Uggerhøj, *The interaction of relativistic particles with strong crystalline fields*, Rev. of Mod. Phys. **77**, 1131–1171 (2005).
65. A. G. Afonin et al., Phys.Part.Nucl. **36**, 21–50 (2005).
66. M. L. Ter-Mikaelian, *High-energy Electromagnetic Processes in Condensed Media* (Wiley, New York, 1972).
67. M. A. Kumakhov, F. F. Komarov, E. P. Velikhov (ed.) *Radiation from charged particles in solids* (New York, AIP, 1989).
68. V. G. Baryshevsky, I. D. Feranchuk, A. P. Ulyanenkov *Parametric x-ray radiation in crystals: Theory, experiment and applications* (Springer, Series: Springer Tracts in Modern Physics, 2005).
69. V.G. Baryshevskii, V.V. Tikhomirov, Zh. Eksp. Teor. Fiz. **90**, 1116–1123 (1986).
70. L. D. Landau, E. M. Lifshitz, *Quantum Mechanics: Non-Relativistic Theory. Vol. 3 (3rd ed.)* (Pergamon Press, 1977).
71. G. Molière, Z. Naturforsch. A **2**, 133 (1947).
72. B. R. Appleton, C. Erginsoy, and W. M. Gibson, Phys. Rev. **161**, 330 (1967).
73. W. K. Chu, W. R. Allen, S. T. Picraux, and J. A. Ellison, Phys. Rev. B **42**, 5923 (1990).
74. P. t. Doyle and P. Turner, Acta Crystallographica Section A: Crystal Physics, Diffraction, Theoretical and General Crystallography **24**, 390 (1968).
75. D. Cromer and J. Waber, Acta Crystallogr. **18**, 104 (1965).
76. D. Cromer and J. Waber, Acta Crystallogr. **19**, 224 (1965).
77. M. Tobiyama et al., Phys. Rev. B **44** N 17, 9248–9258 (1991).
78. S. L. Dudarev, L.-M. Peng, M. J. Whelan, Surf. Sc. **330**, 86–100 (1995).

79. Z. Su and P. Coppens, Acta Cryst. A **53**, 749-762 (1997).

80. P. J. Brown, et al., International Tables for Crystallography, **C** Section 6.1.1, 554–590 (2006).

81. Kittel C. *Introduction to Solid State Physics*, 8th ed. (Wiley, New York, 2005).

82. L. D. Landau, E. M. Lifshitz, *Statistical Physics. Vol. 5 (3rd ed.)* (Butterworth-Heinemann, 1980).

83. J. S. Blakmore, *Solid State Physics* (Cambridge University Press, Cambridge, 1985)

84. Appleton, B. R. , C. D. Moak, T. S. Noggle, and J. H. Barrett, Phys. Rev. Lett. 28, 1307 (1972).

85. L.D. Landau, E.M. Lifshitz, *Mechanics. Vol. 1 (3rd ed.)*, (Butterworth-Heinemann, 1976).

86. H. Bethe, Phys. Rev. **89**, 1256-1266 (1953).

87. GEANT4 4 9.5.0 Physics Reference Manual, http://geant4.cern.ch/, (6.70)-(6.73).

88. V. V. Tikhomirov, arXiv:1501.06588v1 (2015).

89. V.V. Tikhomirov, Nucl. Instr. Meth. in Phys. Res. B **36**, 282–285 (1989).

90. X. Artru, Nucl. Instr. Meth. in Phys. Res. B **48**, 278-282 (1990).

91. V. Biryukov, Crystal Channelling Simulation CATCH 1.4 User's Guide, SL / Note 93-74 (AP) (1993) 12 p.

92. V. G. Baryshevsky, V. V. Tikhomirov, Nucl. Instr. Meth. in Phys. Res. B **309**, 30-36 (2013).

93. V.B. Berestetskii, E.M. Lifshitz, L.P. Pitaevskii, *Quantum Electrodynamics. Vol. 4 (2nd ed.)*, (Butterworth-Heinemann, 1982).

94. C. Patrignani et al. (Particle Data Group), Chin. Phys. C **40**, 100001 (2016).

95. V. V. Beloshitsky, F. F. Komarov, M. A. Kumakhov, Phys. Reports. **139**, 293 (1986).

96. V. V. Beloshitsky, M. A. Kumakhov, Dokl. Acad. Nauk USSR **212**, 846 (1973).

97. T. Waho, Phys. Rev. **14**, 4830 (1976).

98. V.V. Tikhomirov, Eur. Phys. J. C **77**, 483 (2017).

99. V.A. Maisheev, Phys. Rev. STAB **10**, 084701 (2007).

100. S. Bellucci et al., Phys. Rev. STAB **18**, 114701 (2015).

101. V. A. Andreev et al., Pis'ma v Zh. Eksp. Teor. Fiz. **36**, 340 (1982).

102. V. A. Andreev et al., Pis'ma v Zh. Eksp. Teor. Fiz. **38**, 58 (1984).

103. V. A. Andreev et al., Pis'ma v Zh. Eksp. Teor. Fiz. **44**, 101 (1986).
104. Yu. A. Chesnokov et al., Nucl. Instr. and Meth. B **69**, 247 (1992).
105. N. F. Shul'ga, A. A. Greenenko, Phys. Lett. B **353**, 373–377 (1995).
106. A. A. Grinenko, N. F. Shul'ga, Sov. JEPT Lett. **54**, 524 (1991).
107. V. Tikhomirov, Phys. Lett. B **655**, 217 (2007).
108. G. I. Marchuk, Methods of Numerical Mathematics, Springer-Verlag, 1975, 316 p.
109. A.A. Samarskii, A.V. Gulin, *Numerical methods*, (Nauka, Moscow, 1989).
110. A.I. Drozhdin et al., in: Proc. of PAC, Portland, Oregon, USA, May 12-16, 2003, pp. 1733–1735.
111. K. Elsener et al., Nucl. Instr. and Meth. in Phys. Res. B 119, 215-230 (1996).
112. V. Tikhomirov, JINST **2**, P08006 (2007).
113. V. Guidi, A. Mazzolari, and V. Tikhomirov, J. Phys. D: Appl. Phys. **42**, 165301 (2009).
114. O. Brüning, P. Collier, P. Lebrun, S. Myers, R. Ostojic, J. Poole, and P. Proudlock, *LHC Design report, Vol. I, The LHC Main Ring* (CERN, Geneve, 2004).
115. G. Apollinari, I. Béjar Alonso, O. Brüning, M. Lamont, and L. Rossi (HiLumi LHC), *HL-LHC preliminary design report*, CERN-ACC-2014-0300 (2014).
116. S. Redaelli, in *Proc. of the Joint International Accelerator School*, Newport Beach, United States, 2014, edited by R. Schmidt (CERN, Geneva, 2016) pp. 403-437.
117. W. Scandale, Mod. Phys. Lett. A **27** No. 6, 1230007 (2012).
118. M. Maslov, N. Mokhov, and I. Yazynin, SSCL Report 484 (1991).
119. M. Fiascaris et al., in *Proc. of IPAC2016*, Busan, Korea, 2016, pp. 2423–2426.
120. W. Scandale et al., Phys. Lett. B **688**, 284 (2010).
121. M. Benedikt, D. Schulte, F. Zimmermann, Phys. Rev. ST Accel. Beams 18, 101002 (2015).
122. M. Benedikt, F. Zimmermann, Journal of the Korean Physical Society (2016) 69: 893. doi:10.3938/jkps.69.893
123. A. Ball et al., *Future Circular Collider Study Hadron Collider Parameters* (CERN, Geneve, 2014), https://indico.cern.ch/event/298180/contributions/1658149/attachments/560575/772288/FCC-1401101315-DSC_HadronColliderParameters_V0.3.pdf

124. https://impedance.web.cern.ch/impedance/fcchh/beam_dynamics_parameters.html
125. James Molson, Philip Bambade, Sophie Chancé, Angeles Faus-Golfe in *Proc. of IPAC2016*, Busan, Korea, 2016, pp. 1381–1383.
126. T. Behnke et al. arXiv:1306.6327 (2013)
127. R. Tomaás Phys. Rev. ST – Acc. and Beams 13, 014801 (2010)
128. L. Bandiera et al. Journal of Physics: Conference Series 517, 012043 (2014)
129. A. Seryi et al. Nucl. Instr. and Meth. in Phys. Res. A 623, 23 (2010)
130. E. Bagli et al. Proc. of IPAC'10, THPEC080, 4243 (2010).
131. R. Camattari, V. Guidi, V. Bellucci, A. Mazzolari, J. Appl. Cryst. 107, 064102-1–5 (2015) 10.1107/S1600576715009875
132. Guidi et al. J. Phys. D: Appl. Phys. 42, 182005 (2009).
133. D. Lietti et al. Rev. Sci. Instr. 86, 045102 (2015)
134. J.H. Barrett, Phys. Rev. B **3**, 1527 (1971).
135. J.H. Barrett, Phys. Rev. B **20** No. 9, 3535–3542 (1979).
136. F. Abel et al., Phys. Lett. A **42**, 165–166 (1972).
137. F. Abel et al., Phys. Rev. B **12** No. 11, 4617–4627 (1975).
138. F. Abel et al., Phys. Rev. B **13** No. 3, 993–1005 (1976).
139. E. N. Kaufmann, Phys. Rev. B **17** No. 3, 1024–1027 (1978).
140. M.B.H. Breese et al., Phys. Rev. B **53** No. 13, 8267–9276 (1996).
141. M.B.H. Breese et al., Phys. Rev. Lett. **92** No. 13, 045503 (2004).
142. V. Berec et al., Nucl. Instr. and Meth. in Phys. Res. B **355**, 324–327 (2015).
143. H. Esbensen et al. Phys. Rev. B **18** N3 (1978) 1039–1054.
144. S.P. Moller et al., Nucl. Instr. Meth. B **84** (1994) 434–442.
145. A.M. Taratin. Nucl. Instr. Meth. B **119** (1996) 156–162.
146. G. Germogli et al., Nucl. Instr. and Meth. in Phys. Res. B **355**, 81–85 (2015).